The Abdus Salam
International Centre for Theoretical Physics

United Nations
Educational, Scientific and
Cultural Organization

IAEA
International Atomic Energy Agency

1930-3

Joint ICTP-IAEA Advanced Workshop on Model Codes for Spallation Reactions

4 - 8 February 2008

The Role of Multifragmentation in Spallation Reactions.

Alexander Botvina

Institute for Nuclear Research
Russian Academy of Sciences
Moscow
Russian Federation

Strada Costiera 11, 34014 Trieste, Italy - Tel. +39 040 2240 111; Fax +39 040 224 163 - sci_info@ictp.it, www.ictp.it

The Joint ICTP-IAEA Advanced Workshop on

Model Codes for Spallation Reactions

ICTP, Trieste, Feb. 4 - 8, 2008

The role of multifragmentation in spallation reactions

A.S. Botvina

Institute for Nuclear Research, Russian Academy of Sciences, Moscow, Russia

Statistical approach in nuclear reactions: conception of equilibrium

Intermediate energy collisions

Preequlibrium emission + equilibration

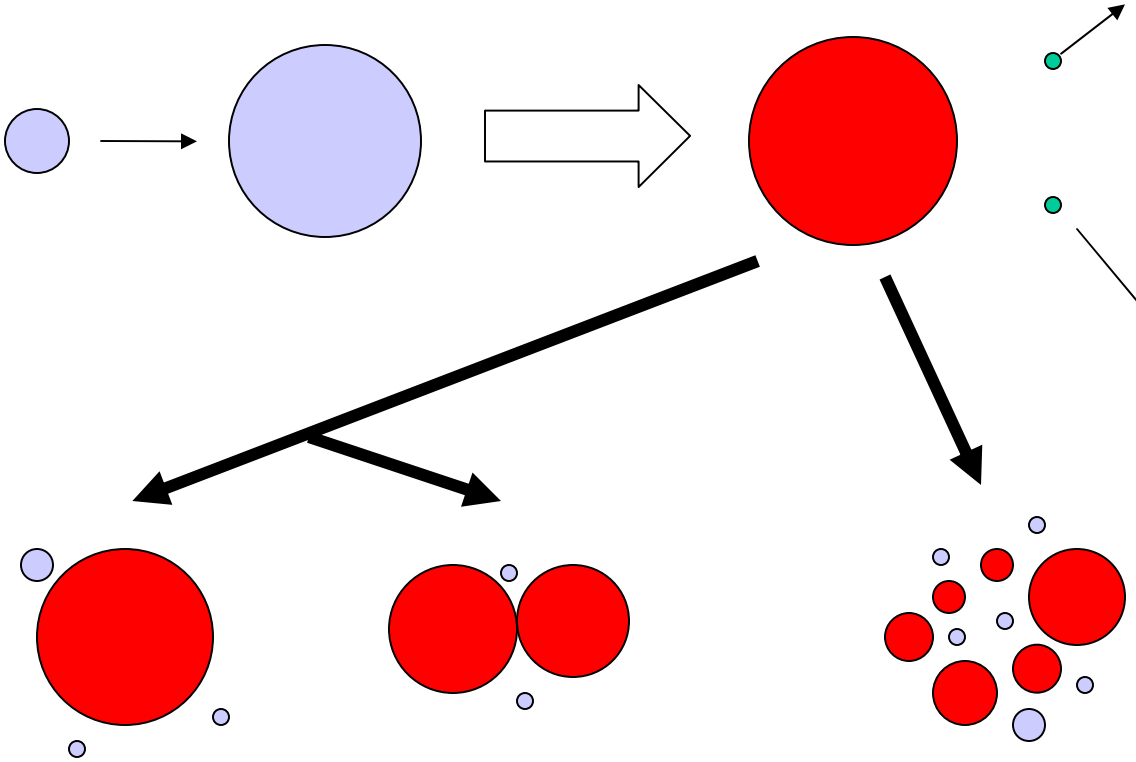

N.Bohr (1936)

Compound-nucleus decay channels (sequential evaporation or fission) dominate at low excitation energy of thermal sources E^*<2-3 MeV/nucl

N.Bohr, J.Wheeler (1939)
V.Weisskopf (1937)

starting 1980-th :

At high excitation energy E^*>3-4 MeV/nucl there is a simultaneous break-up into many fragments

evaporation fission multifragmentation

"If it were possible to experiment with neutrons or protons of energies above a hundred million volts, several charged or uncharged particles would eventually leave the nucleus as a result of the encounter; with particles of energies of about a thousand million volts, we must even be prepared for the collision to lead to an explosion of the whole nucleus"

Niels Bohr, Nature 137 (1936) 351

Experimental evidences of multifragmentation:

induced by hadrons: N.A.Perfilov, O.V.Lozhkin, V.I.Ostroumov (1962)

by heavy ions: B.Jakobsson et al., Z.Phys. **A307** (1982) 293

Statistical theories:

J.Randrup, S.E.Koonin (since 1981)

D.H.E.Gross (1982)

J.Bondorf, I.N.Mishustin, C.Pethick (1983)

Development of the statistical multifragmentation model (SMM)

J.P.Bondorf, R.Donangelo, I.N.Mishustin, C.J.Pethick, H.Schulz, K.Sneppen,
Nucl. Phys. **A443** (1985) 321

A.S.Botvina, A.S.Iljinov, I.N.Mishustin, Sov. J. Nucl. Phys. **42** (1985) 712

application to description of hadron-nucleus reactions of high energy:

A.S.Botvina, A.S.Iljinov, I.N.Mishustin, JETP Lett. **42** (1985) 572

A.S.Botvina, A.S.Iljinov, I.N.Mishustin, J.Bondorf, R.Donangelo, K.Sneppen,
Nucl. Phys. A**475** (1987) 663
A.S.Botvina, A.S.Iljinov, I.N.Mishustin, Nucl. Phys. A**507** (1990) 649

J.P.Bondorf, A.S.Botvina, A.S.Iljinov, I.N.Mishustin, K.Sneppen,
Phys. Rep. **257** (1995) 133 (>400 citations according to ISI Web)

Equation of State of nuclear matter at subnuclear densities.

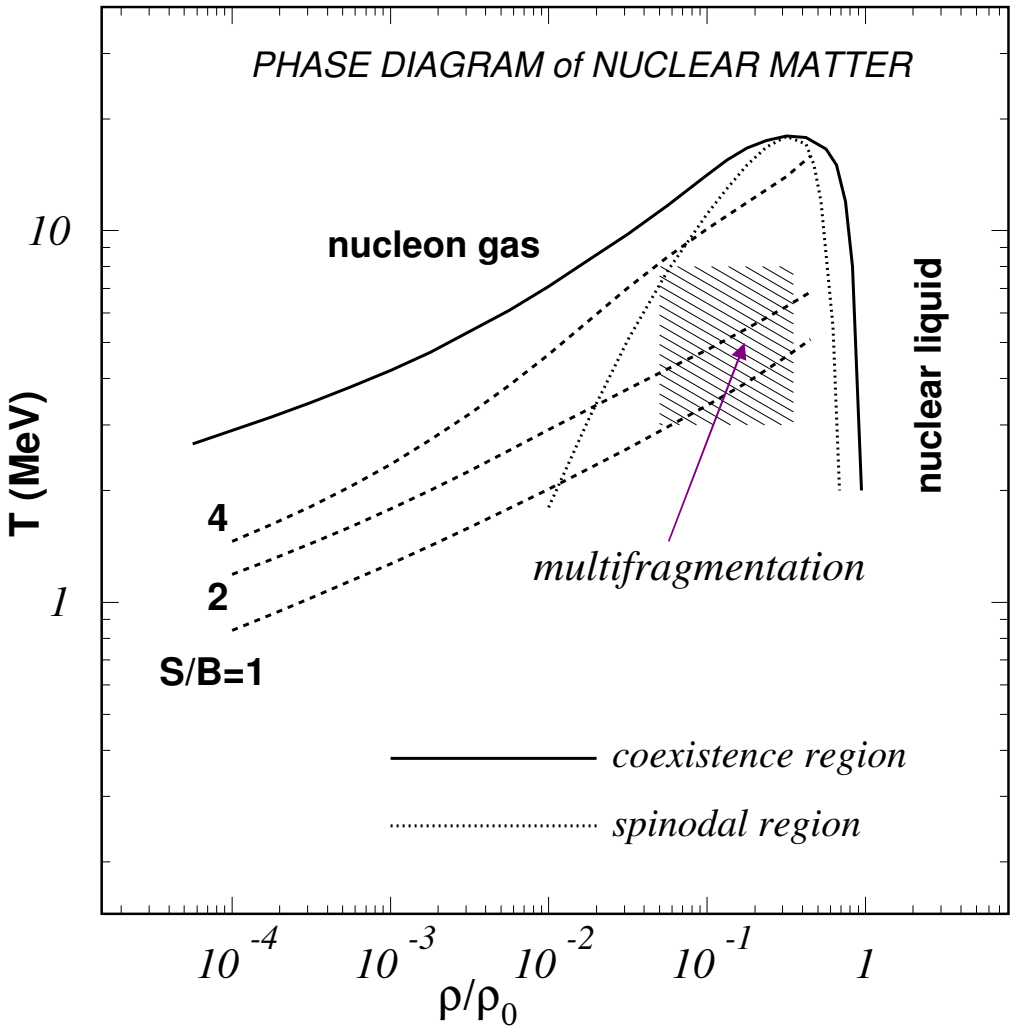

related nuclear process:
thermal multifragmentation of nuclei

Production of hot fragments at

temperature T ~ 3---8 MeV and
density $\rho \sim 0.1\ \rho_0$ ($\rho_0 \approx 0.15$ fm^{-3})

Interpretation: liquid-gas phase transition in finite nuclei. Investigation of properties of fragments surrounded by nuclear species.

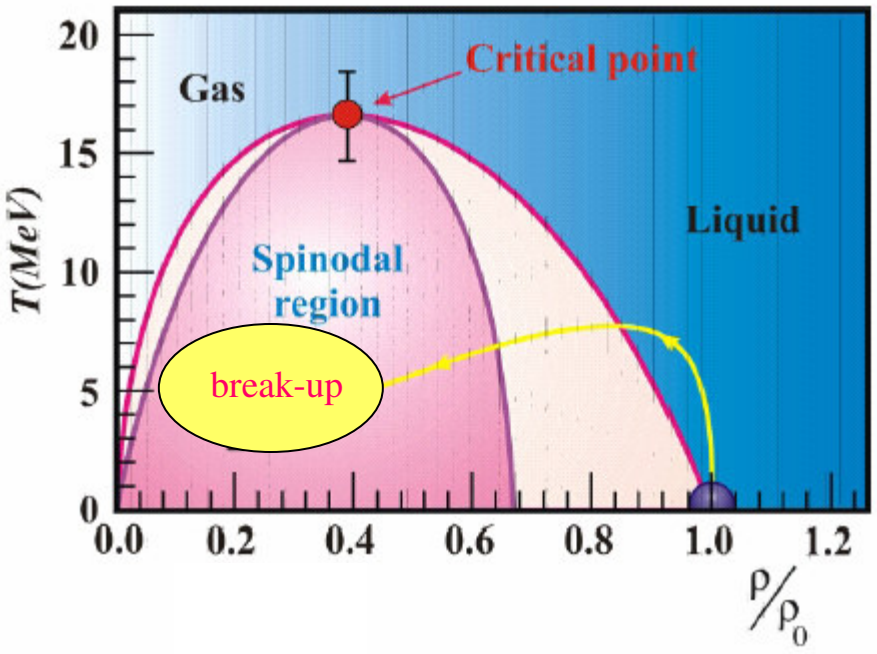

Simultaneous break-up is seen in dynamical calculations

Multifragmentation barriers of excited finite nuclei

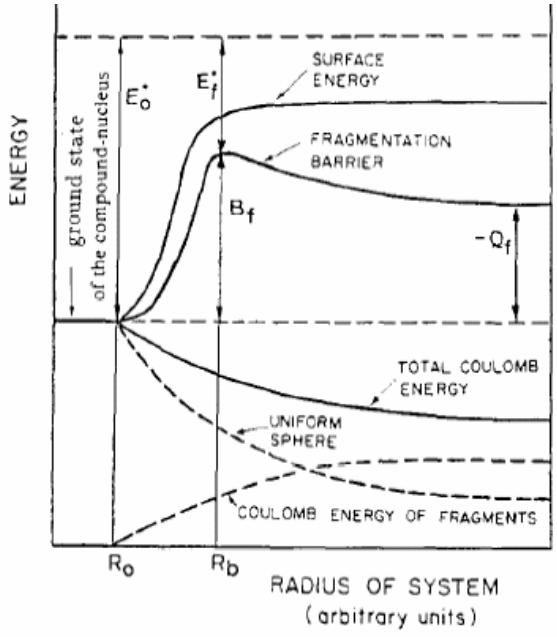

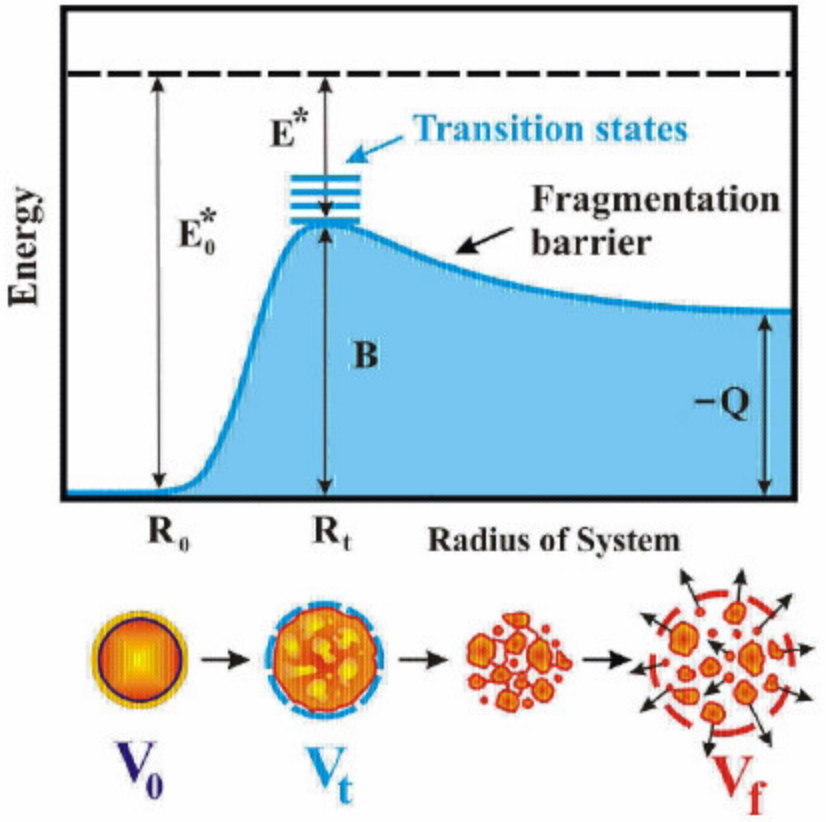

Statistical Multifragmentation Model (SMM)

J.P.Bondorf, A.S.Botvina, A.S.Iljinov, I.N.Mishustin, K.Sneppen, Phys. Rep. **257** (1995) 133

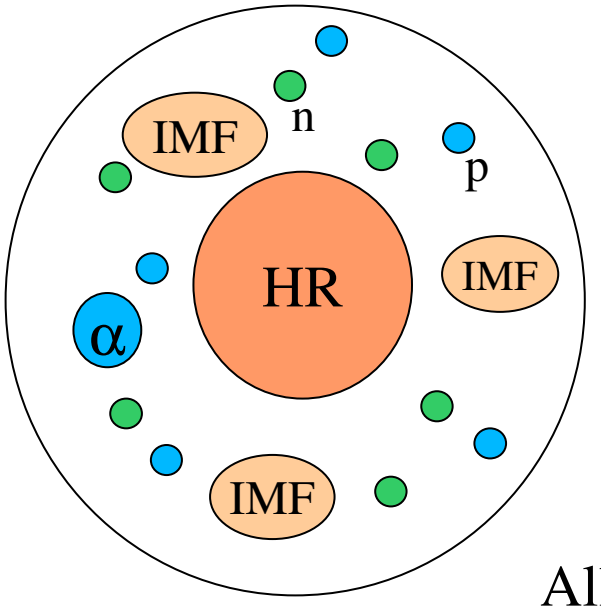

Ensemble of nucleons and fragments
in thermal equilibrium characterized by

neutron number N_0

proton number Z_0, $N_0+Z_0=A_0$

excitation energy $E^*=E_0-E_{CN}$

break-up volume $V=(1+\kappa)V_0$

All break-up channels are enumerated by the sets of fragment multiplicities or partitions, $f=\{N_{AZ}\}$

Statistical distribution of probabilities: $W_f \sim \exp\{S_f(A_0, Z_0, E^*, V)\}$

under conditions of baryon number (A), electric charge (Z) and energy (E*) conservation, including compound nucleus.

mass and charge conservation $\sum_{(A,Z)} N_{AZ} A = A_0, \quad \sum_{(A,Z)} N_{AZ} Z = Z_0.$

entropy of channel: $S_f = -\left(\frac{\partial F_f}{\partial T}\right)$ Energy conservation: $E_0 = F_f + T S_f$

Fragments obey Boltzmann statistics, liquid-drop description of individual fragments, Coulomb interaction in the Wigner-Seitz approximation

free energy of channel: $F_f(T,V) = F_f^{tr} + \sum_{(A,Z)} F_{AZ} N_{AZ} + \frac{3}{5}\frac{Z_0^2 e^2}{R}.$

$$F_f^{tr} = -T\left[\sum_{(A,Z)} N_{AZ} \ln\left(g_{AZ}\frac{V_f}{\lambda_T^3}A^{3/2}\right) - \ln\left(N_{AZ}!\right)\right] + T\ln\left(\frac{V_f}{\lambda_T^3}A_0^{3/2}\right)$$

individual fragments: $F_{AZ} = F_{AZ}^B + F_{AZ}^S + F_{AZ}^{\rm sym} + E_{AZ}^C$

$$F_{AZ}^B = \left(-w_0 - \frac{T^2}{\varepsilon_0}\right)A \qquad F_{AZ}^S = \beta_0\left(\frac{T_c^2 - T^2}{T_c^2 + T^2}\right)^{5/4} A^{2/3}$$

$$F_{AZ}^{\rm sym} = \gamma\frac{(A-2Z)^2}{A} \qquad E_{AZ}^C = \frac{3e^2}{5r_0}\left[1 - \left(\frac{V_0}{V}\right)^{1/3}\right]\frac{Z^2}{A^{1/3}}$$

A.S.Botvina, A.S.Iljinov, and I.N. Mishustin

Sov.J.Nucl.Phys. v.42, 712 (1985)

Onset of multifragmentation at high temperature

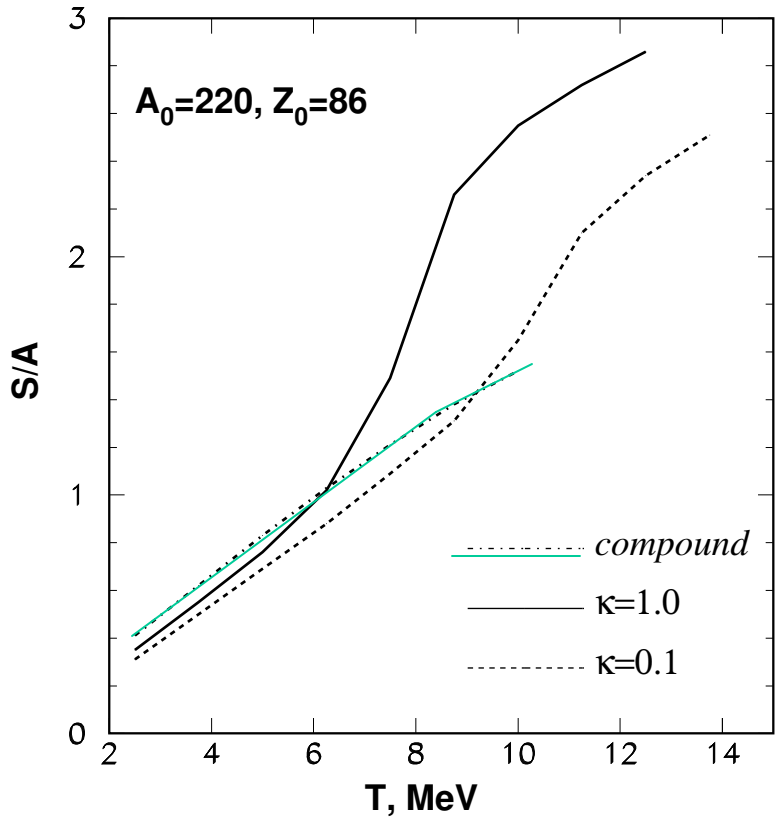

evolution of the mass distribution of fragments with excitation energy

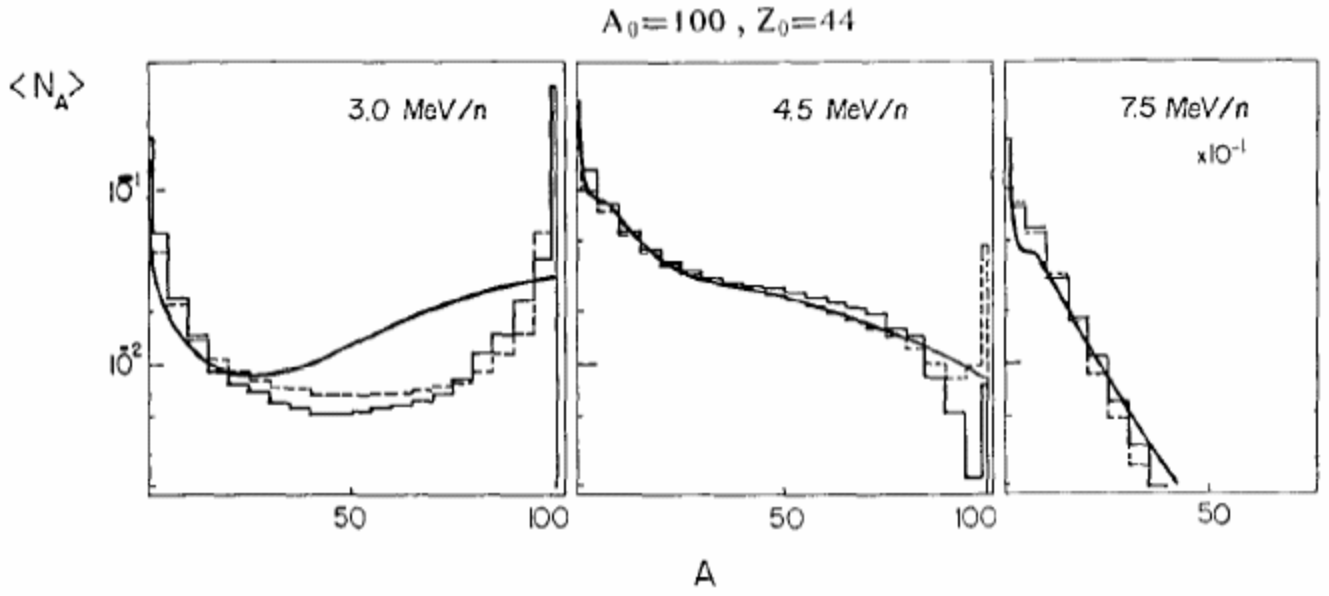

J.P.Bondorf et al.,
Phys. Rep. **257** (1995) 133

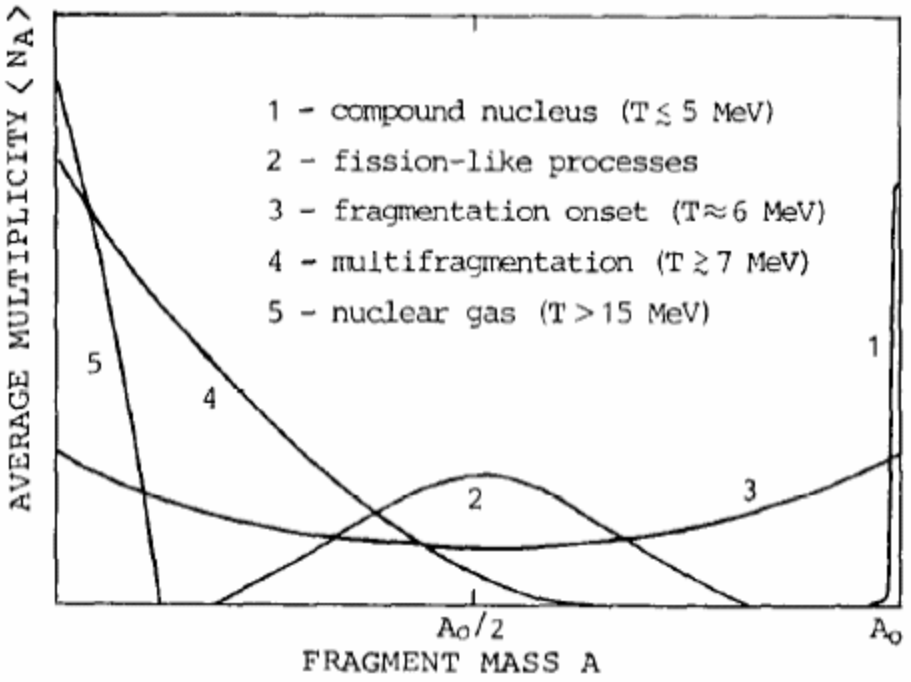

compound probability

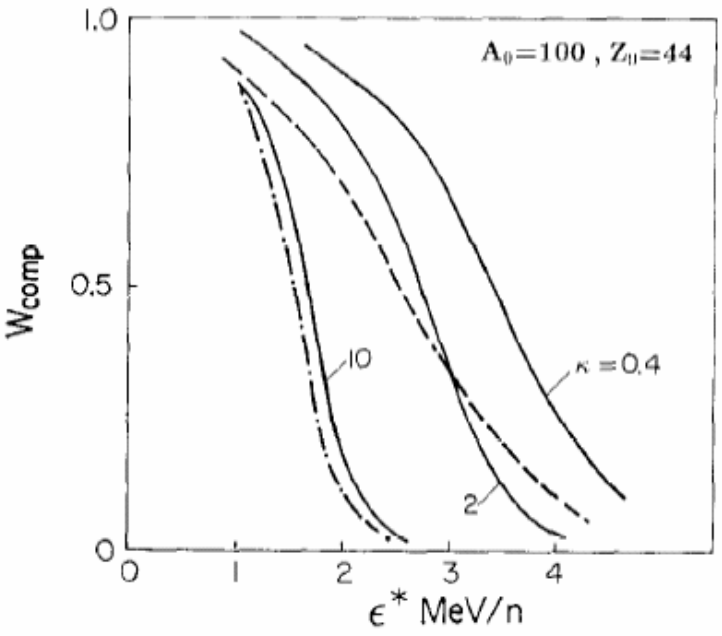

fragment multiplicity + caloric curve

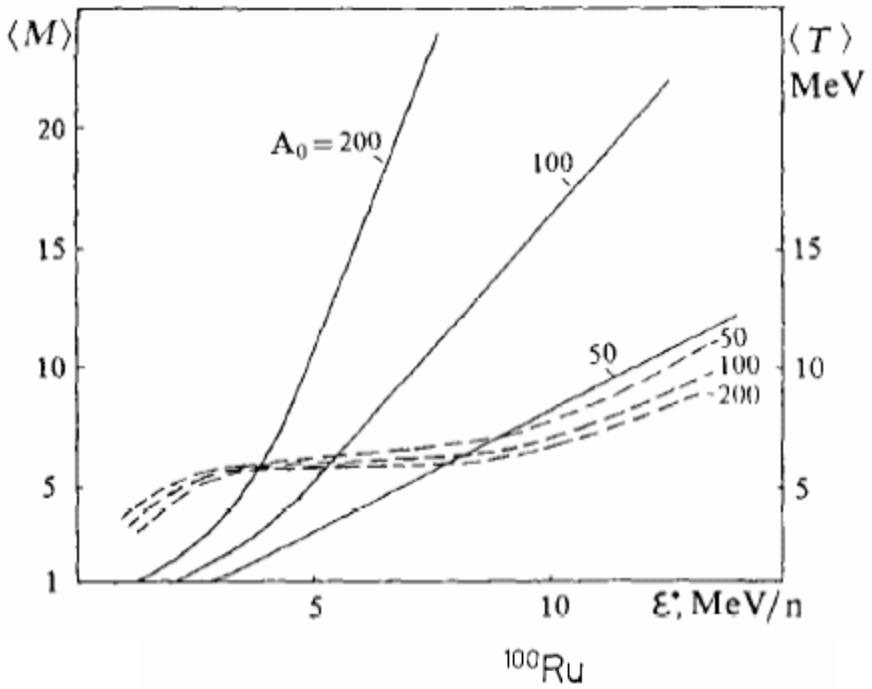

multiplicity distributions

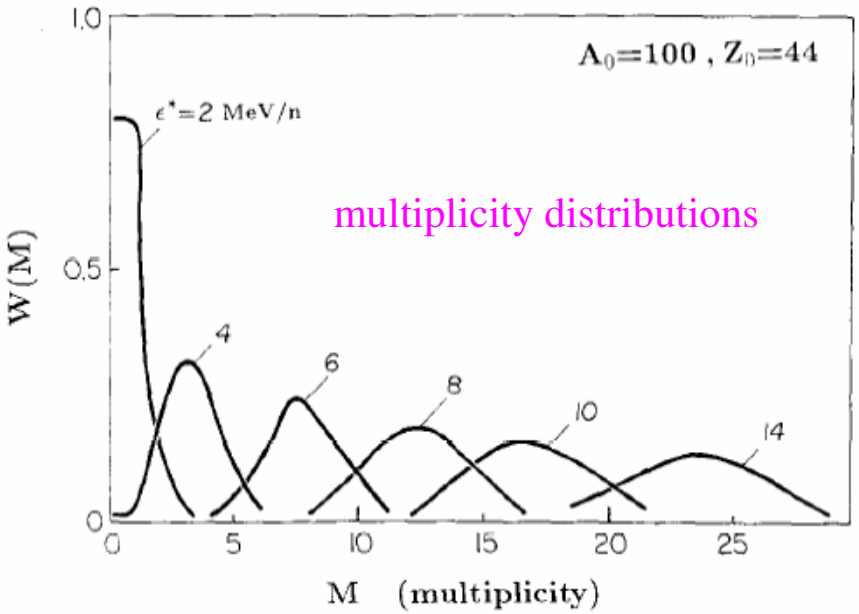

contributions to total energy

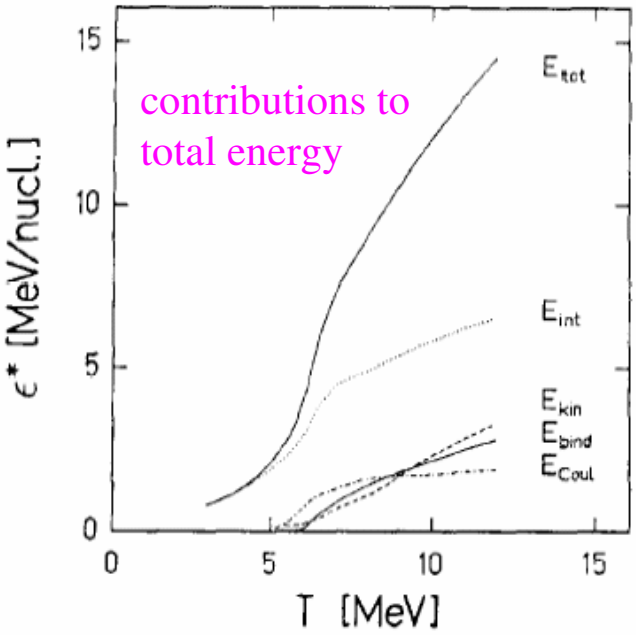

Multifragmentation in intermediate and high energy nuclear reactions

Experimentally established: 1) few stages of reactions leading to multifragmentation, 2) short time ~100fm/c for primary fragment production, 3) freeze-out density is around $0.1\rho_0$, 4) high degree of equilibration at the freeze-out, 5) primary fragments are hot.

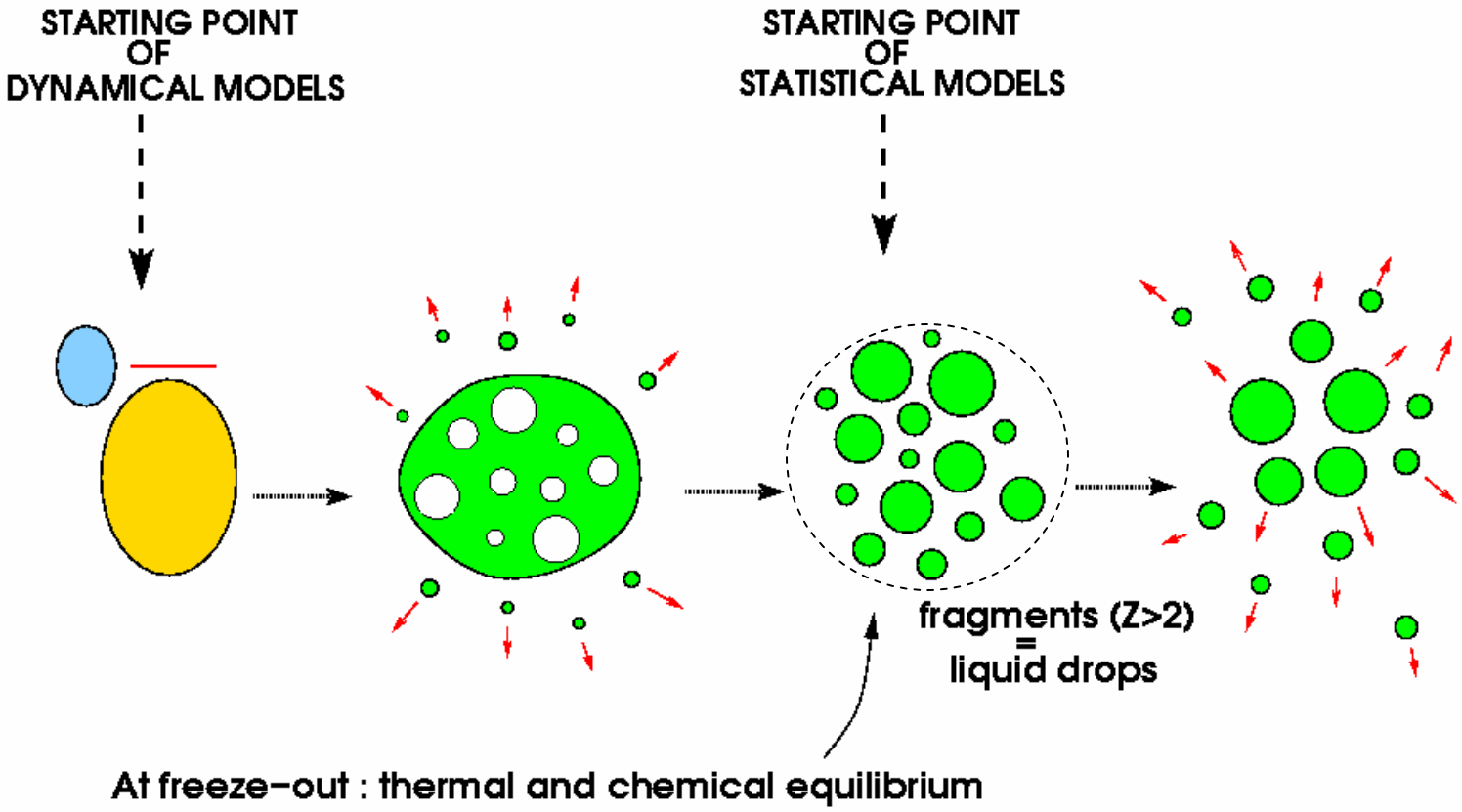

Residual nuclei after Intranuclear cascade calculations

——— INC + trawling

– – – – INC

– . – – . – INC+trawling+preequilibrium

..... INC+preequilibrium

Nucl. Phys. A507(1990)649

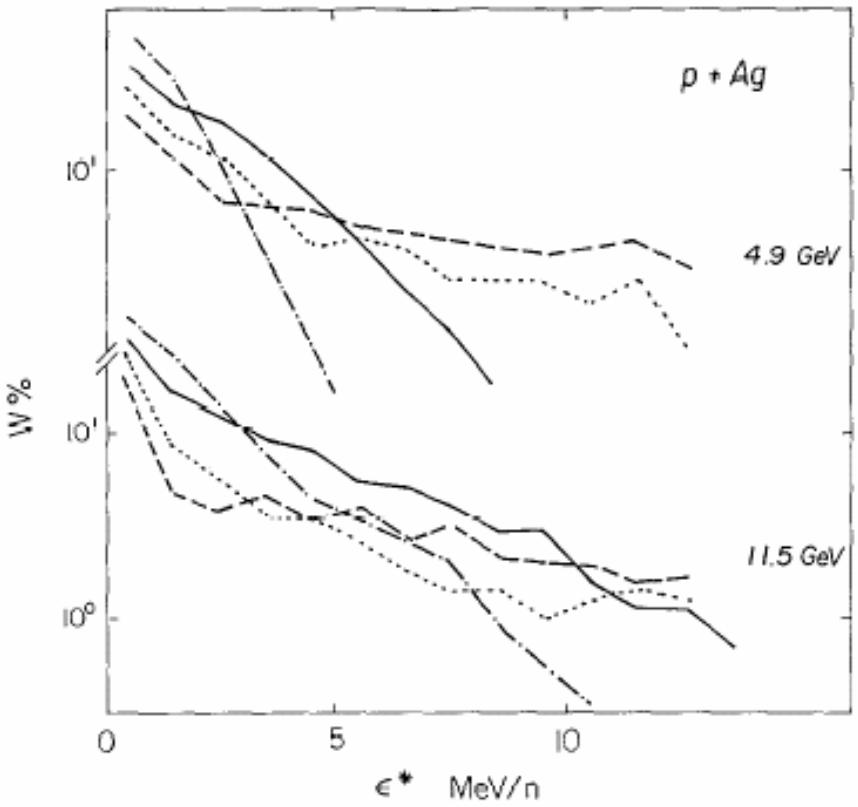

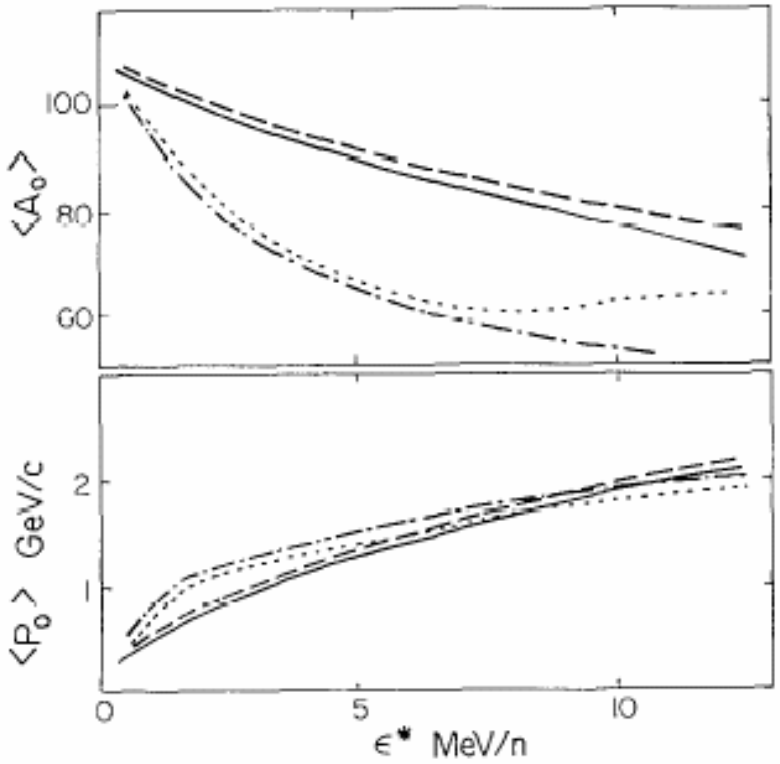

Dynamical stage of the reactions

masses and excitation energies of thermal sources:

INC

Nuclear Physics **A507** (1990) 649–674

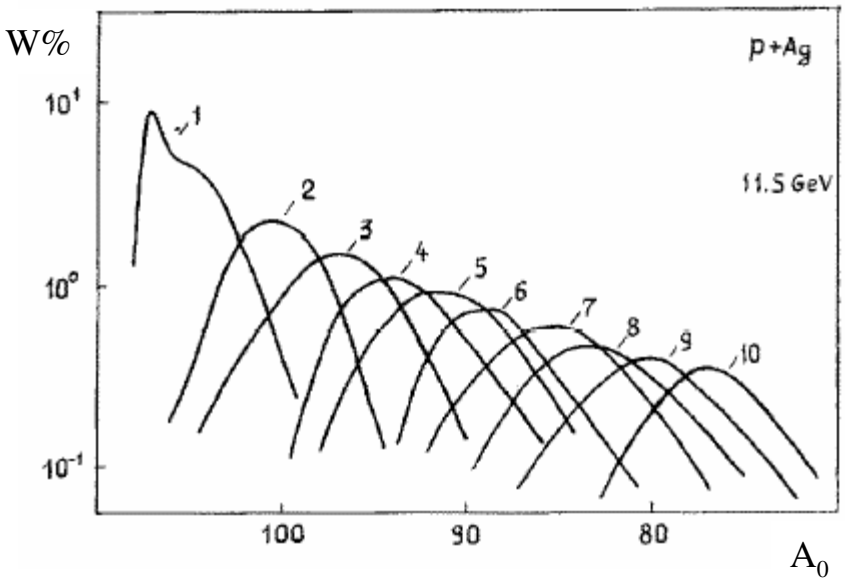

Fig. 3. Distribution of the RN masses in certain intervals of their excitation energy after the intranuclear cascade. The target and the proton energies are indicated in the figure. The ICM with trawling is employed for the calculation. The RN excitation energy intervals are shown by figures near the curves: 1 – E_0 = 0-1 MeV/nucleon; 2 – E_0 = 1-2 MeV/nucleon; ... 10 – E_0 = 9-10 MeV/nucleon.

QMD

Prog. Part. Nucl. Phys., Vol. 30, pp. 301–302, 1993.

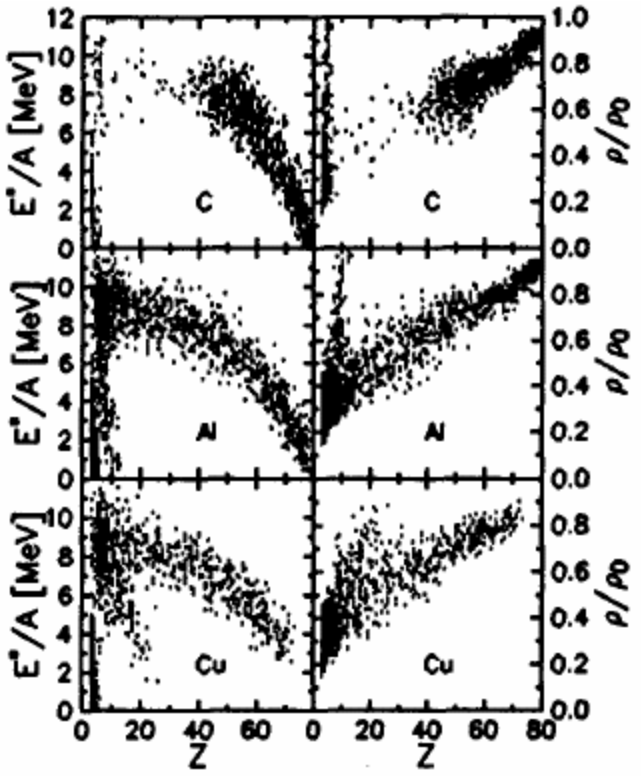

Figure 1: Excitation energies and densities of the primordial fragments in Au (600 MeV/nucleon) + C, Al, Cu. Each point characterizes a single fragment present after a QMD propagation for 200 fm/c.

Time scale of the thermal multifragmentation

ISIS collaboration

velocity correlations of fragments

π^-(8GeV/c)+Au

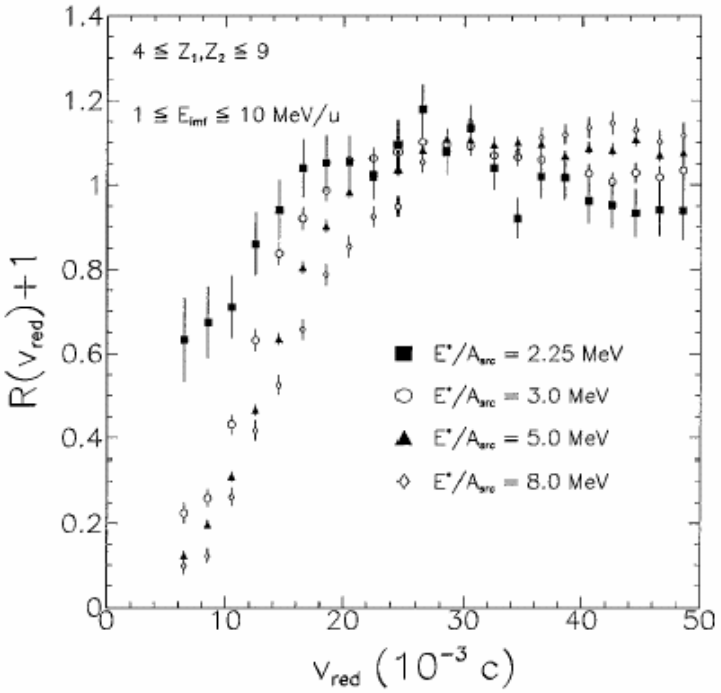

FIG. 1. Reduced velocity correlation functions generated for four different excitation energy per nucleon bins. IMF kinetic energy acceptance is in source frame is $E_{\mathrm{IMF}}/A = 1-10$ MeV.

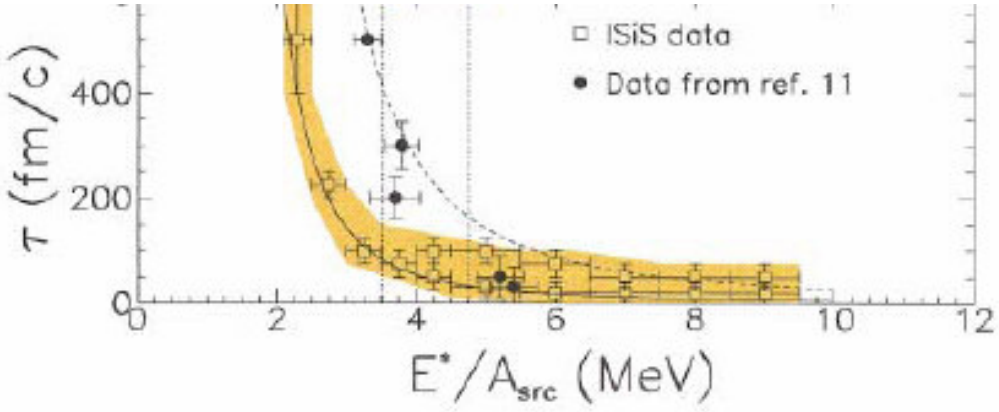

L.Beaulieu et al., Phys. Rev. Lett. **84**, 5971 (2000)

Time scale of the thermal multifragmentation

angle correlations of fragments

p(8.1 GeV) + Au

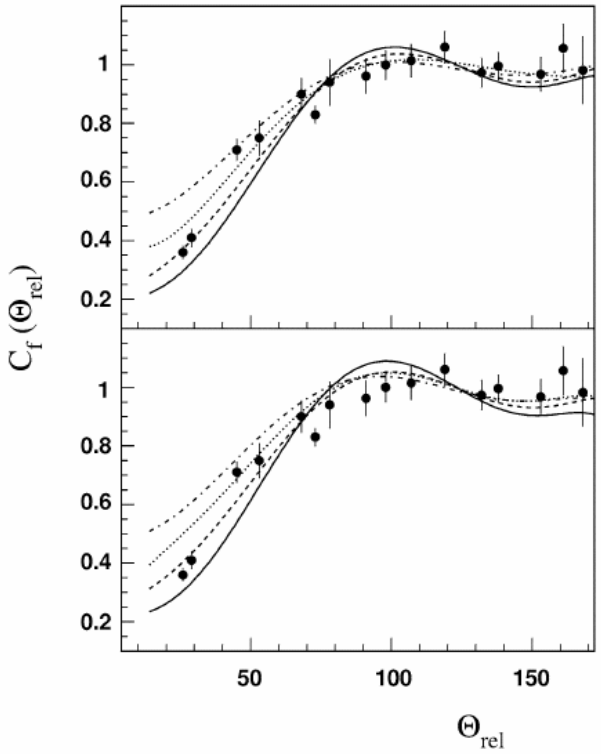

Fig. 5. Comparison of the measured correlation functions (full circles) with the calculated ones for different mean decay times of the fragmenting system: solid, dashed, dotted and dash-dotted lines for $\tau = 0$, 50, 100 and 200 fm/c. The upper panel is for the RC + α + SMM model with the parameters $(4, 8, \eta)$ (see notation in Fig. 4), the lower panel is for the same model, but with the parameters $(4, 4, \eta)$ allowing the fragments to overlap (see text).

FASA

collaboration

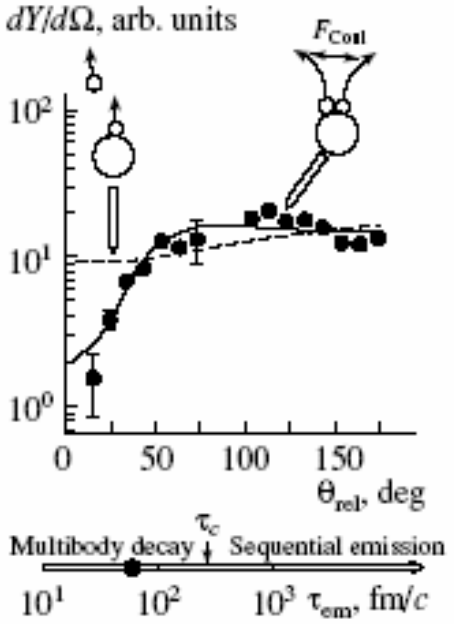

Fig. 5. Distribution of relative angles between coincident IMFs for ^{4}He(14.6 GeV) + Au collisions. The solid curve is calculated for the simultaneous emission of fragments; the dashed curve corresponds to the sequential, independent evaporation.

Nuclear caloric curve

Predicted in 1985 within the SMM

Bondorf, Donangelo, Mishustin, Schulz
NPA 444 (1985) 460

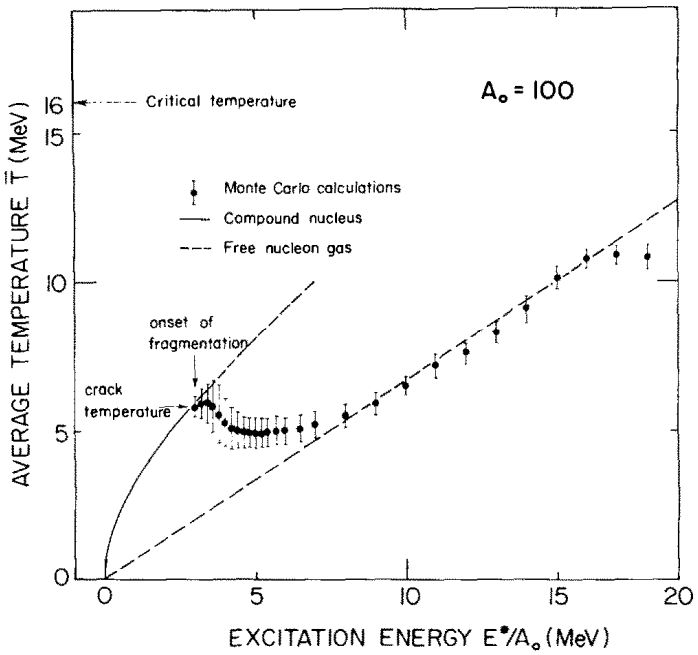

Fig. 4. The average temperature T as a function of the excitation energy E^*/A_0. The dashed line illustrates the temperature of a free nucleon gas.

Experimental result in 1995

Pochodzalla and ALADIN collaboration,
PRL 75 (1995) 1040

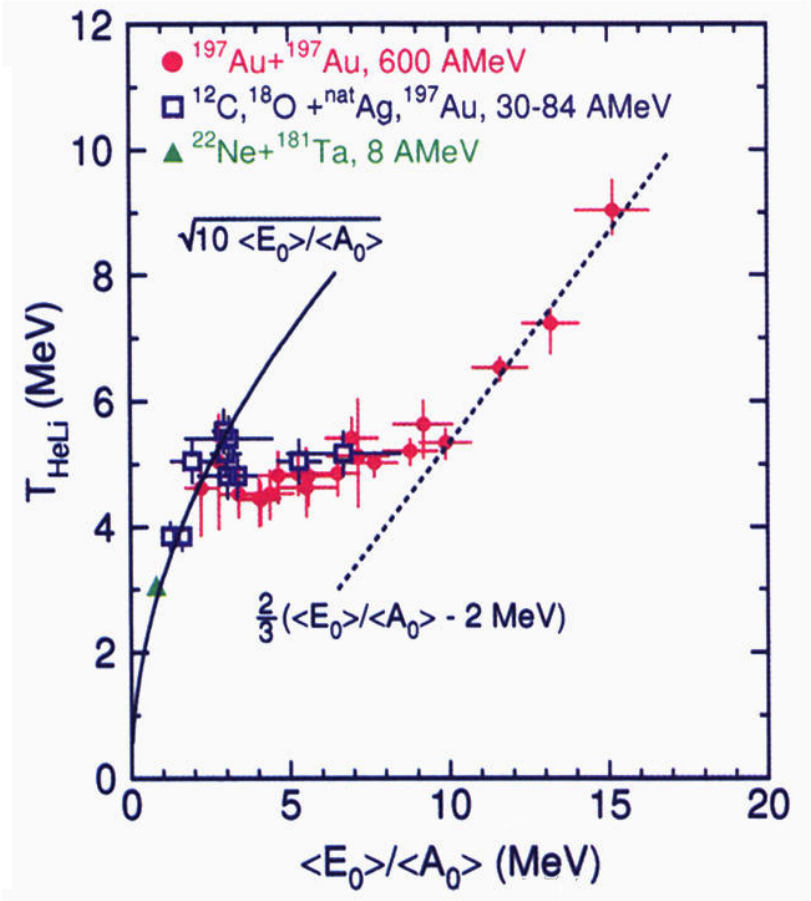

FIG. 2. Caloric curve of nuclei determined by the dependence of the isotope temperature T_{HeLi} on the excitation energy per nucleon. The lines are explained in the text.

MULTICS

Au(35MeV/N)+Au, peripheral

2 MeV/n

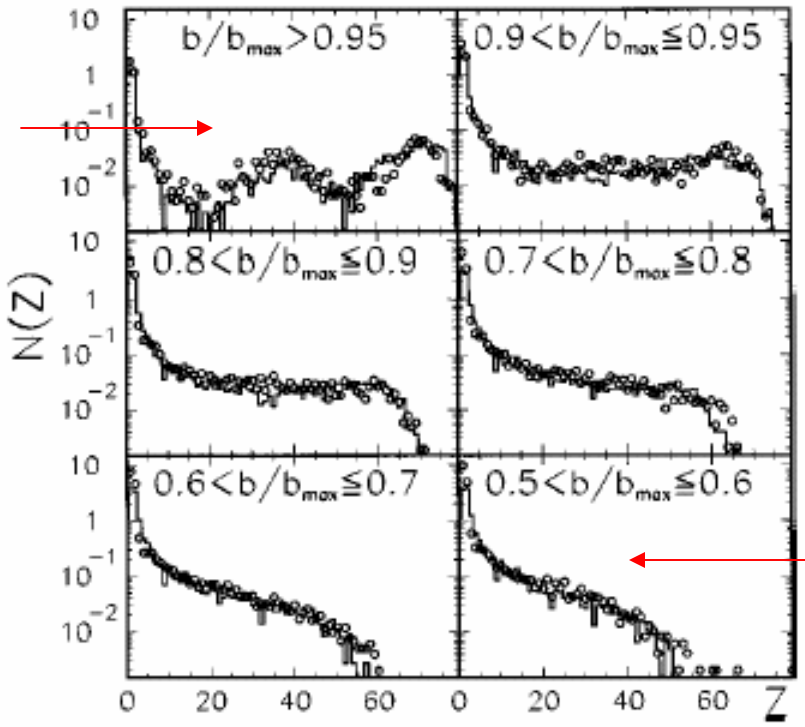

5 MeV/n

FIG. 8. Charge distributions for peripheral and midperipheral collisions (open point: experimental data; histogram: SMM predictions).

M.D'Agostino et al., Nucl.Phys. A**650** (1999) 329

ALADIN data

GSI

multifragmentation of relativistic projectiles

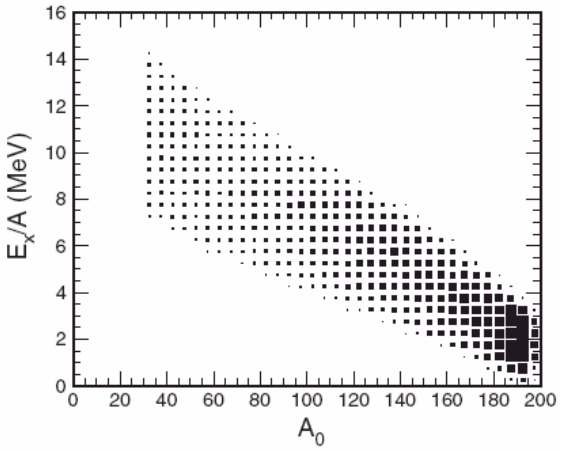

A.S.Botvina et al.,
Nucl.Phys. A584(1995)737

H.Xi et al.,
Z.Phys. A359(1997)397

comparison with SMM (statistical multifragmentation model)

Statistical equilibrium has been reached in these reactions

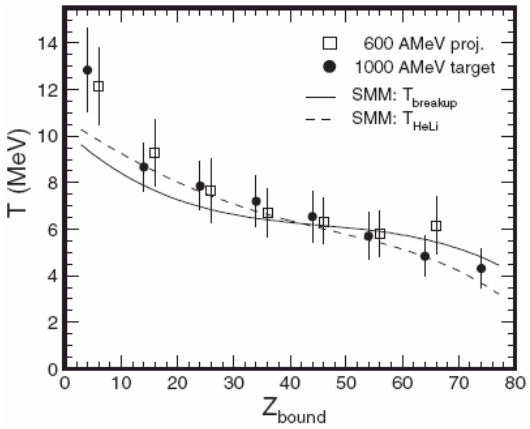

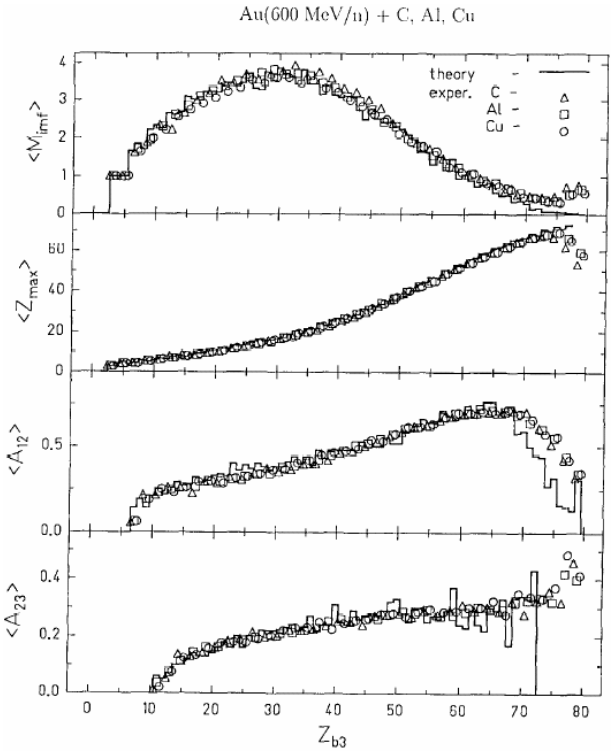

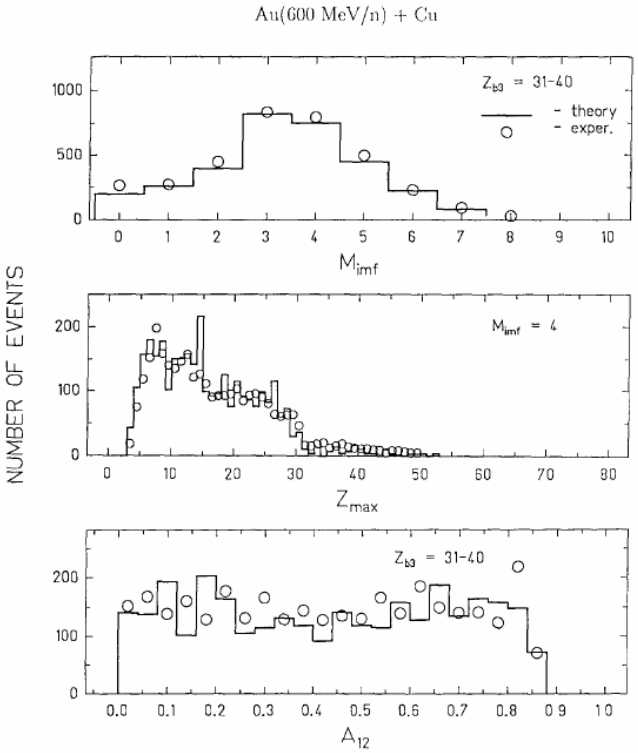

Nuclear Physics A561 (1993) 466–476

BUU dynamics in projectile: Au (600 MeV/n) + Cu

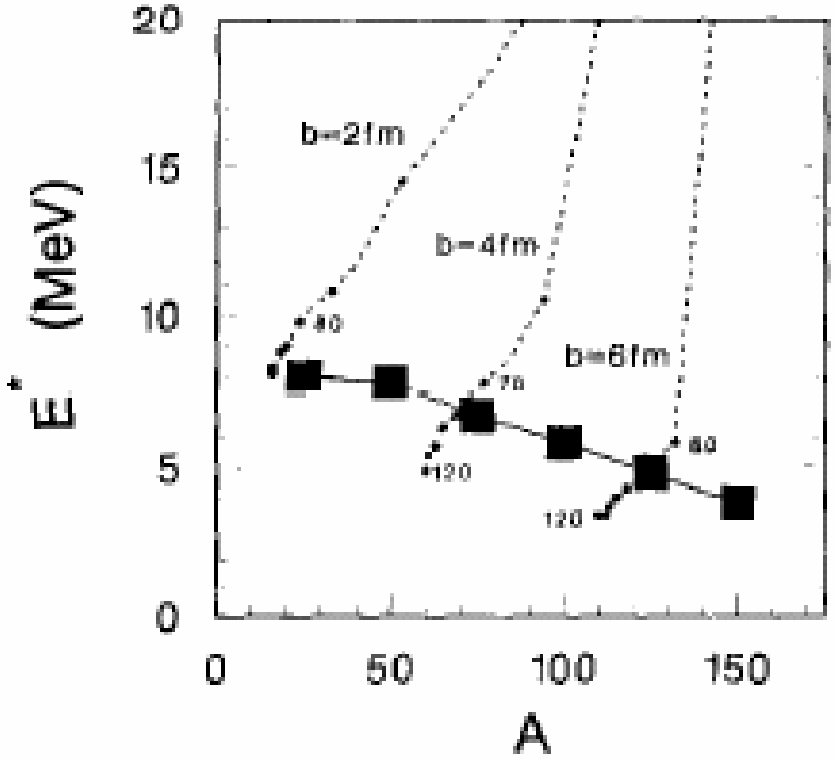

Coupled to describe ALADIN data with statistical model of multifragmentation

Fig. 5. Evolution of the mass number A and excitation energy E^* of the cooling remnant of the Au on Cu collision according to the BUU model for three different impact parameters (dashed lines). The dots on these lines are placed every 10 fm/c and the numbers indicate the times in fm/c. The full squares indicate the break-up conditions calculated with the statistical model already shown in Fig. 2.

Two-stage multifragmentation of 1*A* GeV Kr, La, and Au

EOS

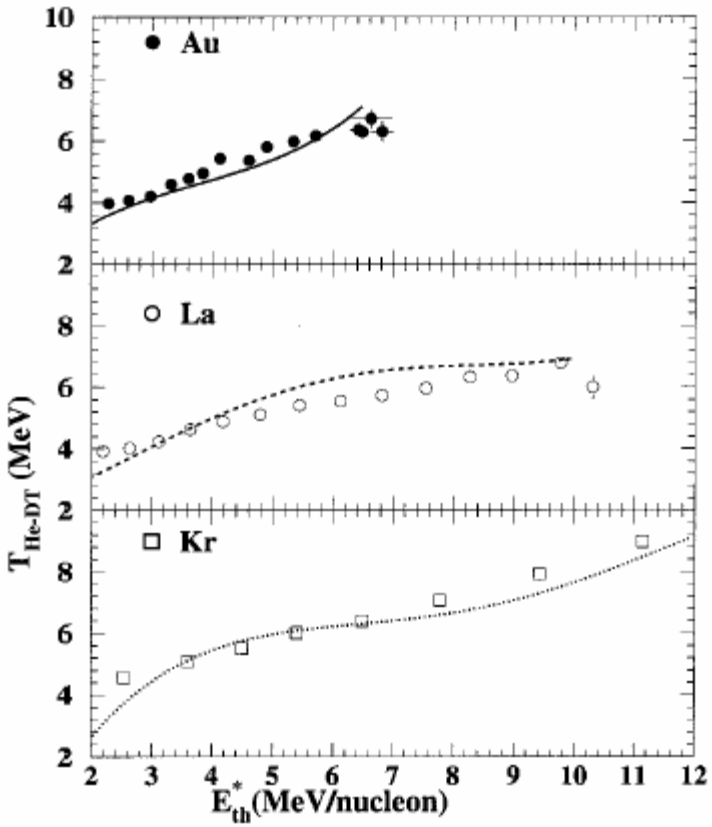

FIG. 19. Caloric curves (T_f vs E^*_{th}/A) for Kr, La, and Au. Points are experimental and curves are from SMM.

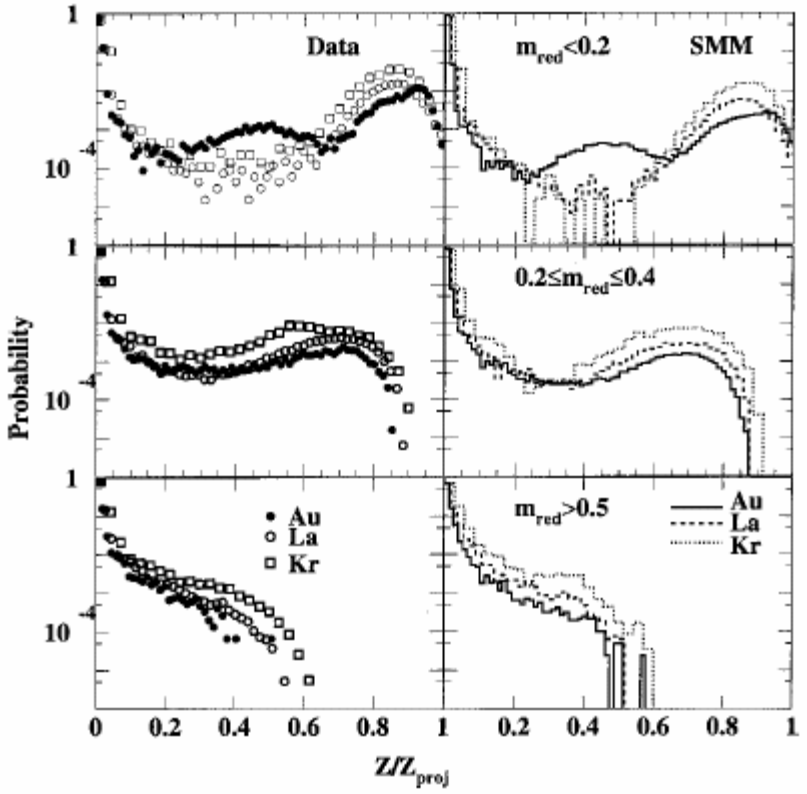

FIG. 24. Second stage fragment charge distribution as a function of $Z/Z_{\text{projectile}}$. Results are shown for three reduced multiplicity intervals for both data and SMM.

Multifragmentation and the phase transition: A systematic study of the multifragmentation of 1A GeV Au, La, and Kr

EOS

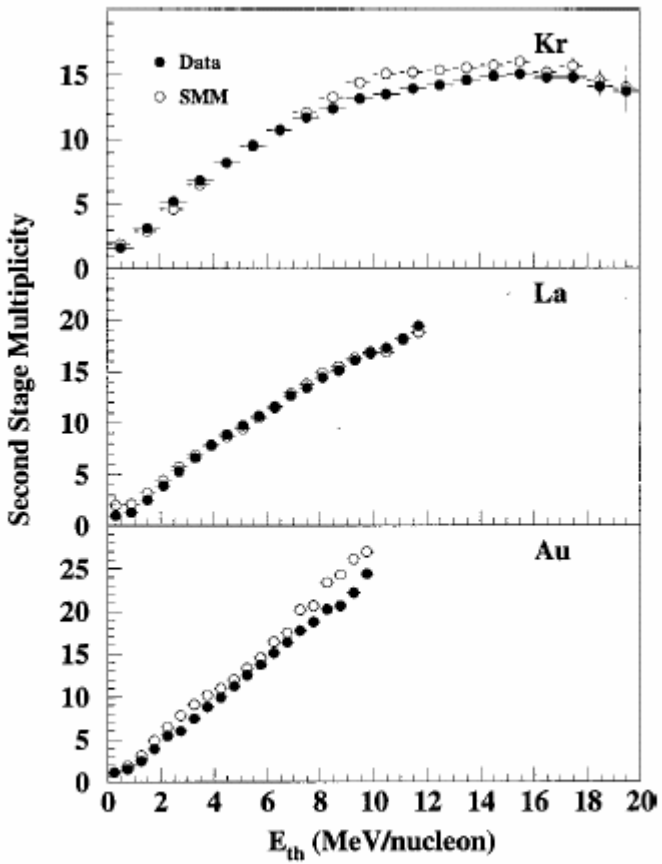

FIG. 6. Second stage charged-particle multiplicity as a function of E^*_{th} for Kr, La, and Au from data and SMM.

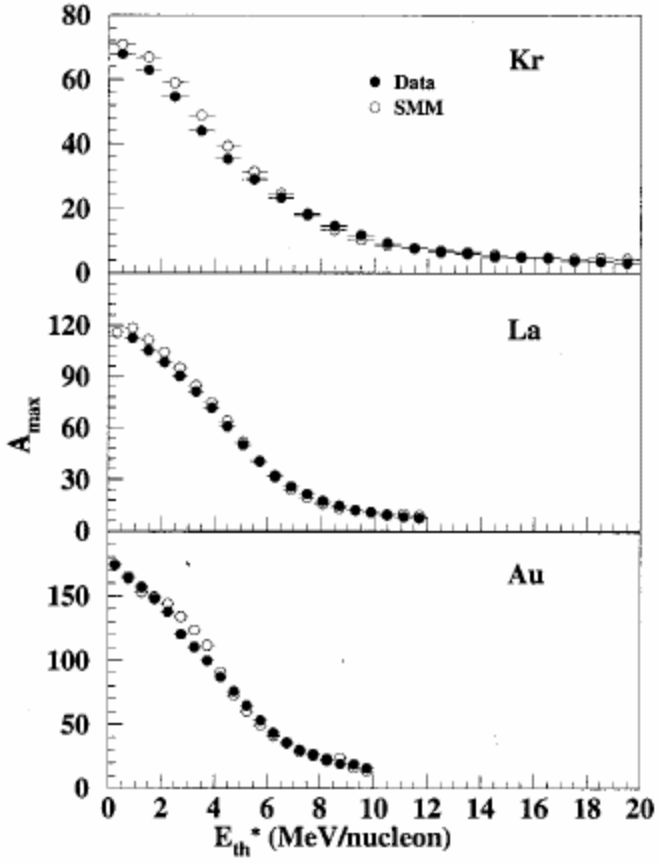

FIG. 7. Size of the largest fragment as a function of E^*_{th} for Kr, La, and Au from data and SMM.

INDRA

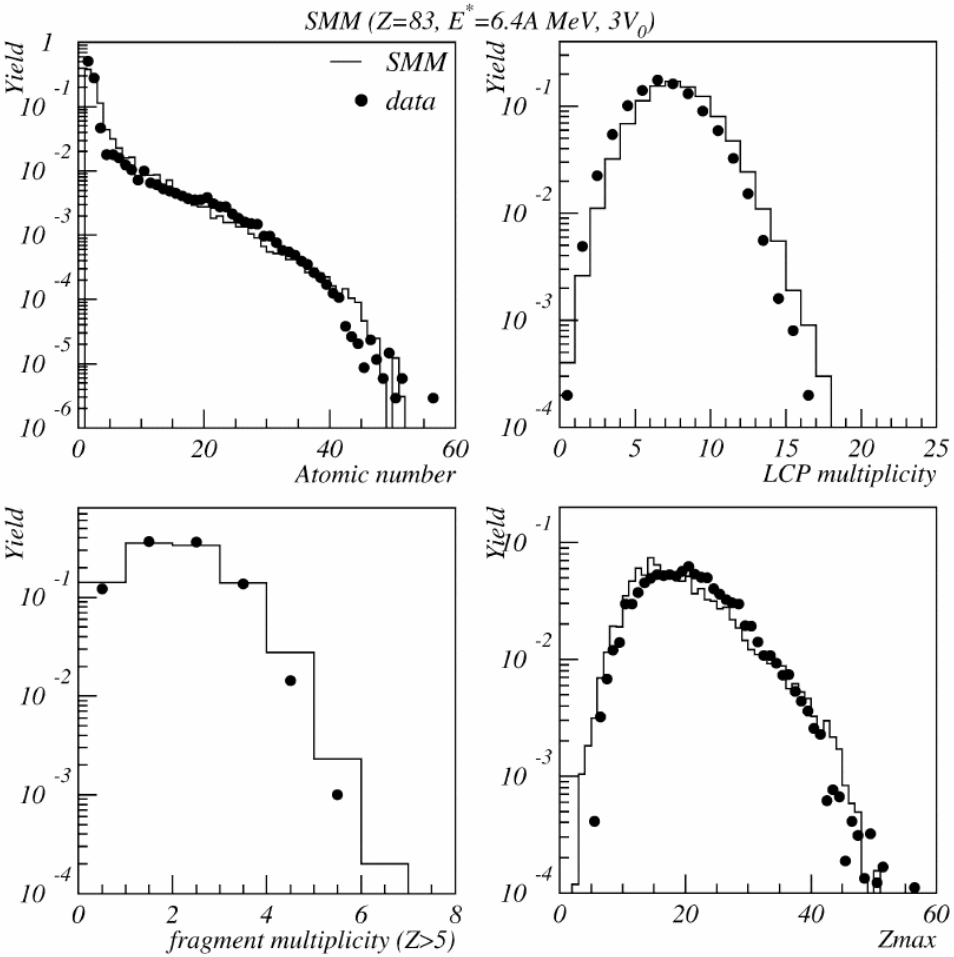

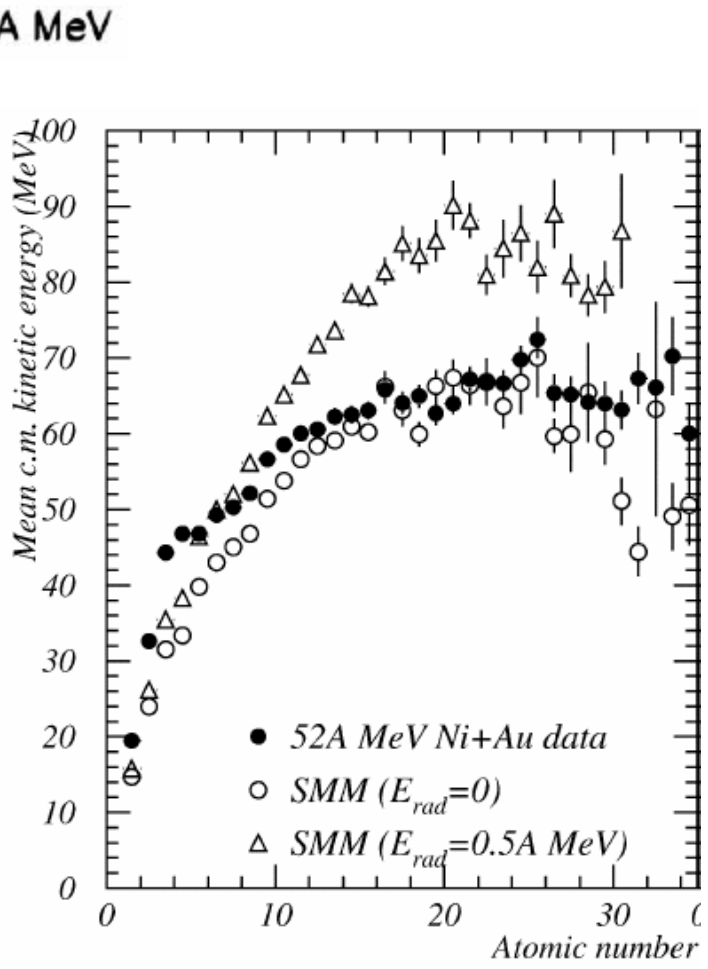

Fig. 10. Atomic number (a) for the 52*A* MeV Ni + Au data (symbols) and SMM (histogram), LCP multiplicity ($Z \leqslant 2$) (b), Fragment multiplicity ($Z \geqslant 6$) (c) and atomic number distributions of the heaviest fragment (d). These comparisons are made in a restricted angular domain in the center of mass (60°–120°). All spectra are normalized to the number of events.

Nuclear Physics A 709 (2002) 367–391

Physics Letters B 371 (1996) 175–180

Statistical multifragmentation in central Au + Au collisions at 35 MeV/u

MINIBALL + MULTICS

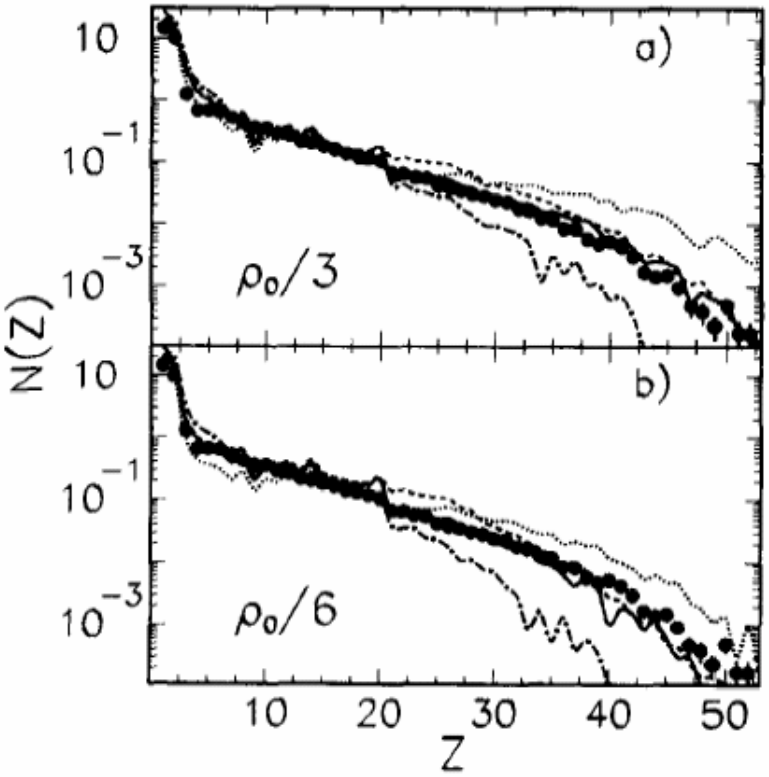

Fig. 1. Charge distribution $N(Z)$. Points show experimental data and lines show results of SMM predictions for sources with parameters $A_s = 343$, $Z_s = 138$, $E_s^*/A = 6.0$ MeV, $\rho_s = \rho_0/3$ (part a)) and $A_s = 315$, $Z_s = 126$, $E_s^*/A = 4.8$ MeV, $E_{flow}/A = 0.8$ MeV, $\rho_s = \rho_0/6$ (part b)). Dashed curves are the unfiltered calculations and solid curves are the filtered ones. The dot-dashed and dotted curves represent filtered calculations for thermal excitations $E_s^*/A + 1$ MeV/u and $E_s^*/A - 1$ MeV/u, respectively.

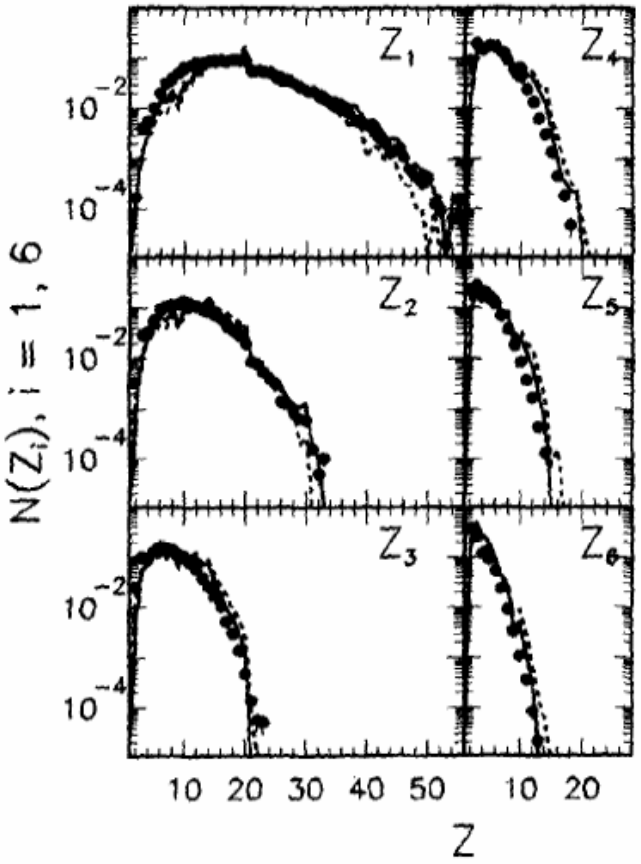

Fig. 2. Charge distribution of the six heaviest fragments, ordered such as $Z_i \geq Z_k$ if $i < k$. Experimental data are shown by points, the solid and dashed curves show the results of SMM calculations for $\rho_s = \rho_0/3$, and $\rho_s = \rho_0/6$, respectively (other source parameters as in Fig. 1).

MINIBALL + MULTICS

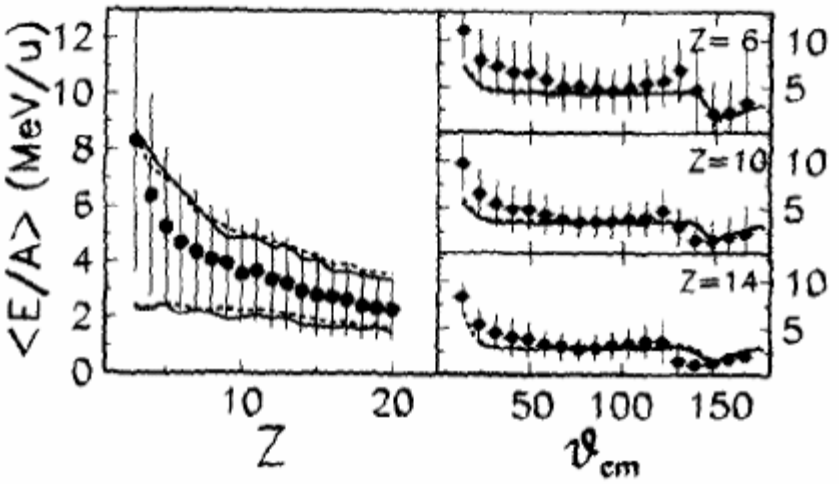

Fig. 3. Mean centre-of-mass kinetic energy per nucleon, $\langle E/A \rangle$, as a function of the charge Z, for fragments emitted at $\theta_{cm} = 90° \pm 10°$ (left panel) and (for $Z = 6, 10, 14$) as a function of θ_{cm} (right panels). Points give the experimental values of $\langle E/A \rangle$ and vertical bars give the standard deviations $\Delta E/A$ of the distributions. The solid and dashed lines are SMM predictions of $\langle E/A \rangle$ (in the left panel show the two values $\langle E/A \rangle \pm \Delta E/A$) for $\rho_s = \rho_0/3$, and $\rho_s = \rho_0/6$, respectively (other source parameters as in Fig. 1). The energy range is the same in the left and in each right panel.

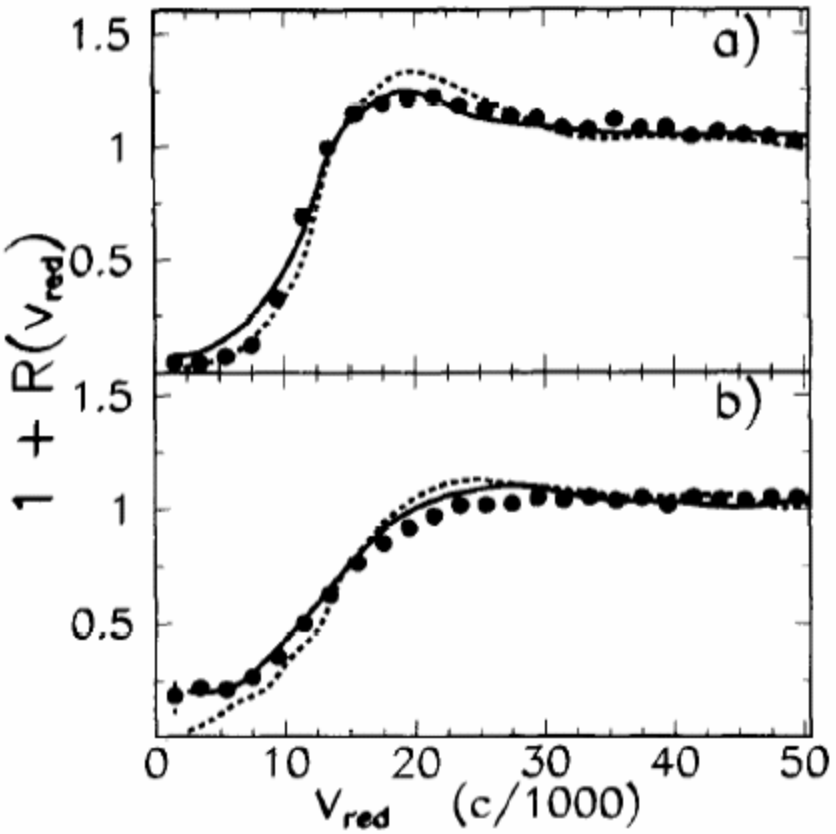

Fig. 4. Two-fragment correlation functions $1 + R(v_{red})$ for $3 \leq Z \leq 30$ and $8° \leq \theta_{lab} < 23°$ (part a)) and for $3 \leq Z \leq 10$ and $23° \leq \theta_{lab} \leq 40°$ (part b)). Full points show experimental data. The solid and dashed lines are SMM predictions for $\rho_s = \rho_0/3$, and $\rho_s = \rho_0/6$ (other source parameters as in Fig. 1).

Eur. Phys. J. A 3, 75–83 (1998)

Thermal multifragmentation in p + Au interactions at 2.16, 3.6 and 8.1 GeV incident energies

FASA

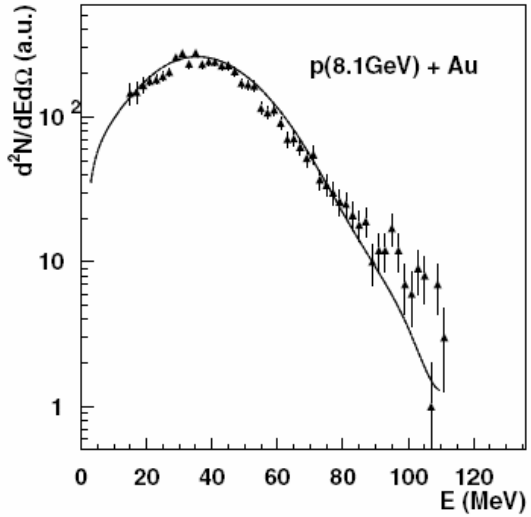

Fig. 8. Energy distribution of carbon isotopes obtained at 8.1 GeV incident energy compared to the one from the INC+Expansion+SMM calculation

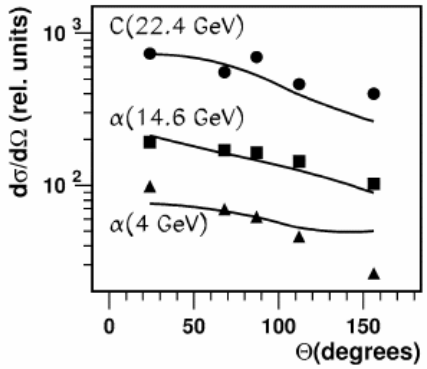

Fig. 9. Angular distributions of carbon (in laboratory system) for ^{4}He + Au and ^{12}C + Au collisions. The lines are calculated with RC + α + SMM.

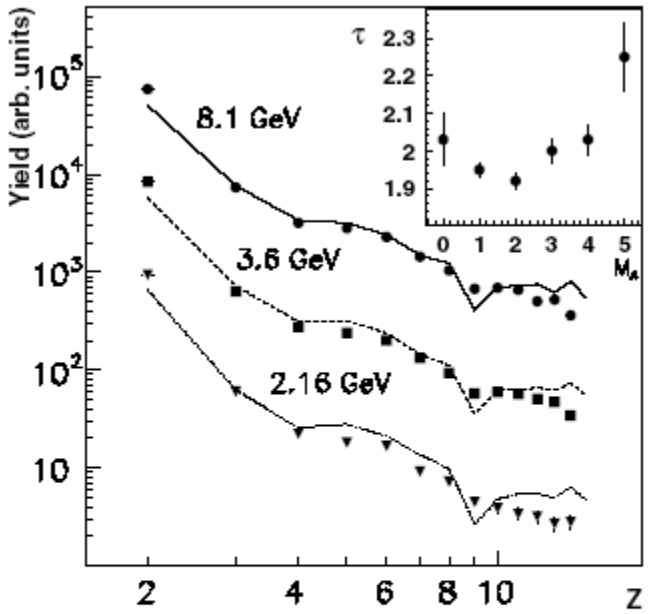

Fig. 10. Fragment charge distributions at the beam energies 8.1 GeV (top), 3.6 GeV (scaled by 1/4) and 2.16 GeV (scaled by 1/16). The lines are calculated by INC+Expansion+SMM (normalized at Z=3). The insert gives the τ-parameter deduced from the IMF-charge spectra for the beam energy of 8.1 GeV as a function of the measured IMF multiplicity

experiment: J.R.Grover, Phys.Rev. **126**(1962)1540
S.Kaufman et al., Phys.Rev. **C14**(1976)1121

FRS @ GSI

Nuclear Physics **A507** (1990) 649–674

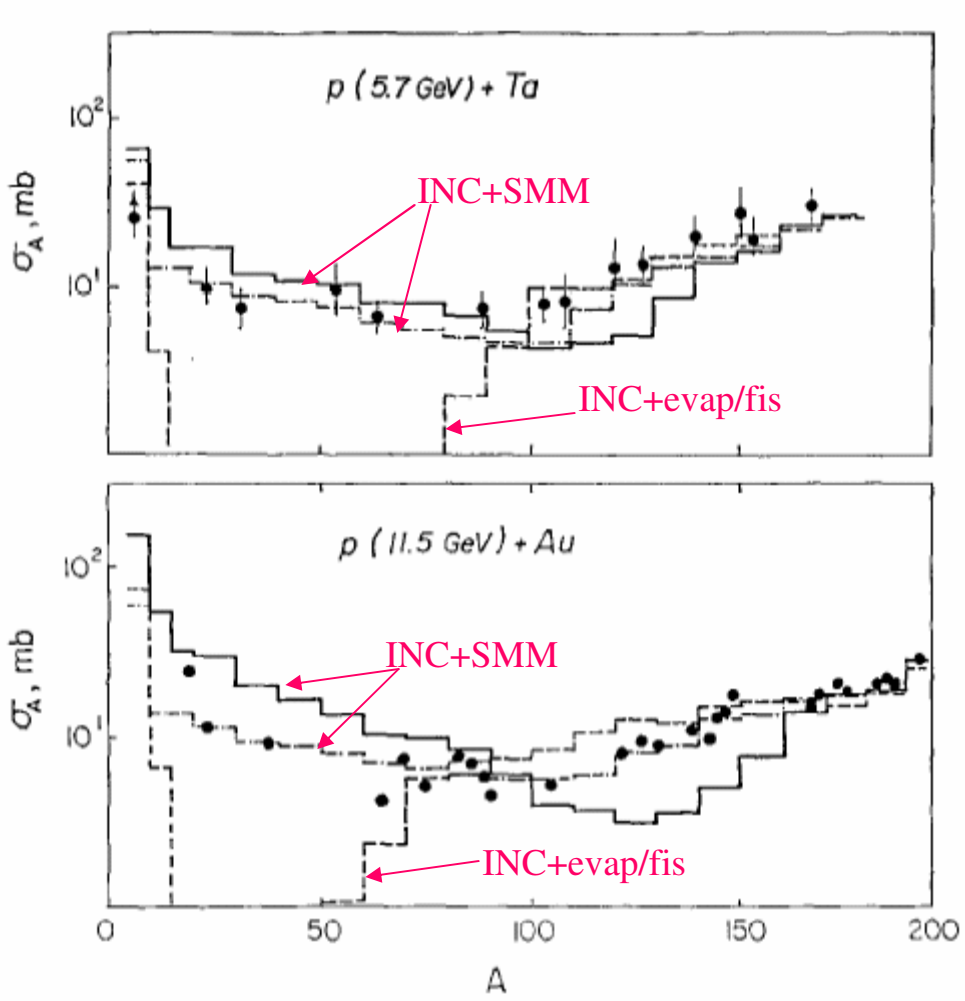

PHYSICAL REVIEW C **70**, 054607 (2004)

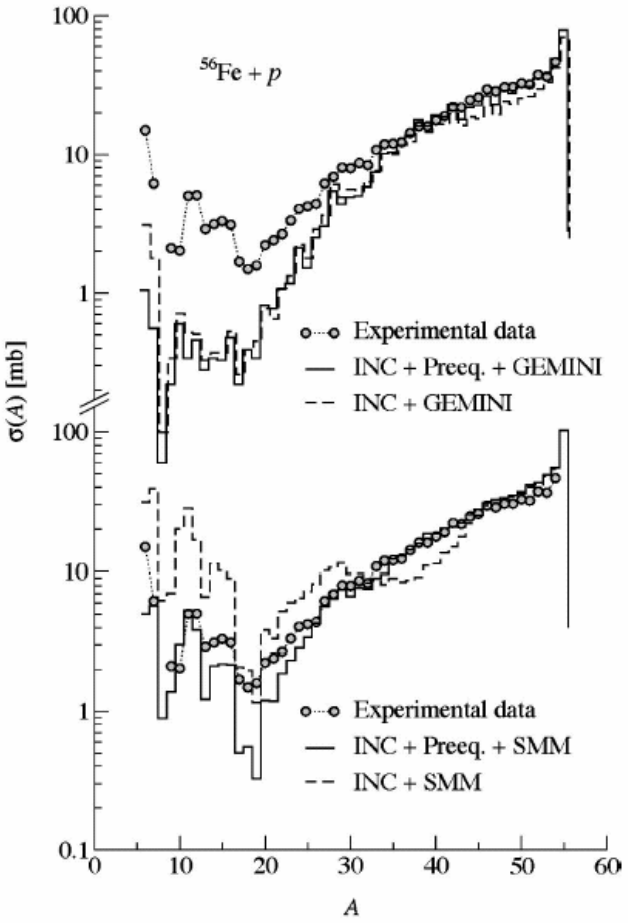

FIG. 15. Comparison of the measured mass distributions as a function of the mass number for the system ^{56}Fe+p with the results of GEMINI (upper part) and SMM (lower part). SMM is more sensitive than GEMINI to the effect of a pre-equilibrium phase.

Multifragmentation versus sequential evaporation

ISIS π^-(8GeV/c)+Au

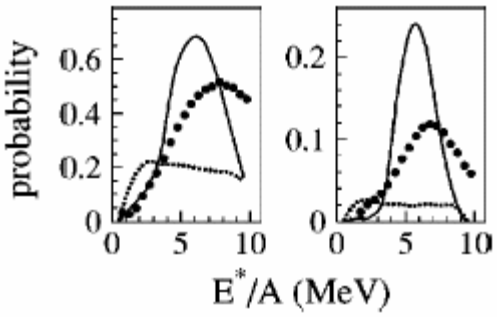

FIG. 3. Left panel: dots present the raw measured probability to detect an event with at least one heavy-fragment, $Z \geqslant 8$, and solid (dotted) line presents the SMM (GEMINI) model prediction filtered with the experimental detection efficiency. An initial angular momentum of $L = 20\hbar$ for the hot nucleus was assumed for GEMINI model calculations. Right panel: as in left panel, but for the probability of detecting events with at least two heavy-fragments, $Z \geqslant 8$.

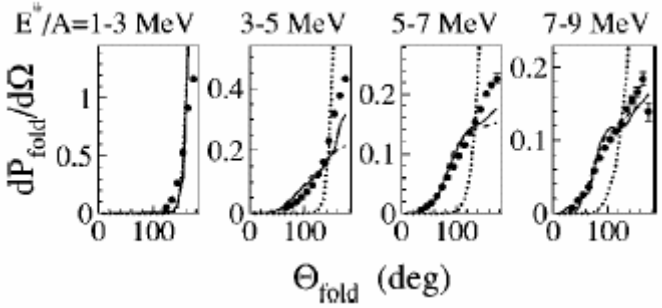

FIG. 2. The measured folding-angle (the angle between two $Z \geqslant 8$ fragments) probability for the indicated excitation-energy bins. Solid, dashed, and dotted lines show the SMM-hot, SMM-cold, and GEMINI model predictions, respectively, filtered with the experimental detection efficiency.

ALADIN Au(600MeV/n)+Cu

Principal component analysis

Nuclear Physics A 604 (1996) 183–207

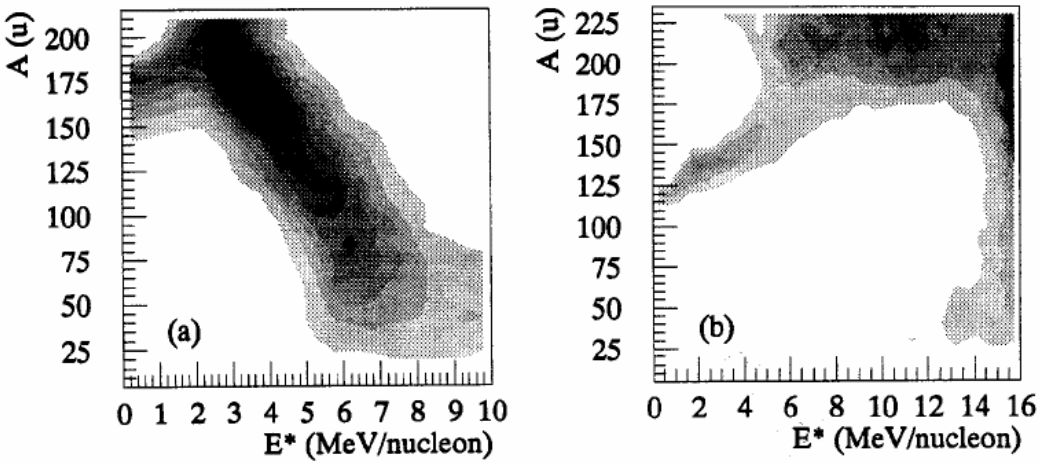

Fig. 4. Source variable correlated distributions $\mathcal{S}_{\infty}(E^*, A)$ for (a) the SMM model and (b) the Gemini model, corresponding to the ALADIN sample of events. The mass of the parent nucleus is denoted by A and its excitation energy by E^*. The observable CPDF used in the backtracing procedure is $\mathcal{O}_{\exp}(Z_{b3}, M)$.

SMM:

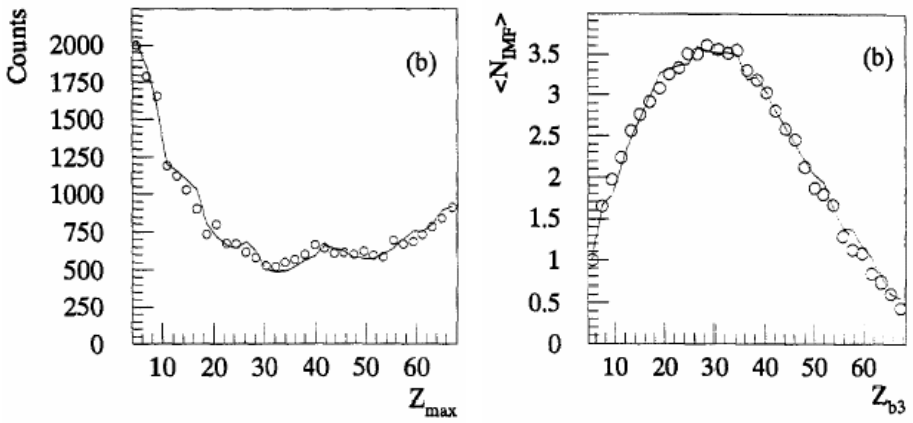

Multifragmentation versus sequential evaporation

ISIS π^-(8GeV/c)+Au

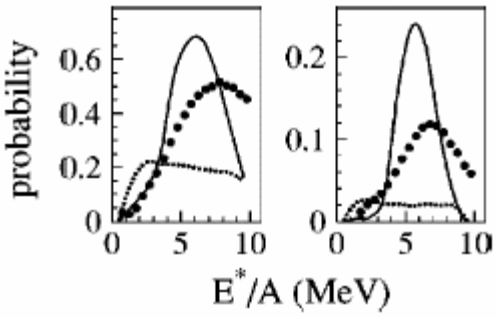

FIG. 3. Left panel: dots present the raw measured probability to detect an event with at least one heavy-fragment, $Z \geqslant 8$, and solid (dotted) line presents the SMM (GEMINI) model prediction filtered with the experimental detection efficiency. An initial angular momentum of $L = 20\hbar$ for the hot nucleus was assumed for GEMINI model calculations. Right panel: as in left panel, but for the probability of detecting events with at least two heavy-fragments, $Z \geqslant 8$.

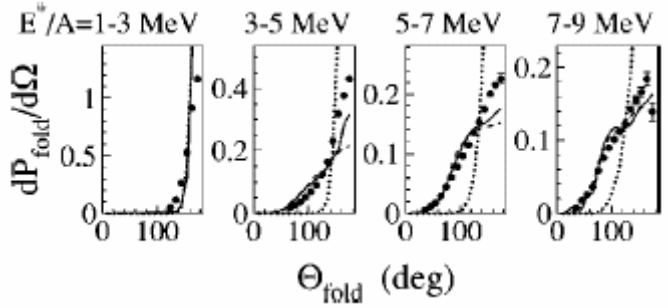

FIG. 2. The measured folding-angle (the angle between two $Z \geqslant 8$ fragments) probability for the indicated excitation-energy bins. Solid, dashed, and dotted lines show the SMM-hot, SMM-cold, and GEMINI model predictions, respectively, filtered with the experimental detection efficiency.

ALADIN Au (600 MeV/n) +X.

Nuclear Physics A556 (1993) 672–696

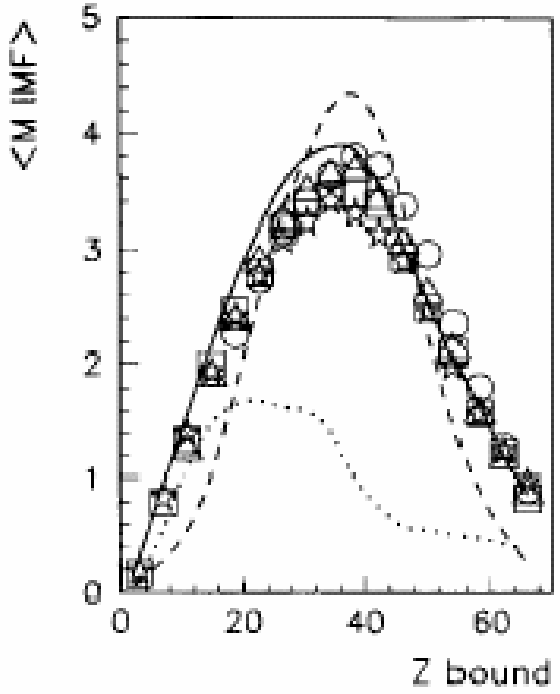

Fig. 15. The average multiplicity of IMFs as a function of Z_{bound} for Au 600 MeV/nucleon collisions on C (circles), Al (triangles), Cu (squares) and Pb (stars). The error bars are in most cases smaller than the size of the symbols. The lines are COPENHAGEN (dashed), GEMINI (dotted) and percolation (full) predictions.

Nuclear Physics A734 (2004) 545–548

Proton energy spectra

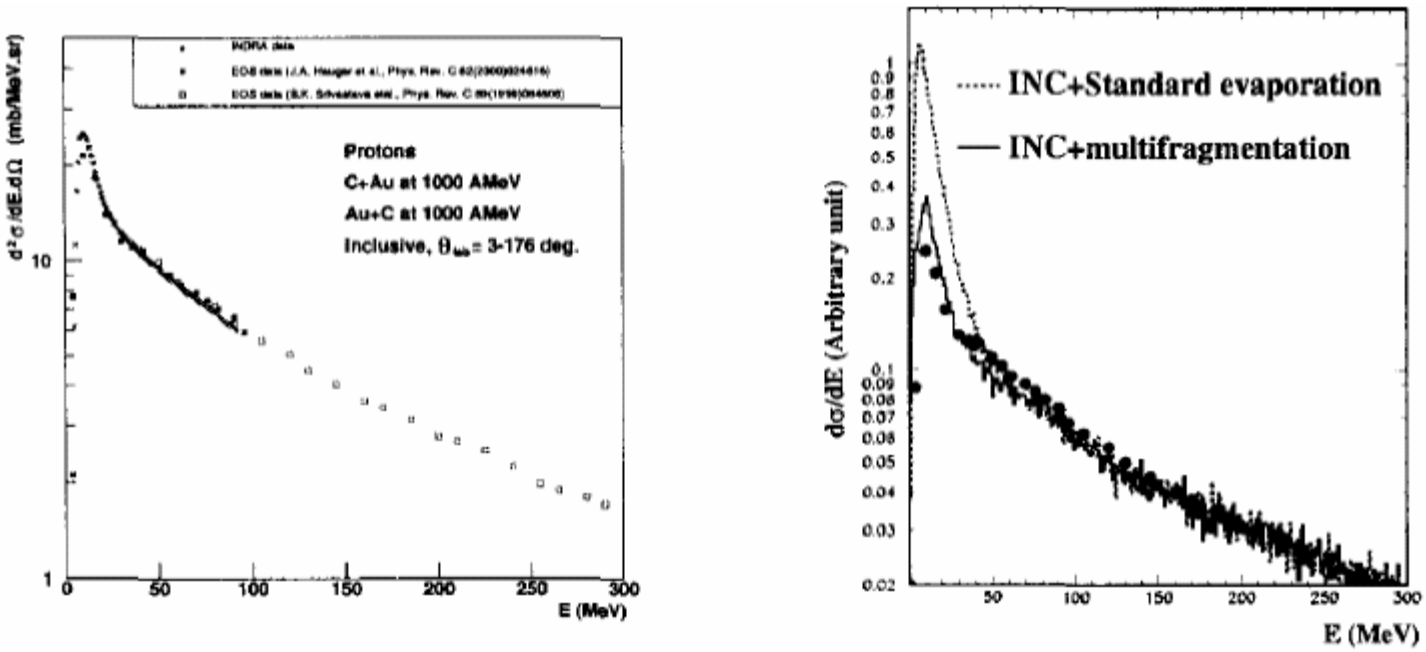

Figure 1. *Left part: The INDRA proton kinetic energy spectrum (full dots) for the C+Au reaction at 1. GeV/nucleon for angle-integrated data between* $3^0 \leq \theta_{lab} \leq 176^o$, *is compared to the EOS spectra (full and empty squares from [4] and [5] respectively). Data are in the gold reference frame. Right part: Comparison between proton EOS data and calculations with the INC+percolation model followed by the Dresner evaporation code (dashed line) or the multi-fragmentation SMM model (full line). The normalization is done on the high energy part.*

The surface (B_0) and symmetry (γ) energy coefficients in the multifragmentation scenario

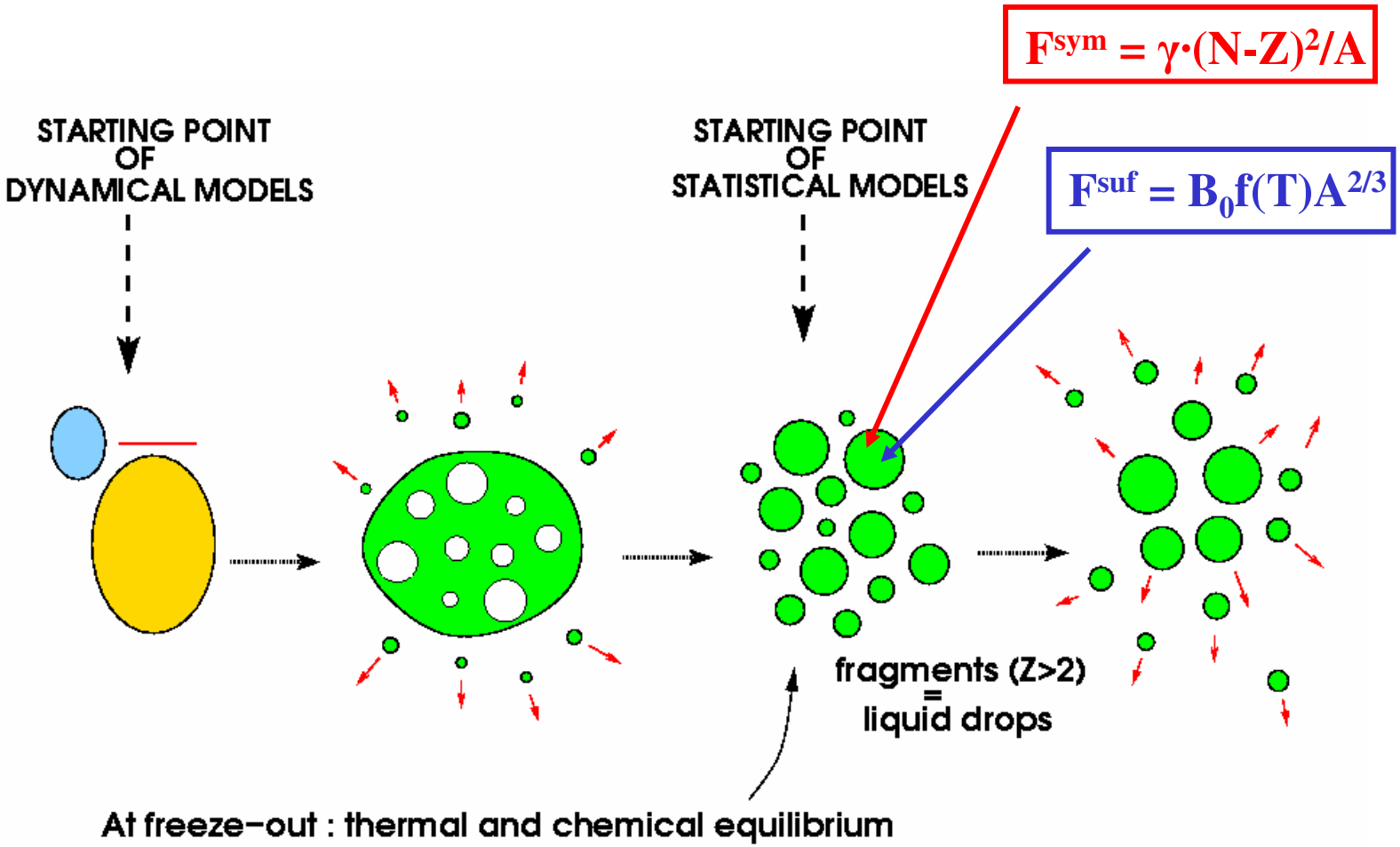

ALADIN: $^{12}C+ ^{112,124}Sn$ A.Le Fevre et al., Phys.Rev.Lett **94**(2005)162701

Evolution symmetry energy toward multifragmentation

$$\mathbf{E_{sym}=\gamma(A-2Z)^2/A}$$

(by analyzing the isoscaling phenomenon)

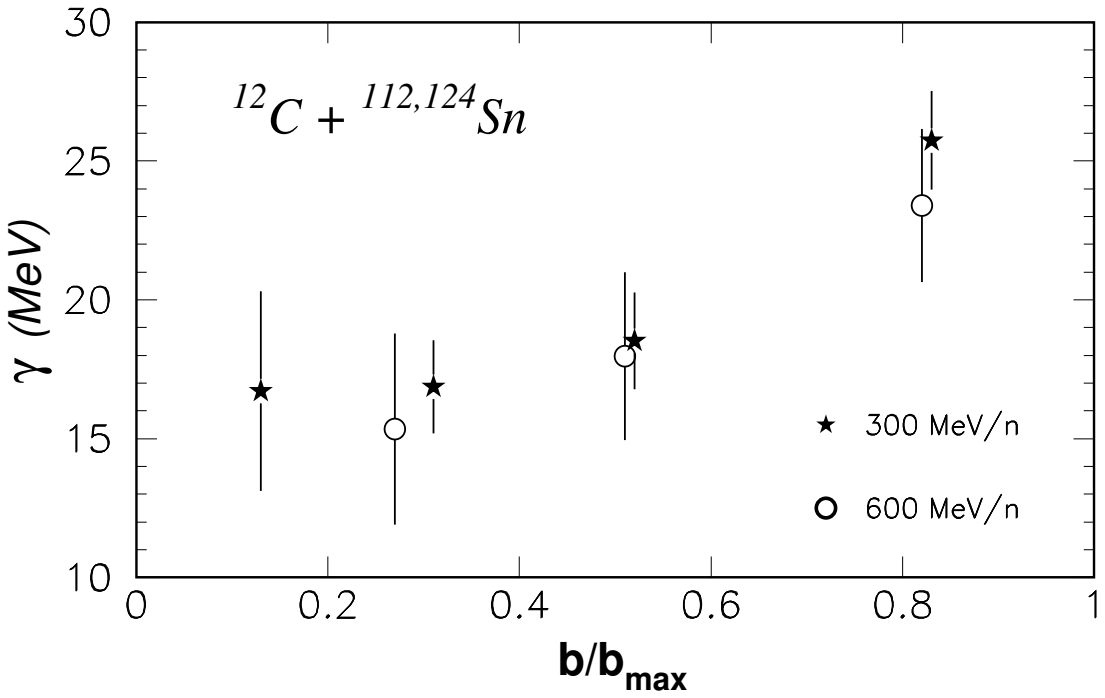

Isoscaling and coefficient γ

ALADIN: $^{12}C+ ^{112,124}Sn$ A.Le Fevre et al., Phys.Rev.Lett 94, 162701 (2005)

$S(N)=Y(^{124}Sn)/Y(^{112}Sn)=C\cdot\exp(N\cdot\alpha+Z\cdot\beta)$ **$\alpha\cdot T \approx -4\gamma\,(Z_1^2/A_1^2-Z_2^2/A_2^2)$**

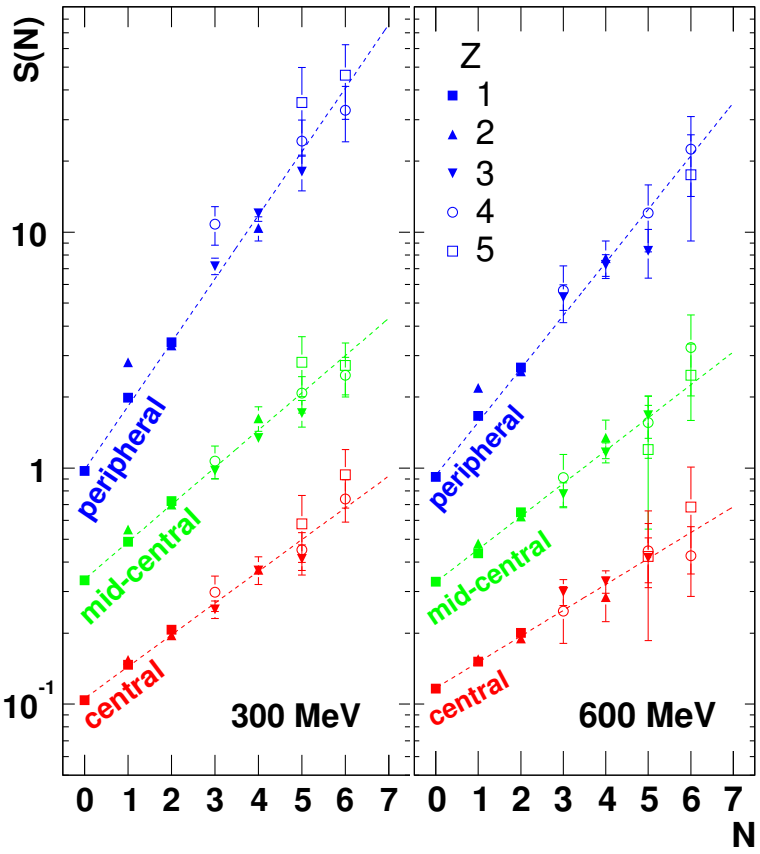

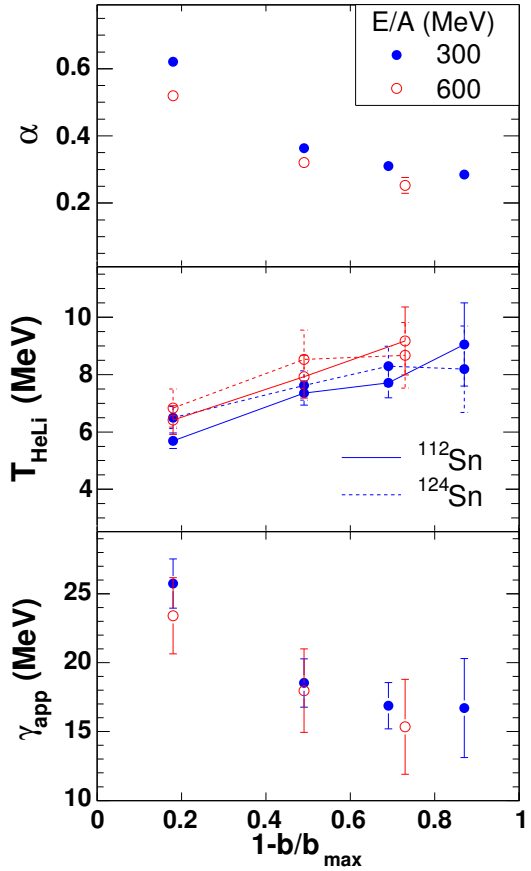

The symmetry energy coefficient γ and isospin of fragments

$$E_{sym}=\gamma(A-2Z)^2/A$$

A.S.Botvina et al., PRC**72**(2005)048801

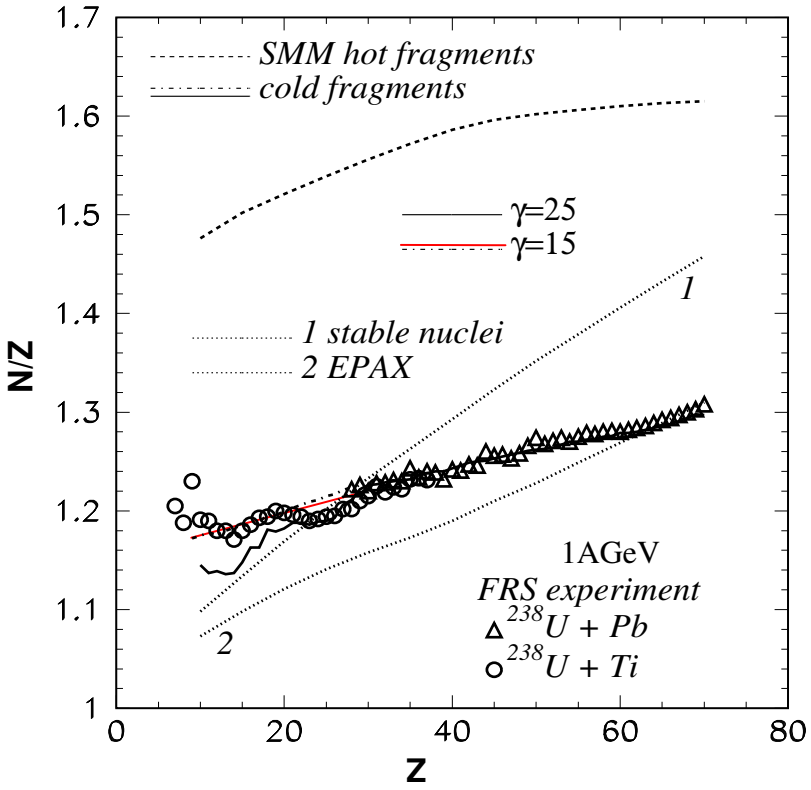

G.Souliotis et al., PRC**75**(2007)011601

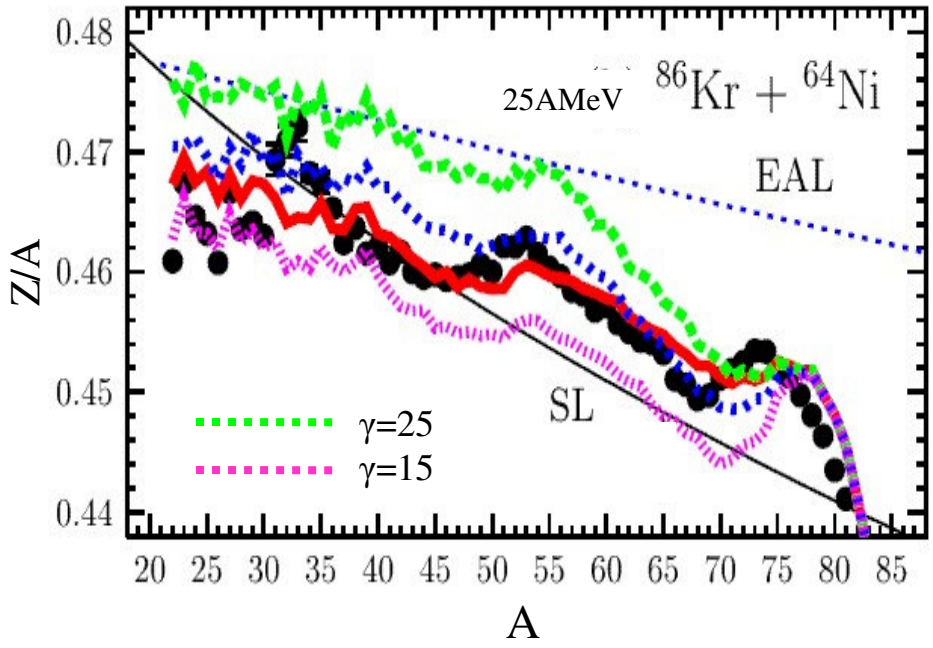

Isotope Distributions

J.Iglio et al. PRC74, 024605 (2006)

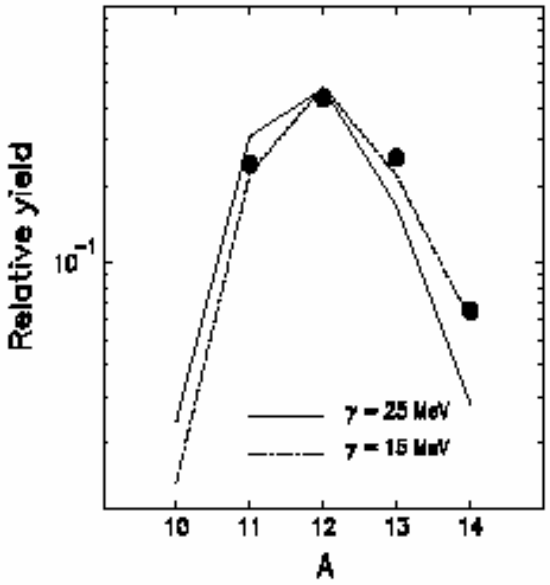

FIG. 12. Isotopic yield distribution for the carbon element in ^{40}Ca+^{58}Ni reaction at 45 MeV/nucleon. The solid line is the SMM calculation with symmetry energy coefficient $\gamma = 25$ MeV, and the dashed line is the calculation with $\gamma = 15$ MeV. The solid points correspond to the experimental result.

G.A.Souliotis et al., PRC75, 011601 (2007)

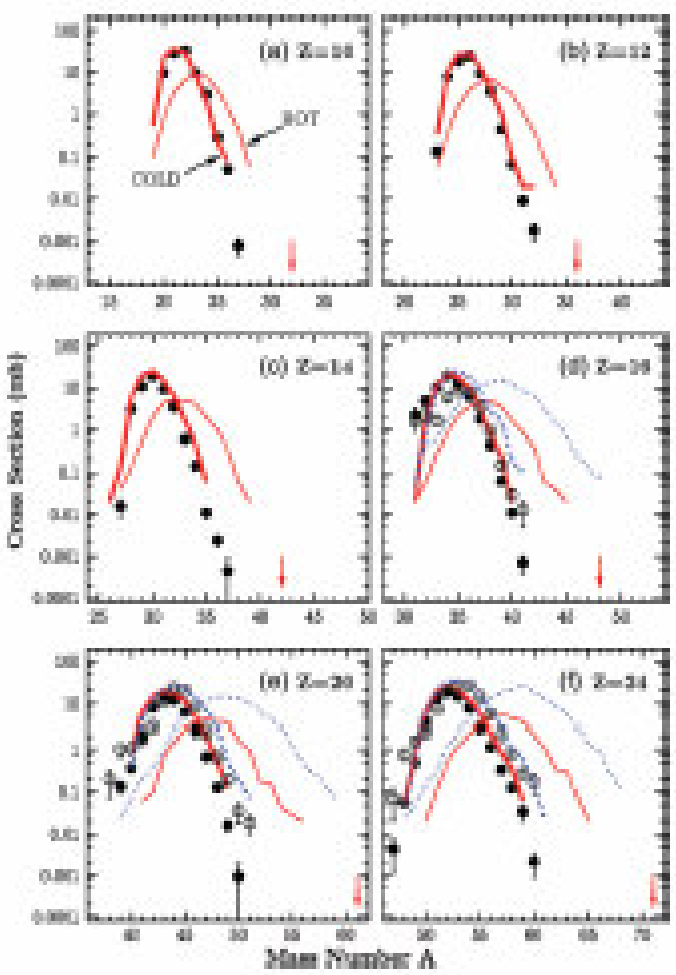

FIG. 4. (Color online) Comparison of experimental mass distributions with DIT/SMMC6 calculations. Solid points: ^{78}Kr+^{58}Ni data. Open points: ^{86}Kr+^{208}Pb data. Full lines: calculations for ^{78}Kr+^{58}Ni; thick: final (cold) fragments, thin: primary (hot) fragments. Dotted lines: calculations for ^{86}Kr+^{208}Pb; thick: final (cold) fragments, thin: primary (hot) fragments. Arrows: neutron drip line [35].

One can distinguish effects of the surface and symmetry energies since the charge yield of fragments is very sensitive to the surface:

A.S.Botvina et al., PRC74(2006)044609

$F^{suf} = B_0((T_c^2-T^2)/(T_c^2+T^2))^{5/4}A^{2/3}$

$F^{sym} = \gamma\cdot(N-Z)^2/A$

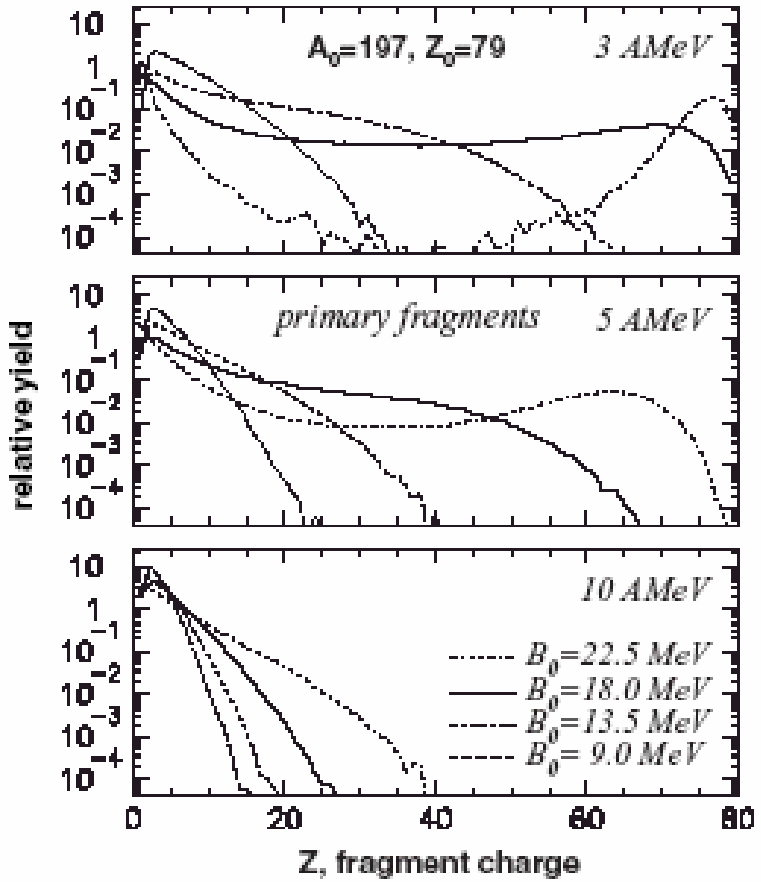

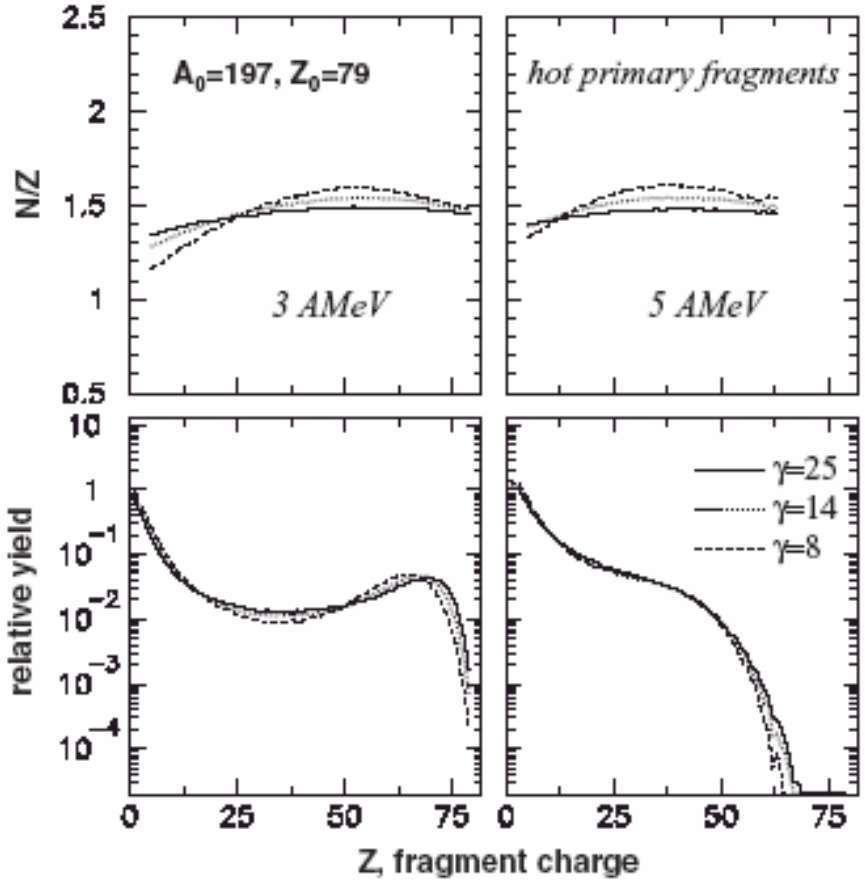

Properties of hot fragments: the surface energy term B_0

$Z^{-\tau}$ analysis of IMF yields

projectiles with different isospin

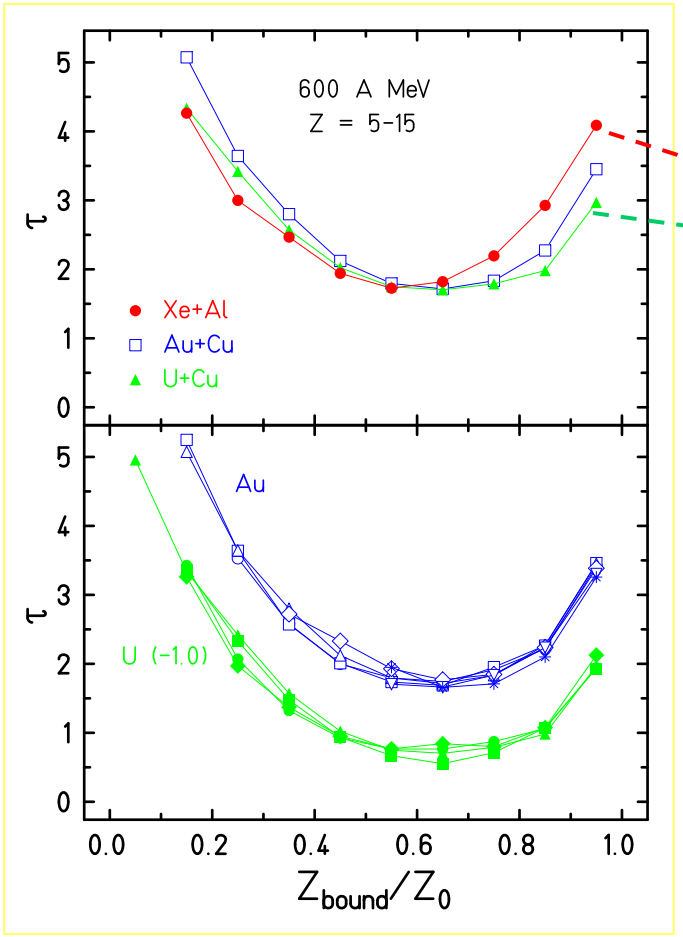

ALADIN

SMM

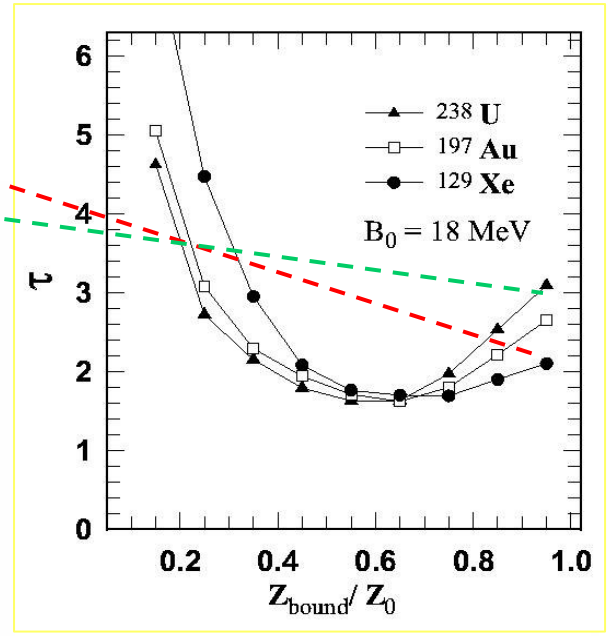

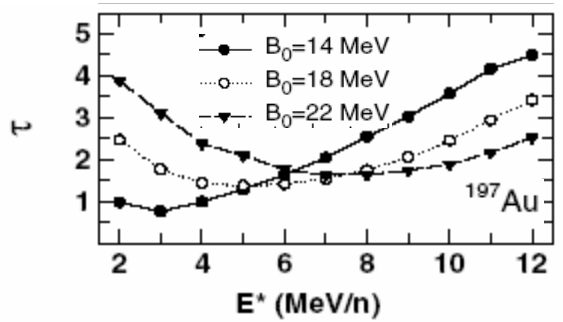

A.S.Botvina et al., PRC74(2006)044609

Evolution of the surface energy toward multifragmentation

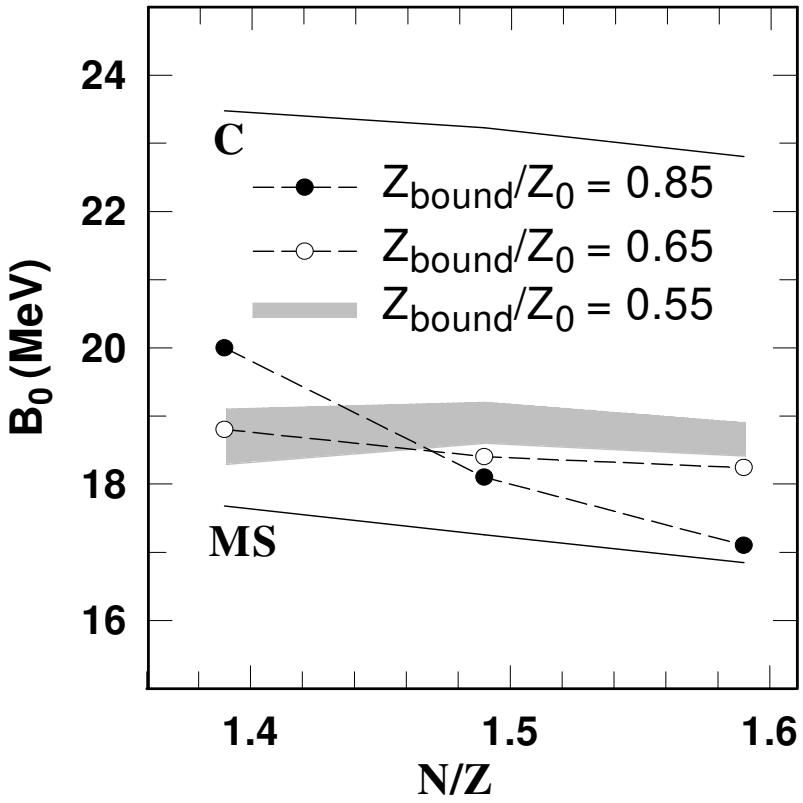

We analyze all available observables: distributions of IMF , Z_{max} , T , ... vs Z_{bound} , and involve additionally new τ - observables for each projectile (Xe, Au, U)

- We have found the isospin independence of the surface energy, that is equivalent to the surface independence of the symmetry energy.

for single isolated nuclei:

C -- Cameron mass formula (1957)
MS -- Myers-Swiatecki mass formula (1966)

(include separate volume and surface contributions to the symmetry energy)

Conclusions on nuclear multifragmentation:

Multifragmentation of nuclei is fast decay process taking place in all reactions where high excitation energy is reached. It dominates over sequential evaporation and fission which are usual at low energy.

Multifragmentation takes as much as 10-15% of the total cross section in high energy hadron nucleus reactions, and much more for high energy nucleus-nucleus collisions. It must be included in hybrid calculations of particle transport in complex matter: nuclear transmutation (environment studies), electro-nuclear breeding (new methods of energy production), proton and ion therapy (medical research), radiation protection of space detectors (space research). Multifragmentation can be the dominating channel for production of some particular isotopes.

Multifragmentation can be interpreted as a manifestation of the liquid-gas type phase transition in finite nuclei, and it allows for investigating the phase diagram of nuclear matter. In particular, one can investigate properties of hot nuclei/fragments surrounded by other nuclear species.

Outlooks for description of spallation reactions:

1) Excited residuals produced after initial dynamical stage should be investigated in details. Their distributions in mass number, excitation energy and isospin are of primary importance for the following statistical fragment production mechanisms: evaporation, fission, multifragmentation.

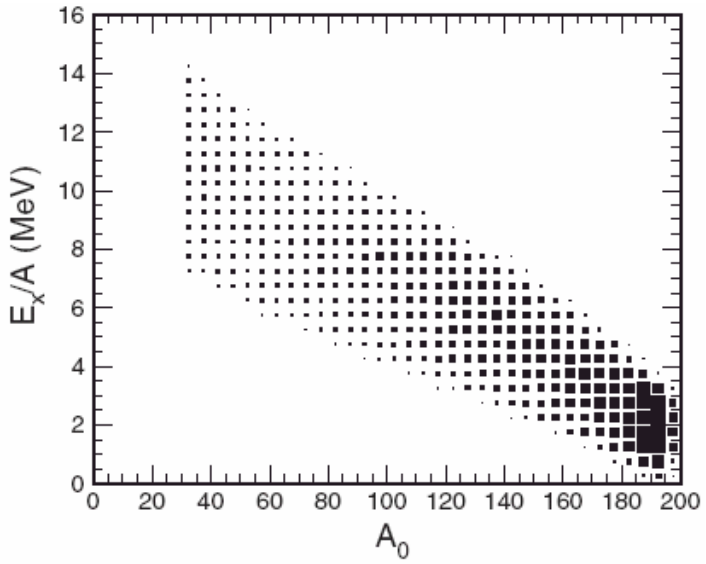

It is necessary to find out how the distribution of residuals evolve with beam energy, target, projectile. This should be combined experimental + theoretical studies. Without this knowledge the secondary stages responsible for fragment production can not give precise answer.

Example of residuals extracted for ALADIN
Au(600MeV/n)+Au peripheral collisions

Outlooks for description of spallation reactions:

2) Intermediate mass fragments (IMF) are predominantly produced at high excitation energies of residuals. Therefore, they can be used for investigation of the high energy limit for these residuals. This also can help to understand what parameters have residuals at low and intermediate (1-4 MeV/n) energies, since their transformation in (A,Z)-Ex plane is continuous.

3) Transition from sequential evaporation/fission to fast simultaneous multifragmentation (at 2-4 MeV/nucleon) must be investigated in details: This would allow for fixing parameters of statistical models

4) Future of fragmentation reactions is isotope measurements and fragment correlations. These data improve considerably our knowledge about reaction mechanisms. Whereas inclusive data do not always allow for unambiguous interpretation.

System- A_0, Z_0, E_0, V

Ensemble of partitions {f: N_{AZ}, $1 \le A \le A_0$, $0 \le Z \le Z_0$}

Microcanonical	Canonical	Macrocanonical
$\Sigma A N_{AZ} = A_0$	$\Sigma A N_{AZ} = A_0$	$\Sigma A \langle N_{AZ} \rangle = A_0$
$\Sigma Z N_{AZ} = Z_0$	$\Sigma Z N_{AZ} = Z_0$	$\Sigma Z \langle N_{AZ} \rangle = Z_0$
$E_f(N_{AZ}, T_f, V) = E_0$	$\langle E_f(N_{AZ}, T_f, V) \rangle = E_0$	$\langle E_f(\langle N_{AZ} \rangle, T_f, V) \rangle = E_0$
$W_f^{mic} \approx \exp S_f(E_0, V, A_0, Z_0)$	$W_f^{can} \approx \exp(-\frac{F_f(T, V, A_0, Z_0)}{T})$	$W_f^{mac} \approx \exp(-\frac{F_f(T, V, A_0, Z_0) - \mu \Sigma A - \upsilon \Sigma Z}{T})$

Schematic classification of statistical ensembles used for describing break-up of the nuclear system with mass number A_0, charge Z_0 and total energy E_0 in a volume V.

Chimera, 35 MeV/N

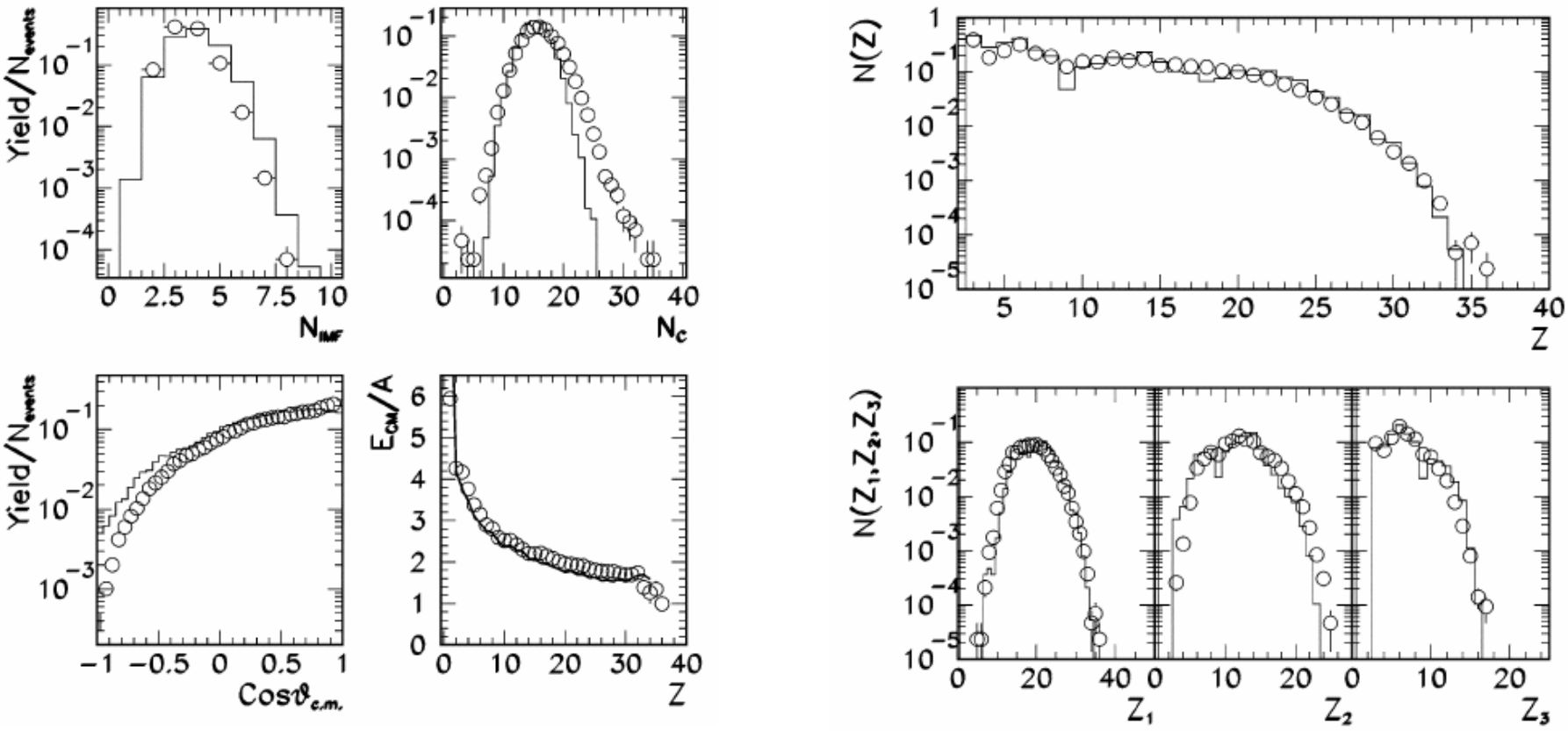

Fig. 11. IMF multiplicity, total-charged particle multiplicity, fragments $\cos(\theta_{\mathrm{c.m.}})$ distribution, and mean kinetic energy per nucleon in the CM reference frame as a function of the fragment charge. Circles represent data, lines show SMM-filtered predictions for central $^{112}\mathrm{Sn} + {}^{58}\mathrm{Ni}$ collisions.

Fig. 12. Charge distribution and charge partition, i.e., charge distributions of the heaviest three fragments in each event ($Z_1 \geqslant Z_2 \geqslant Z_3$). Circles represent data, lines show SMM-filtered predictions for central $^{112}\mathrm{Sn} + {}^{58}\mathrm{Ni}$ collisions.

Statistical fragmentation of Au projectiles at $E/A = 600$ MeV

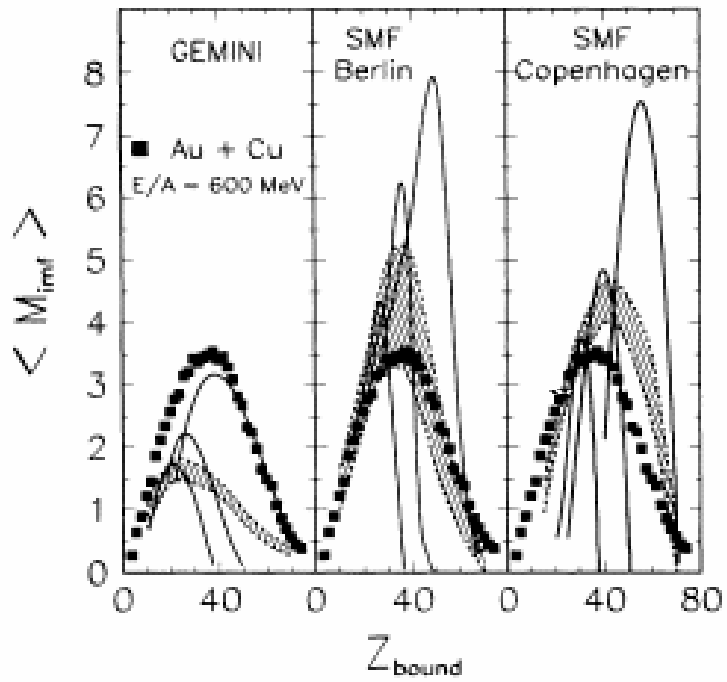

FIG. 3. Comparison of the $\langle M_{\mathrm{IMF}} \rangle$-$Z_{\mathrm{bound}}$ correlation observed for Au + Cu reactions (squares) with predictions of the sequential decay code GEMINI (left part) and of the statistical multifragmentation models of Gross and co-workers (center part) and of Bondorf and co-workers (right part). The lines represent excitation functions for different initial systems $(A_1, Z_1) = (100,40)$, (131,54), and (190,75). The shaded bands are predictions based on initial conditions provided by BUU simulations.

SMM for ALADIN

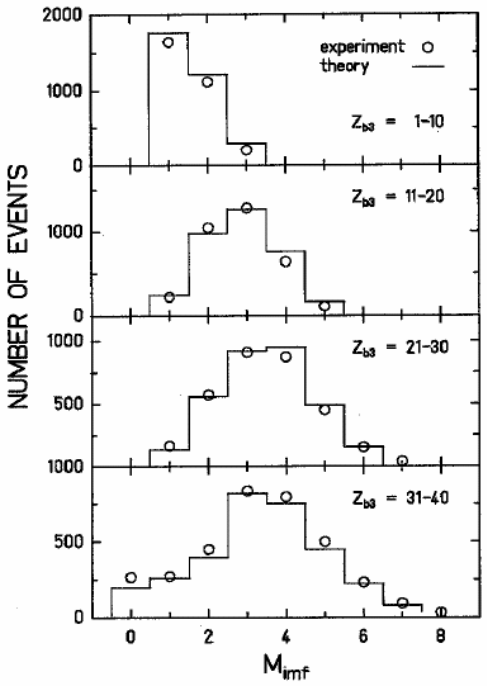

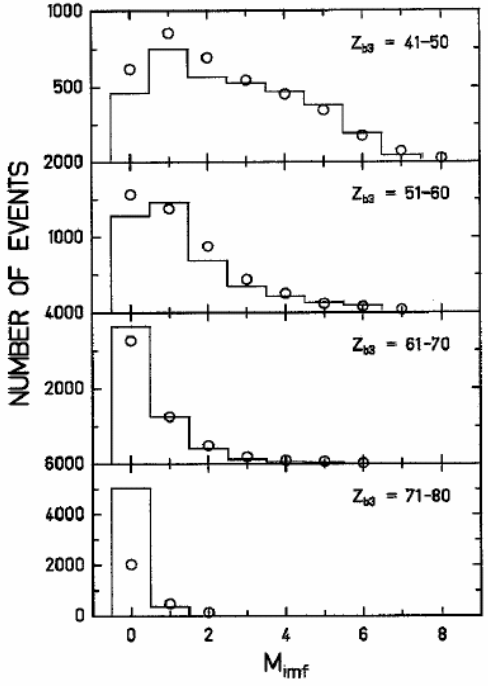

A.S.Botvina et al.,
Nucl.Phys. A584(1995)737

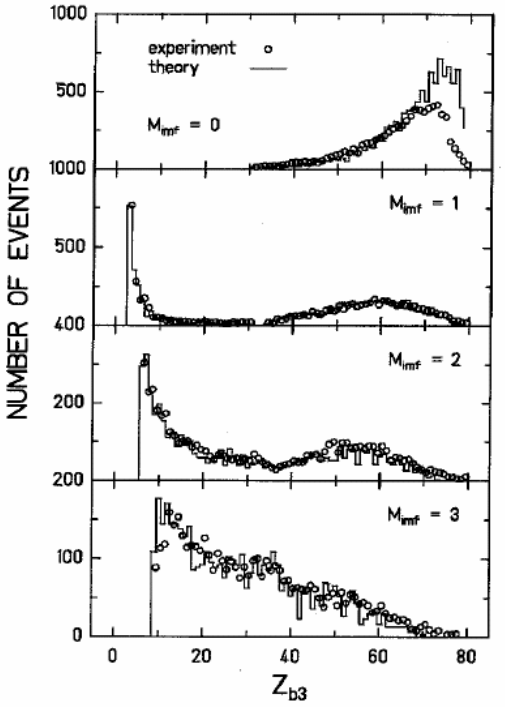

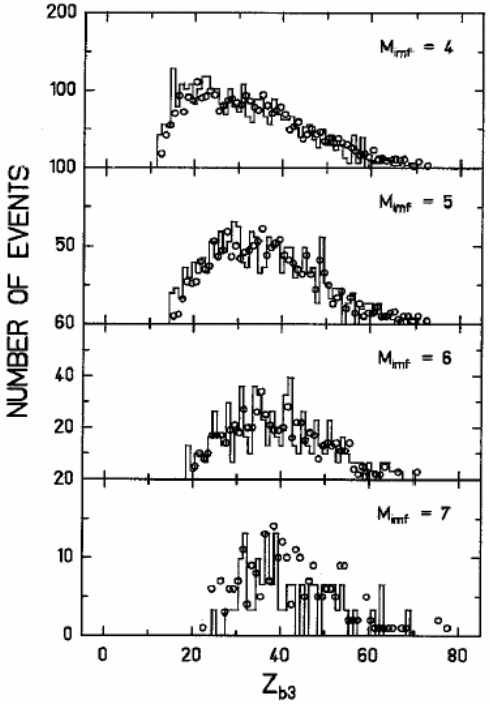

SMM for ALADIN

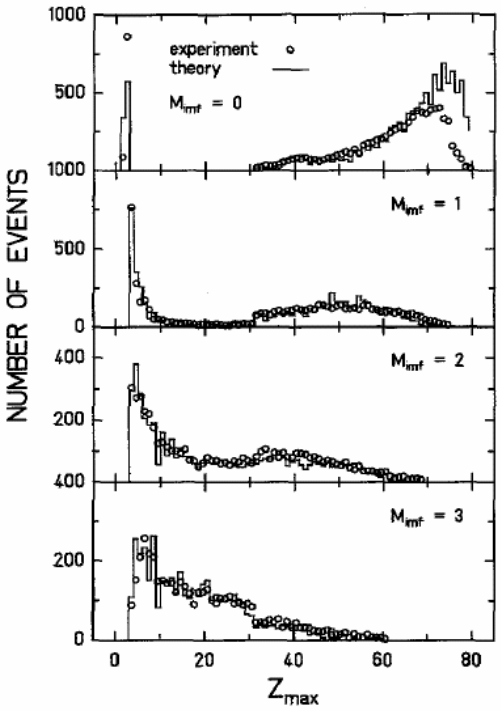

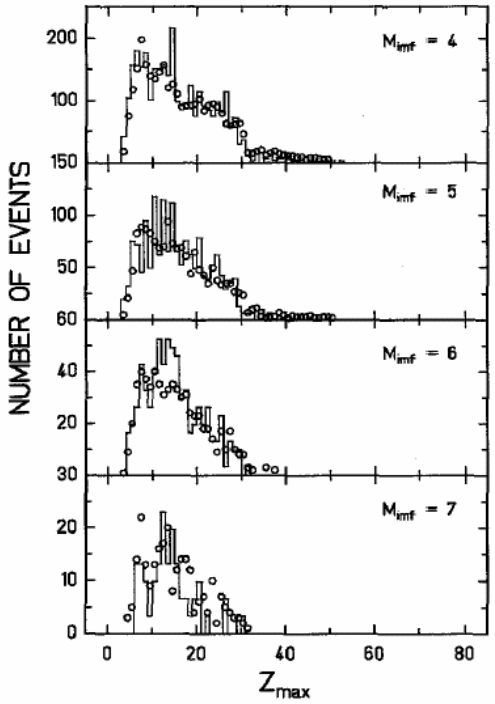

A.S.Botvina et al.,
Nucl.Phys. A584(1995)737

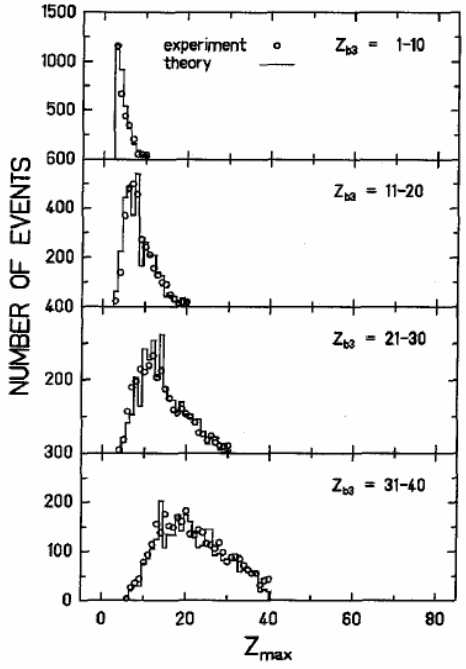

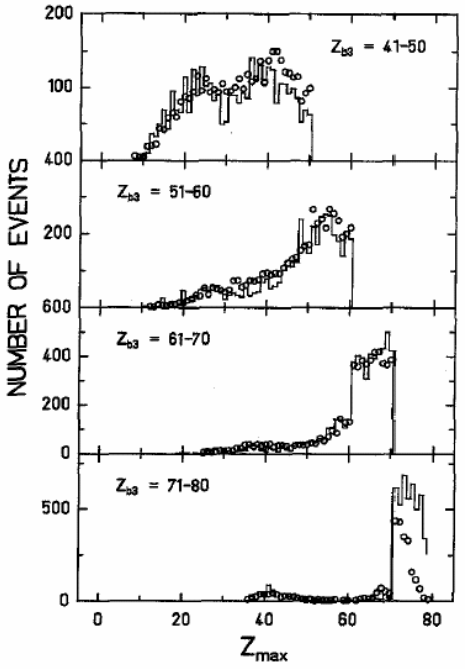

4.3.2. The Fermi break-up

For light primary fragments (with $A \leq 16$) even a relatively small excitation energy may be comparable with their total binding energy. In this case we assume that the principal mechanism of de-excitation is the explosive decay of the excited nucleus into several smaller clusters (the secondary break-up). To describe this process we use the famous Fermi model [105]. It is analogous to the above-described statistical model, but all final-state fragments are assumed to be in their ground or low excited states. In this case the statistical weight of the channel containing n particles with masses m_i $(i = 1, \ldots, n)$ in volume V_f may be calculated in microcanonical approximation:

$$\Delta\Gamma_f^{\text{mic}} \propto \frac{S}{G}\left(\frac{V_f}{(2\pi\hbar)^3}\right)^{n-1}\left(\frac{\prod_{i=1}^n m_i}{m_0}\right)^{3/2}\frac{(2\pi)^{(3/2)(n-1)}}{\Gamma(\frac{3}{2}(n-1))}\left(E_{\text{kin}} - U_f^C\right)^{(3/2)n-5/2}, \tag{58}$$

where $m_0 = \sum_{i=1}^n m_i$ is the mass of the decaying nucleus, $S = \prod_{i=1}^n (2s_i + 1)$ is the spin degeneracy factor (s_i is the ith particle spin), $G = \prod_{j=1}^k n_j!$ is the particle identity factor (n_j is the number of particles of kind j). E_{kin} is the total kinetic energy of particles at infinity which is related to the prefragment excitation energy E_{AZ}^* as

$$E_{\text{kin}} = E_{AZ}^* + m_0c^2 - \sum_{i=1}^n m_ic^2. \tag{59}$$

U_f^C is the Coulomb interaction energy between cold secondary fragments given by Eq. (49), U_f^C and V_f are attributed now to the secondary break-up configuration.

$$\Omega = \int \frac{V^M\, \mathrm{d}^3\boldsymbol{p}_1 \cdots \mathrm{d}^3\boldsymbol{p}_M}{(2\pi\hbar)^{3M}}\delta\left(\sum_{A,Z}\boldsymbol{p}_{AZ}\right)\delta\left(\sum_{A,Z}\frac{p_{AZ}^2}{2m_{AZ}} - \sum_{A,Z}E_{AZ}^{\text{kin}}\right)$$

Fermi-break-up for light nuclei

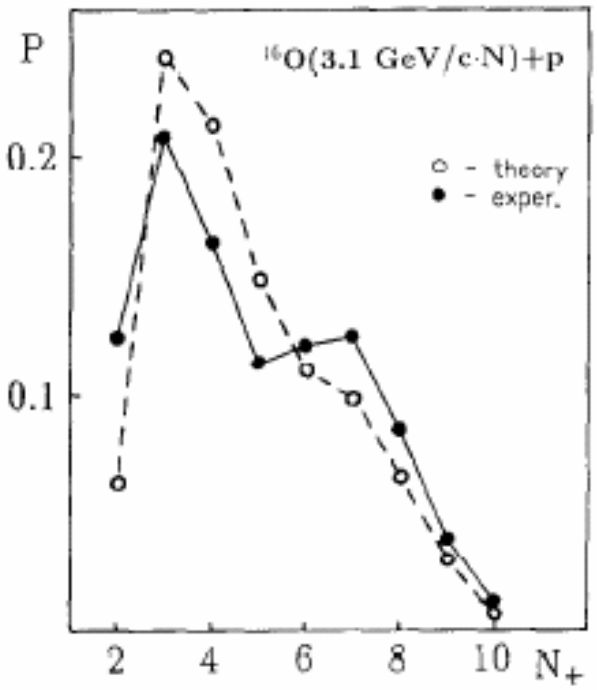

Fig. 6.12. Multiplicity distribution of positively charged particles N_+ produced in ^{16}O(3.1 GeV/c per nucleon) + p reaction. The dots are experimental data from [159]. The open circles are the CFEM calculation.

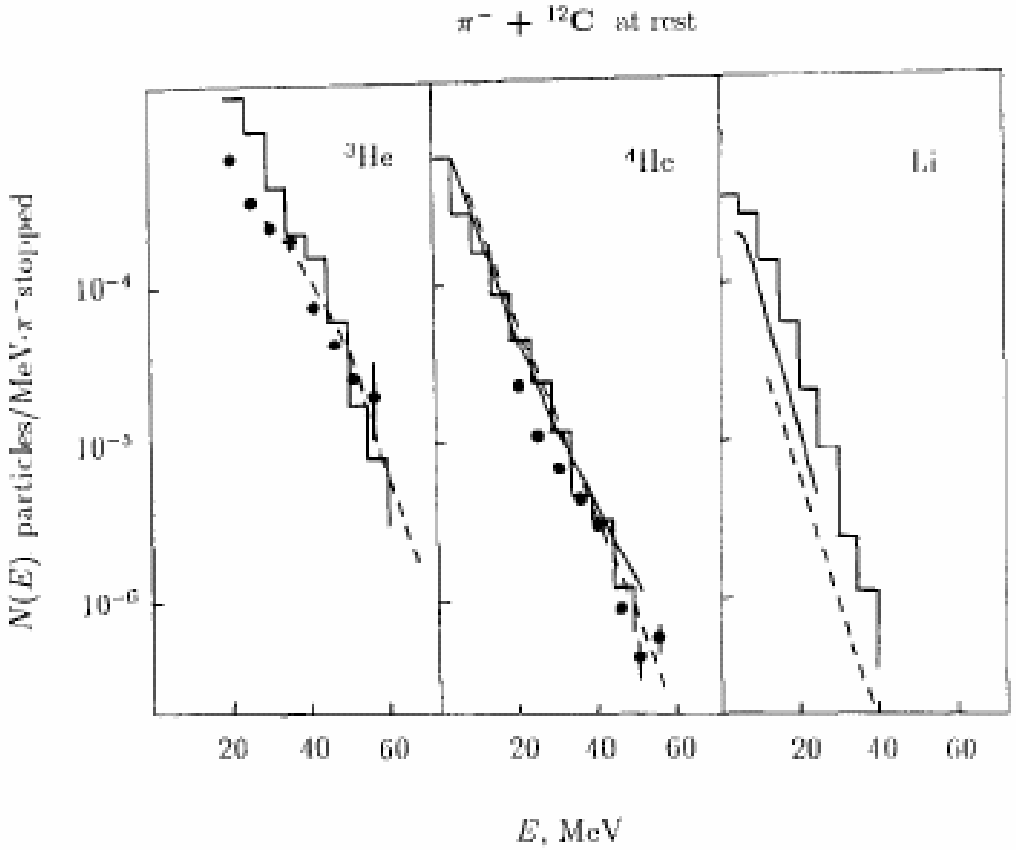

Fig. 6.13. Energy spectra of He and Li fragments produced after absorption of stopped π^--mesons in ^{12}C nucleus. The detected particles are indicated in the figure. The histograms are calculated as described in the text. The experimental data: solid curves [160], dashed curves [161], dots [162].

4.3.3. Evaporation from hot fragments

The successive particle emission from hot primary fragments with $A > 16$ is assumed to be their basic de-excitation mechanism. Due to the high excitation energy of these fragments, the standard Weisskopf evaporation scheme [2] was modified to take into account the heavier ejectiles up to ^{18}O, besides light particles (nucleons, d, t, α), in ground and particle-stable excited states [81]. This corresponds to the excitation energies $\epsilon^{(i)}$ of the ejectiles not higher than 7–8 MeV. By analogy with standard model the width for the emission of a particle j from the compound nucleus (A, Z) is given by

$$\Gamma_j = \sum_{i=1}^{n} \int_0^{E^*_{AZ} - B_j - \epsilon_j^{(i)}} \frac{\mu_j g_j^{(i)}}{\pi^2 \hbar^3} \sigma_j(E) \frac{\rho_{A'Z'}(E^*_{AZ} - B_j - E)}{\rho_{AZ}(E^*_{AZ})} E \, dE \tag{60}$$

Here the sum is taken over the ground and all particle-stable excited states $\epsilon_j^{(i)} (i = 0, 1, \ldots, n)$ of the fragment j, $g_j^{(i)} = (2s_j^{(i)} + 1)$ is the spin degeneracy factor of the ith excited state, μ_j and B_j are corresponding reduced mass and separation energy, E^*_{AZ} is the excitation energy of the initial nucleus (55), E is the kinetic energy of an emitted particle in the centre-of-mass frame. In Eq. (60) ρ_{AZ} and $\rho_{A'Z'}$ are the level densities of the initial (A, Z) and final (A', Z') compound nuclei. They are calculated using the Fermi-gas formula (41). The cross section $\sigma_j(E)$ of the inverse reaction $(A', Z') + j = (A, Z)$ was calculated using the optical model with nucleus–nucleus potential from Ref. [117]. The evaporational process was simulated by the Monte Carlo method using the algorithm described in Ref. [118]. The conservation of energy and momentum was strictly controlled in each emission step.

4.3.4. Nuclear fission

An important channel of de-excitation of heavy nuclei ($A > 200$) is fission. This process competes with particle emission. Following the Bohr–Wheeler statistical approach we assume that the partial width for the compound nucleus fission is proportional to the level density at the saddle point $\rho_{sp}(E)$ [1]:

$$\Gamma_f = \frac{1}{2\pi\rho_{AZ}(E^*_{AZ})} \int_0^{E^*_{AZ}-B_f} \rho_{sp}(E^*_{AZ} - B_f - E)\, dE, \tag{61}$$

where B_f is the height of the fission barrier which is determined by the Myers–Swiatecki prescription [120]. For approximation of ρ_{sp} we used the results of the extensive analysis of nuclear fissility and Γ_n/Γ_f branching ratios [121]. The influence of the shell structure on the level densities ρ_{sp} and ρ_{AZ} is disregarded since in the case of multifragmentation we are dealing with very high excitation energies $E^* > 30$–50 MeV when shell effects are expected to be washed out [122].

sequential evaporation of fragments

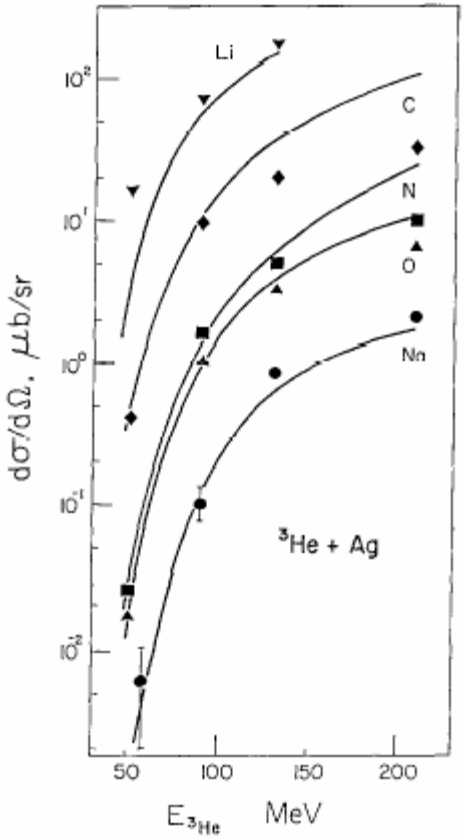

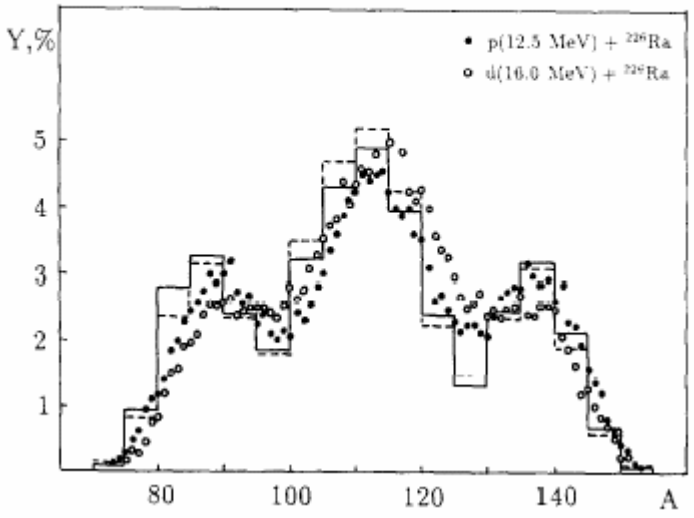

nuclear fission

Fig. 4.1. Cross section for heavy cluster emission at backward angles (θ = 120°–160°) in the reaction ^{3}He+Ag as a function of the laboratory kinetic energy of ^{3}He. The data are from Ref. [119], and the curves show the results of the evaporation model calculation described in the text.

P.Napolitani et al., Phys. Rev. C70 (2004) 054607; Fe (1GeV/N) + H, Ti

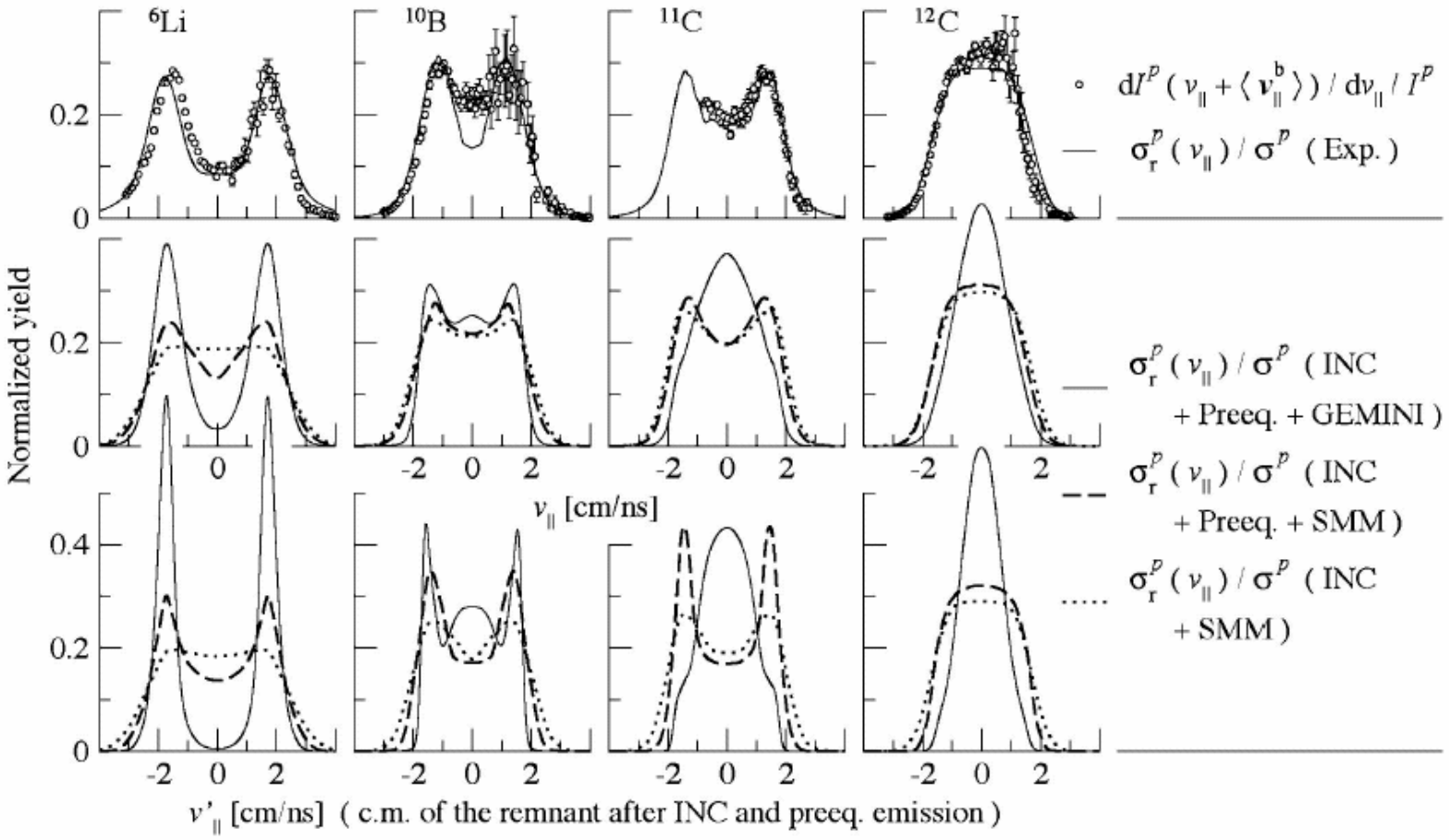

FIG. 16. (First row) Experimental velocity spectra (circles) and reconstructed velocity spectra (solid line). Each spectrum is drawn in the reference frame corresponding to the measured average velocity value of the fragment considered. (This frame corresponds to the "center of mass" frame of the reaction product drawn in Fig. 5). (Second row) Calculated velocity spectra obtained by GEMINI or SMM following INC and the pre-equilibrium stage, and from SMM following directly INC. Each spectrum is drawn in the reference frame corresponding to the calculated average velocity value of the fragment considered. (Third row) Velocity recoil introduced by the GEMINI or SMM phase alone (recoils by INC and pre-equilibrium stages not included). All spectra are normalized to the unit.

TABLE I. Critical parameters from data and SMM_{cold}.

Parameter	Au_{data}	La_{data}	Kr_{data}	Au_{SMM}	La_{SMM}	Kr_{SMM}	Per[a]	LG[b]
m_c	28±3	24±3	18±2	26±3	23±3	17±2		
E_c^*	4.5±0.5	5.5±0.6	6.5±1.0	4.3±0.5	5.3±0.6	6.2±1.0		
τ	2.16±0.08	2.10±0.06	1.88±0.08	2.11±0.05	2.05±0.05	1.81±0.06	2.20	2.21
β	0.32±0.02	0.34±0.02	0.53±0.05	0.35±0.03	0.37±0.03	0.57±0.06	0.44	0.328
β/γ	0.22±0.03	0.25±0.01	0.50±0.01	0.28±0.03	0.29±0.05	0.52±0.01		
γ	1.4±0.3[c]			1.02±0.23[c]			1.76	1.24
γ	1.32±0.15[d]	1.20±0.08[d]						

[a]Percolation.
[b]Liquid gas.

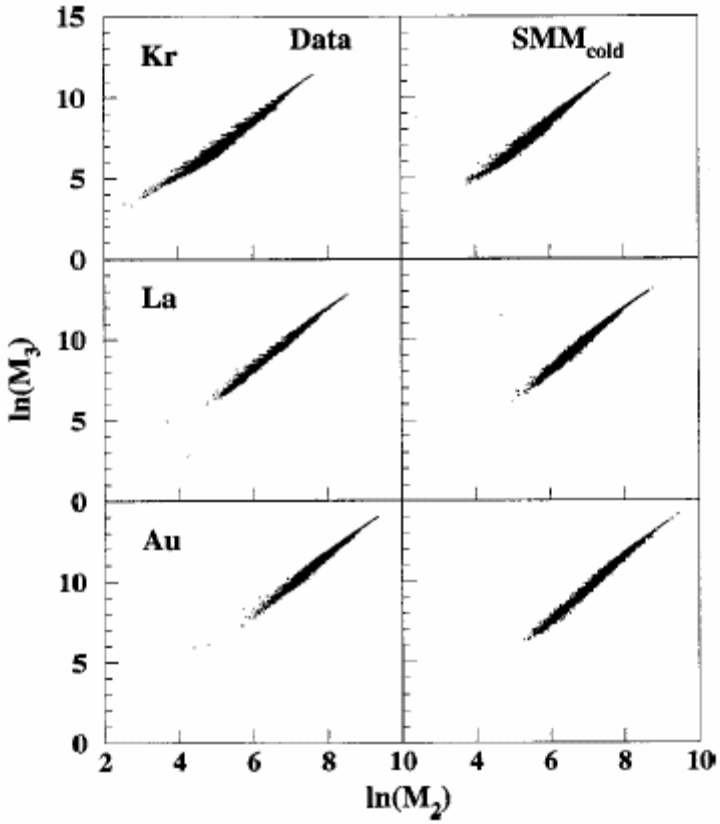

FIG. 12. $\ln(M_3)$ vs $\ln(M_2)$ for Au, La, and Kr above the critical energy.

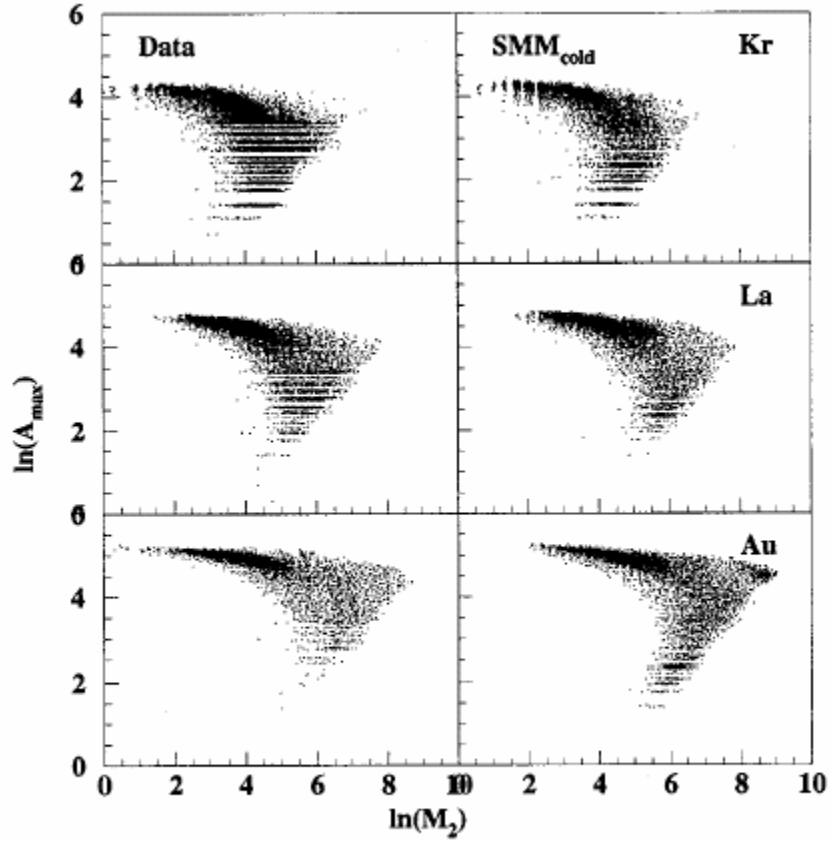

FIG. 15. Scatter plot of the $\ln(A_{max})$ vs $\ln(M_2)$ from data and SMM_{cold}.

Comparison of 1*A* GeV ^{197}Au+C data with thermodynamics: The nature of the phase transition in nuclear multifragmentation

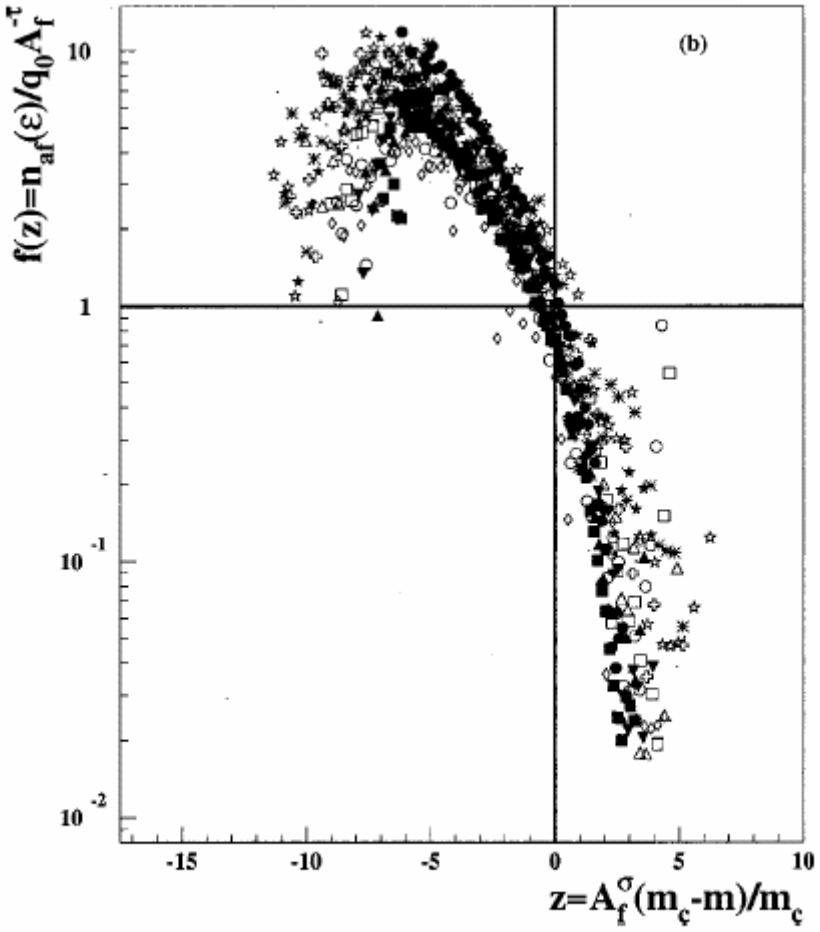

FIG. 18. The scaling functions for data. The intersection of the solid lines marks the critical point.

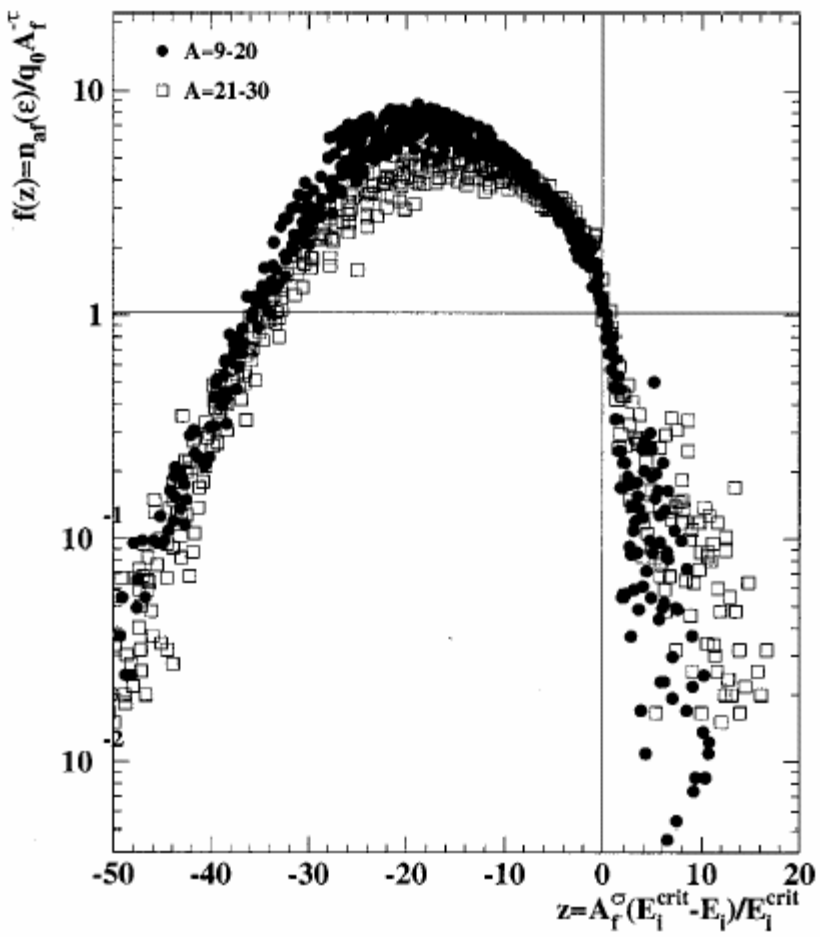

FIG. 27. Scaling function obtained from SMM_{hot} for MF of $A=160$, $Z=64$.

Thermal expansion effects in the 8 GeV/c $\pi^- + {}^{197}$Au reaction

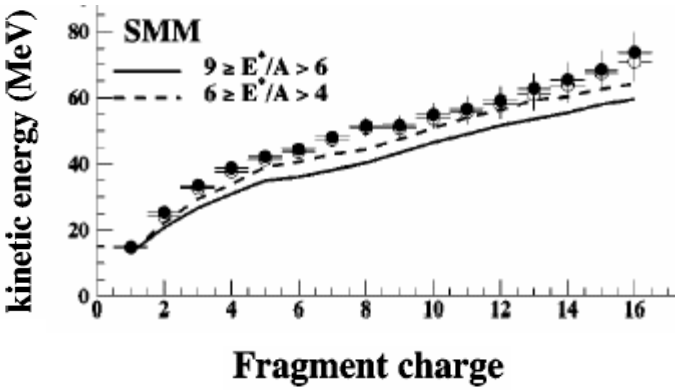

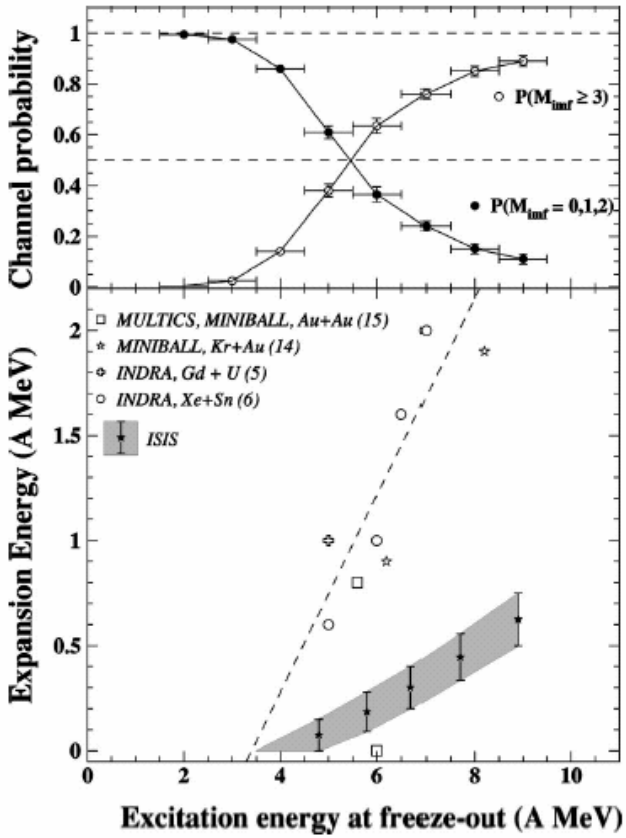

FIG. 4. Upper panel: decay channel probability as a function of the excitation energy, corrected for detector efficiency. The horizontal errors correspond to the excitation energy bin width; the vertical ones represent two assumptions regarding the detector efficiency. Lower panel: comparison between 8 GeV/c $\pi^- + {}^{197}$Au reactions and central heavy-ion collisions. The shaded area corresponds to the ISiS expansion energies extracted with SMM at $3V_0$ (upper limit) and $2V_0$ (lower limit). The dashed line summarizes the expansion energies extracted in central heavy-ion collisions with various assumptions regarding the source characteristics. See [5,6,14,15] for more details.

Sideways-peaked angular distributions in hadron-induced multifragmentation: Shock waves, geometry, or kinematics?

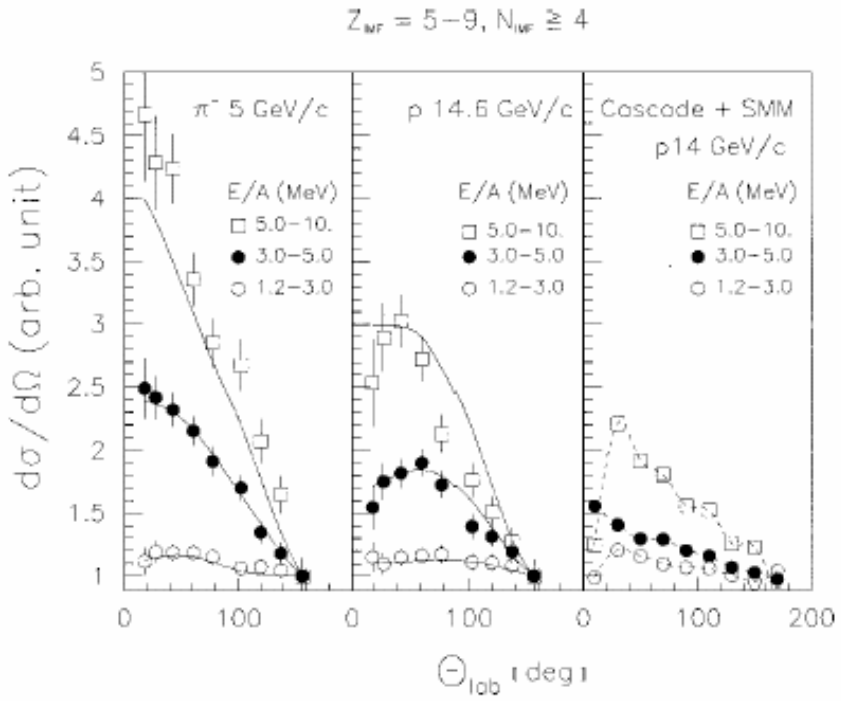

FIG. 3. Relative angular distributions as a function of IMF kinetic energy for $Z=5-9$ fragments from events with IMF multiplicity $N_{IMF} \geqslant 3$ from 5 GeV/c π^- (left) and 14.6 GeV/c proton (center) reactions on ^{197}Au. Data are gated on fragment E/A, as indicated. The absolute yield for each kinetic-energy cut decreases with increasing fragment E/A value. Solid lines are the result of a two-component moving-source fit to the data. The right-hand frame shows predictions of an INC and SMM hybrid calculation of the angular distributions for 14.6 GeV/c protons, gated on fragment energy (symbols and dashed line). All distributions are normalized to unity at the most backward angle.

Nuclear Physics A681 (2001) 267c–274c

Signals for the transition from liquid to gas in hot nuclei

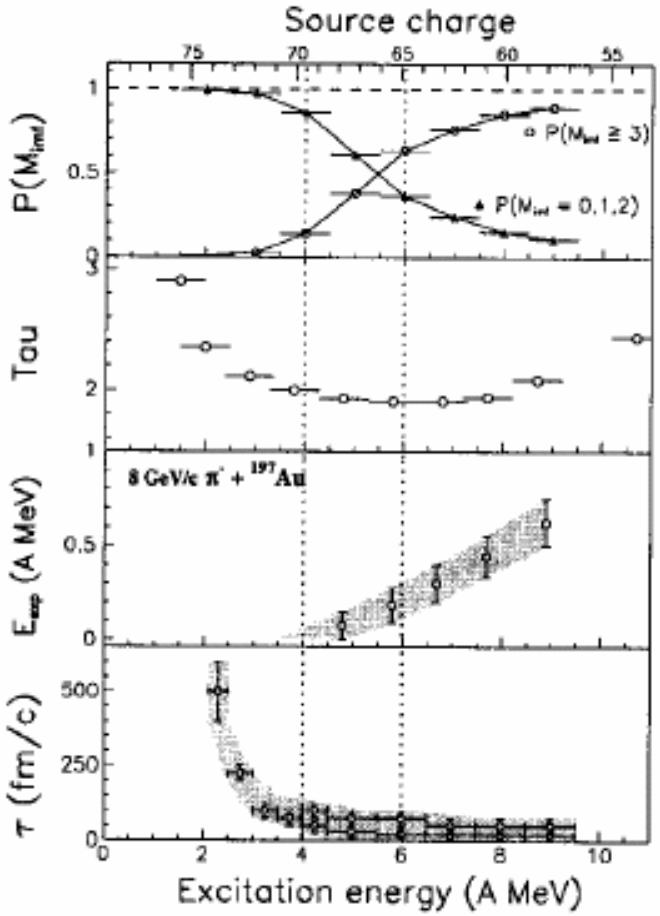

Figure 6. Dependence on E^*/A for the following quantities, from bottom up: relative IMF emission time τ, extra radial expansion energy ϵ_R, charge distribution power-law exponent τ, and probabilbiy for IMF multiplicity $M_{IMF} \geq 3$ (open) and $M_{IMF} \leq$ (closed)

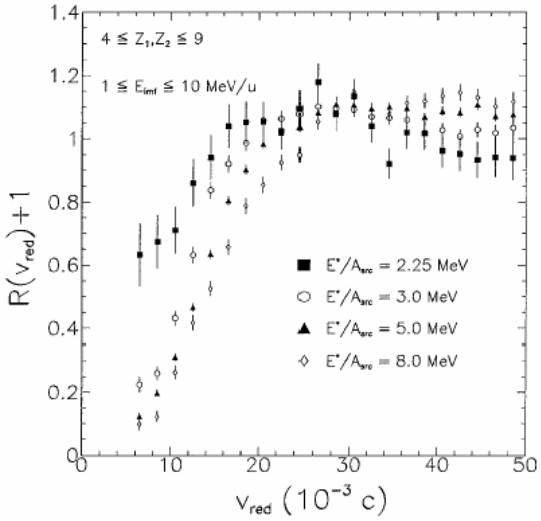

FIG. 1. Reduced velocity correlation functions generated for four different excitation energy per nucleon bins. IMF kinetic energy acceptance is in source frame is $E_{\rm IMF}/A = 1{-}10$ MeV.

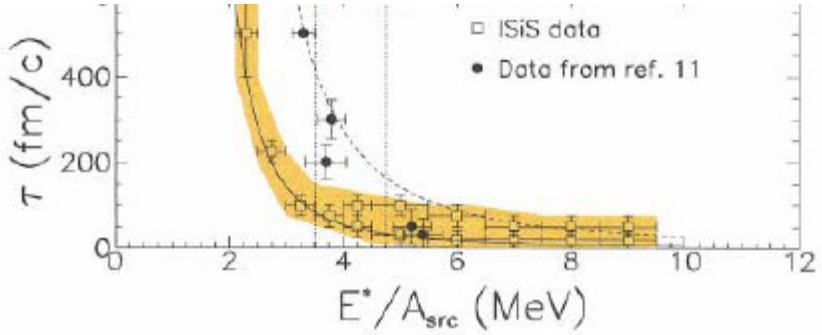

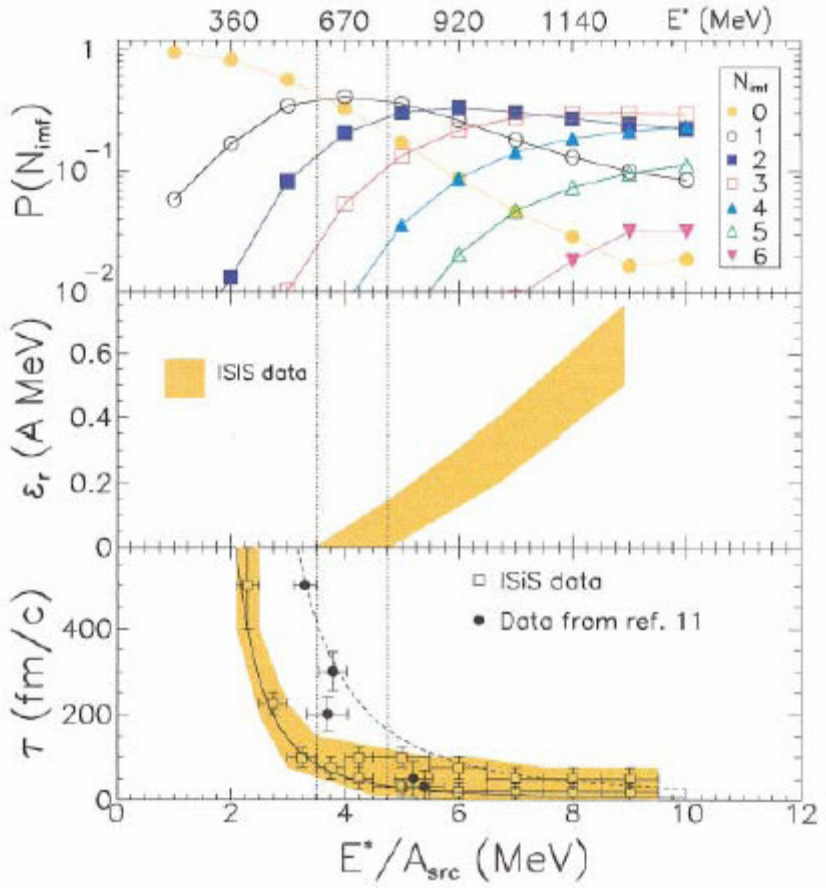

FIG. 3 (color). Dependence on E^*/A for source lifetime (bottom), thermally driven expansion energy ϵ_r [29] (center), and probability of observing a given IMF multiplicity (top). In the bottom panel, the shaded area indicates the range of possible solutions (space-time) consistent with IMF observables. The solid line is an exponential fit to the ISiS results; the dashed line a similar fit using heavy-ion data [11].

Nuclear Physics A654 (1999) 786c–791c

Multifragmentation with GeV Light-Ion Beams*

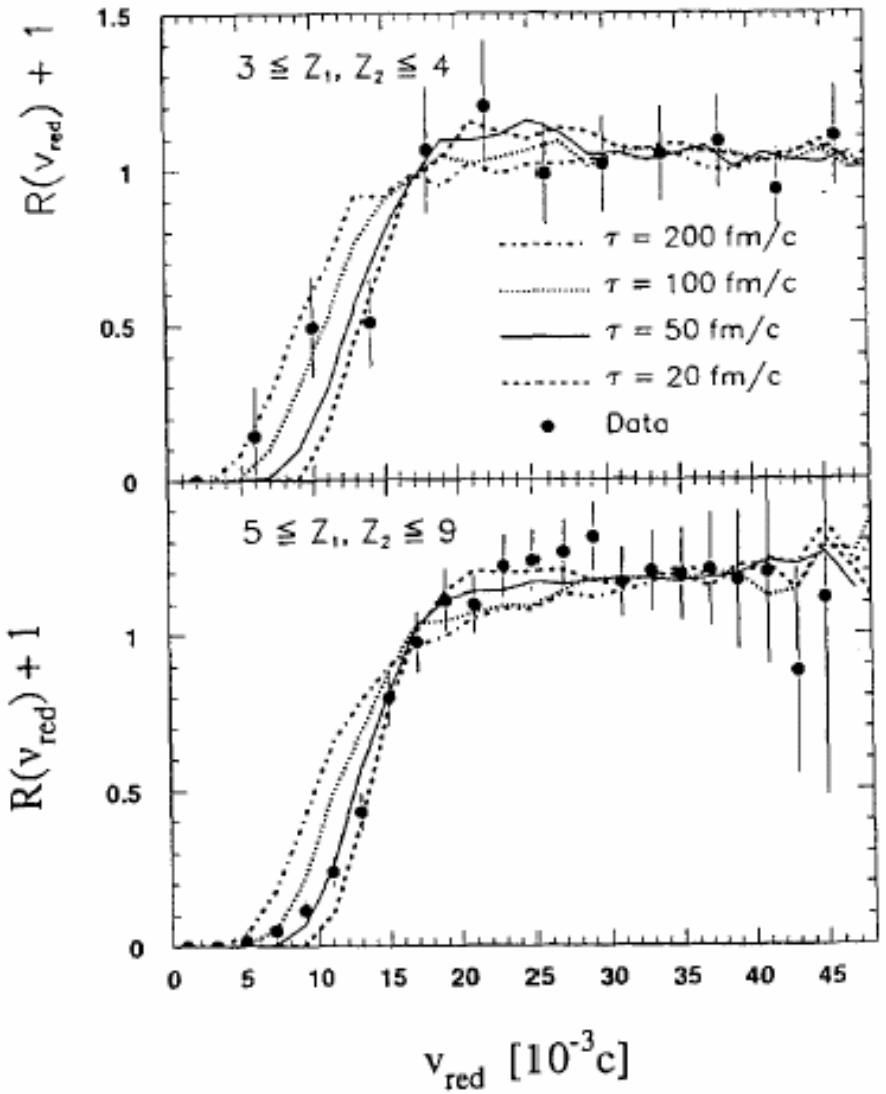

Figure 2. Reduced relative velocity correlation function for the 4.8 GeV ^{3}He + ^{197}Au reaction (points). Data were selected for pairs of events with thermal multiplicity $\leq$ 11 and E/A = 0.7-3.0 MeV. Lines are results of N-body simulation with $\rho/\rho_o = 0.25$ and maximum residue size Z=12. Time scale is indicated on figure.

Multifragmentation reactions and properties of stellar matter at subnuclear densities

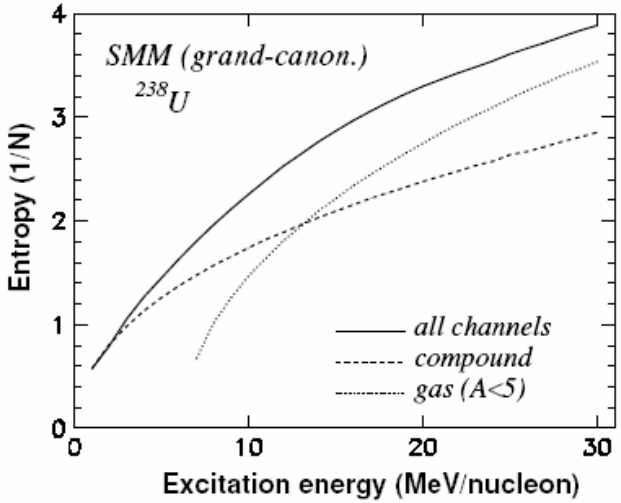

FIG. 1. Entropy per nucleon for different disintegration channels of ^{238}U as a function of excitation energy per nucleon. Calculations are performed within the grand-canonical version of the SMM [12,21] at the freeze-out density $\rho = \rho_0/3$. Dashed and dotted lines correspond to compound nucleus and vaporization ($A \leqslant 4$) channels, respectively. Solid line is the total entropy, obtained by summing over all breakup channels.

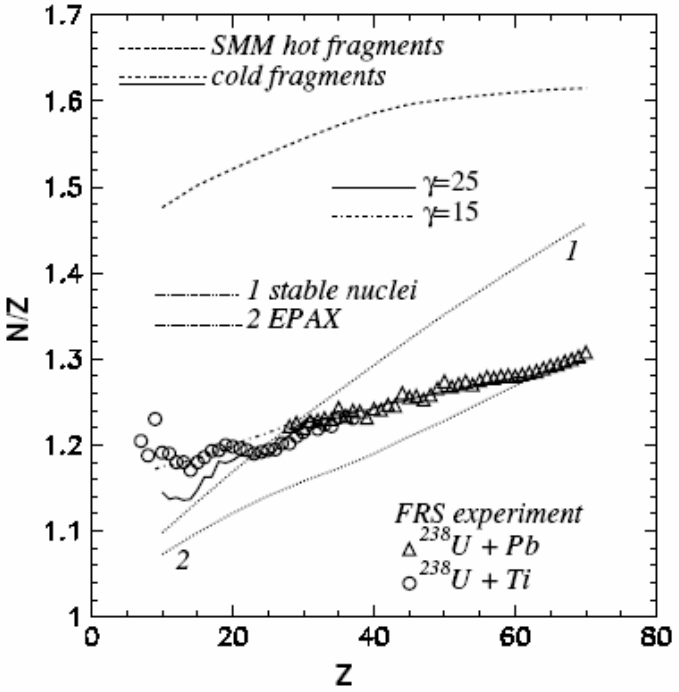

FIG. 2. Mean N/Z vs charge of fragments produced in breakup of ^{238}U with energy 1 GeV/nucleon on Pb and Ti targets. Points are experimental data obtained on fragment separator (FRS) at GSI [24]. Dashed line is SMM calculation for primary hot fragments; solid and dot-dashed lines are fragments after secondary deexcitation. Dotted line 1 corresponds to stable nuclei, dotted line 2 is the EPAX phenomenological parametrization for nuclei produced by spallation. Solid and dashed lines are calculations at the standard symmetry energy parameter $\gamma = 25$ MeV; dot-dashed line is for reduced $\gamma = 15$ MeV.

Nuclear Physics A 584 (1995) 737–756

Multifragmentation of spectators in relativistic heavy-ion reactions

^{197}Au + Cu at E/A = 600 MeV.

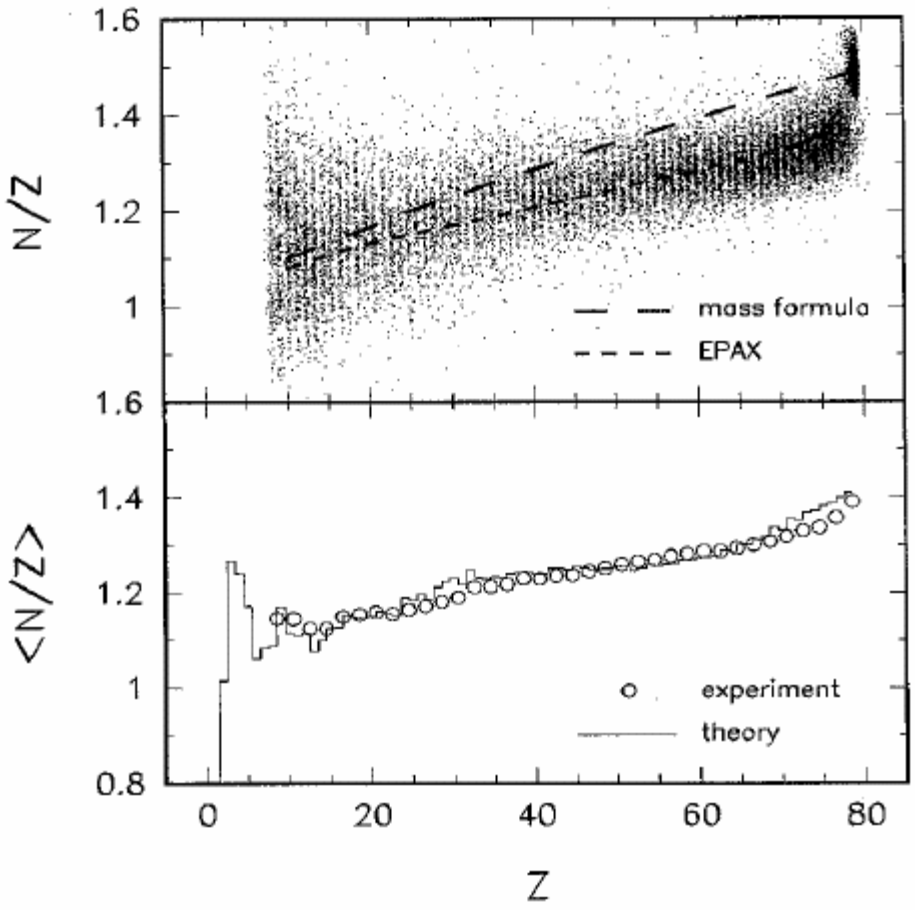

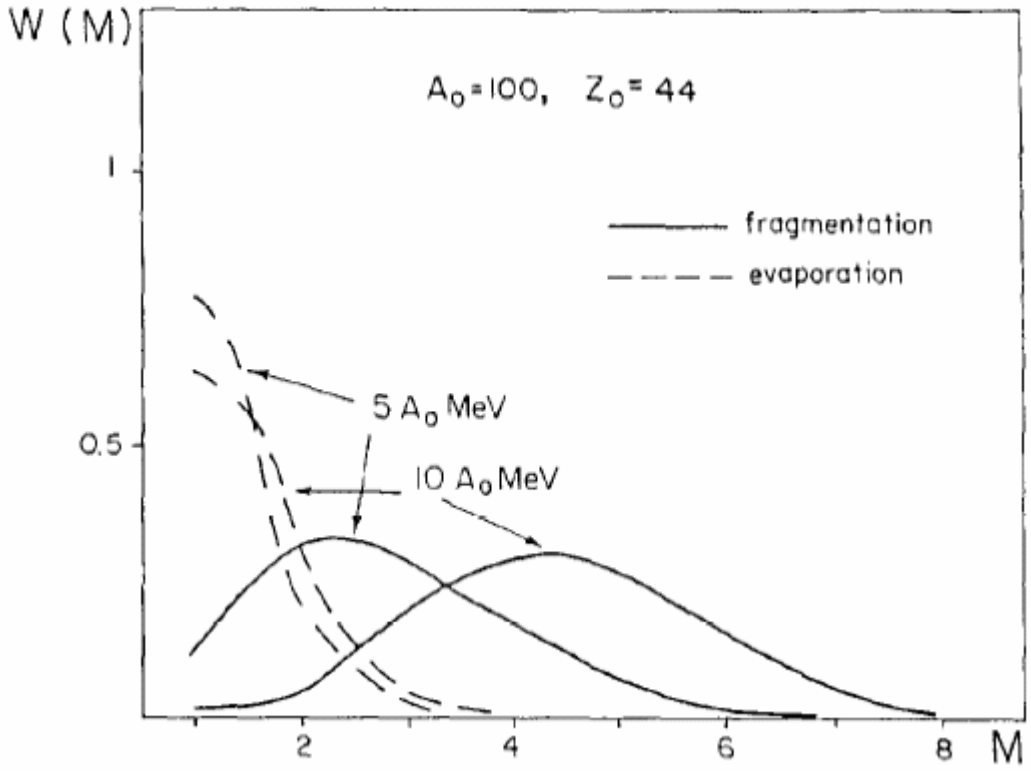
W (M)
$A_0 = 100, \quad Z_0 = 44$
1
0.5
fragmentation
evaporation
$5\ A_0$ MeV
$10\ A_0$ MeV
2
4
6
8
M

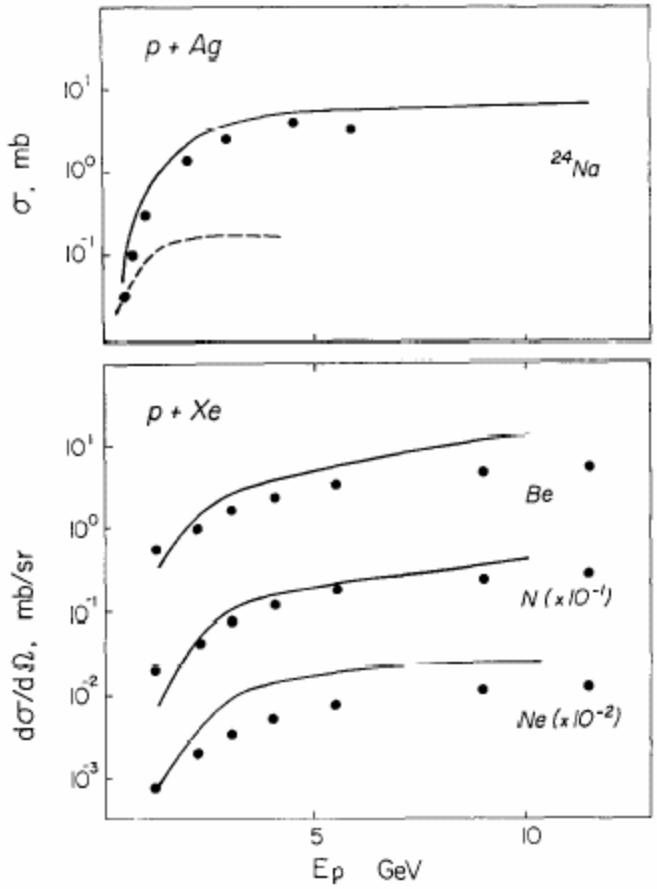
p + Ag
σ, mb
10^1
10^0
10^{-1}
^{24}Na
p + Xe
$d\sigma/d\Omega$, mb/sr
10^1
10^0
10^{-1}
10^{-2}
10^{-3}
Be
N (x 10^{-1})
Ne (x 10^{-2})
5
10
E_p GeV

Safety for humans,
risk assessment for electronic devices
in space missions

Galactic cosmic rays

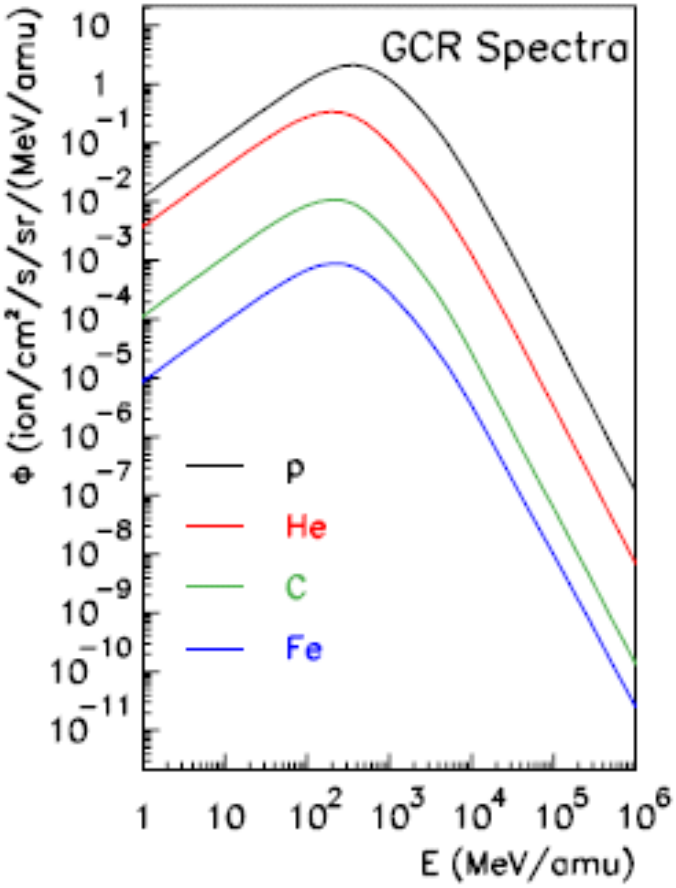

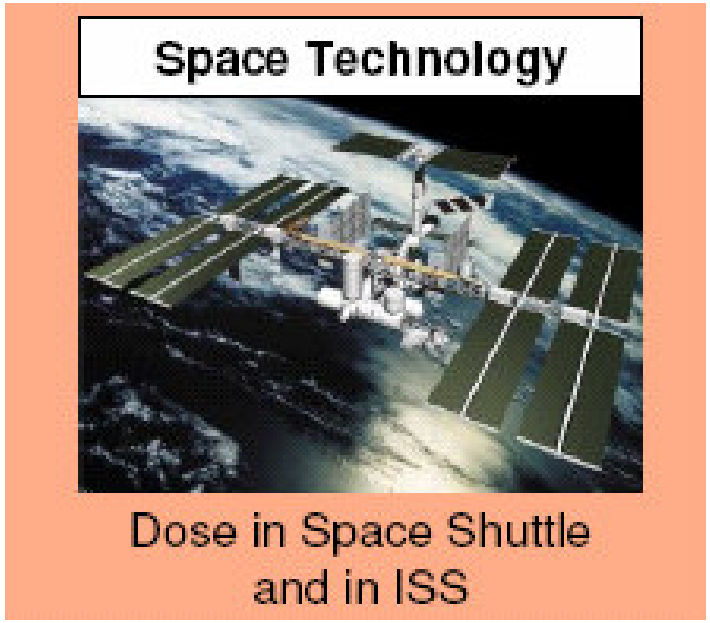

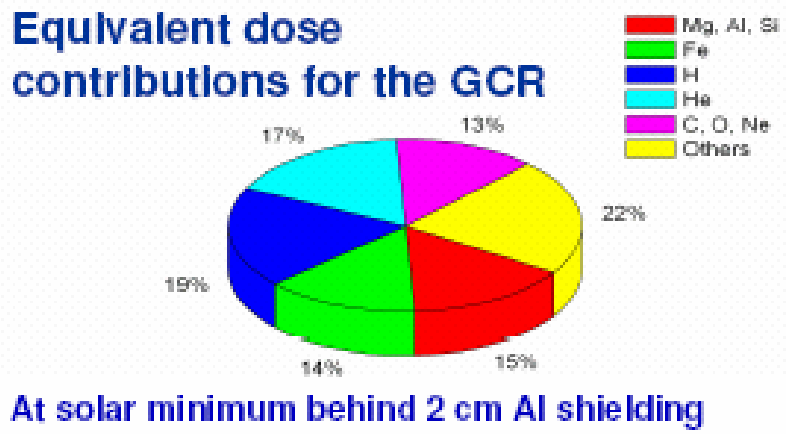

Discussions at NUFRA2007

Crab nebula, after supernova explosion

Numerical simulations of supernova explosions

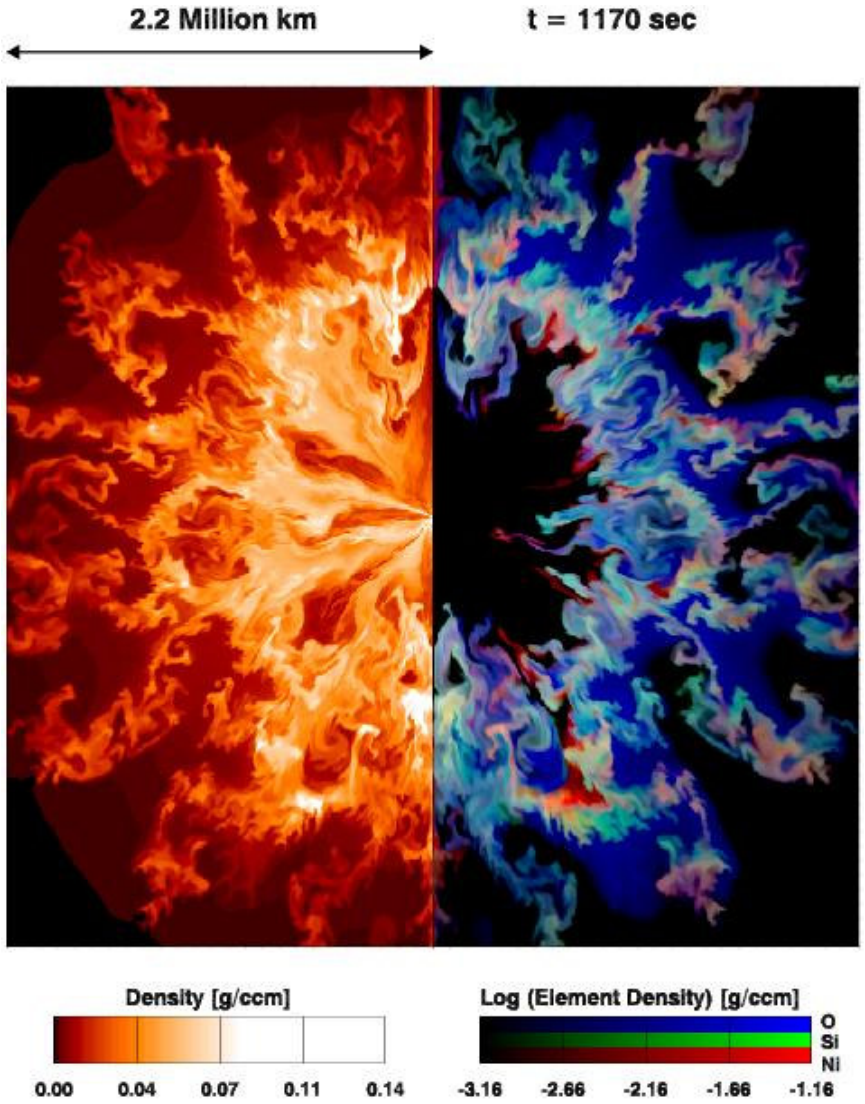

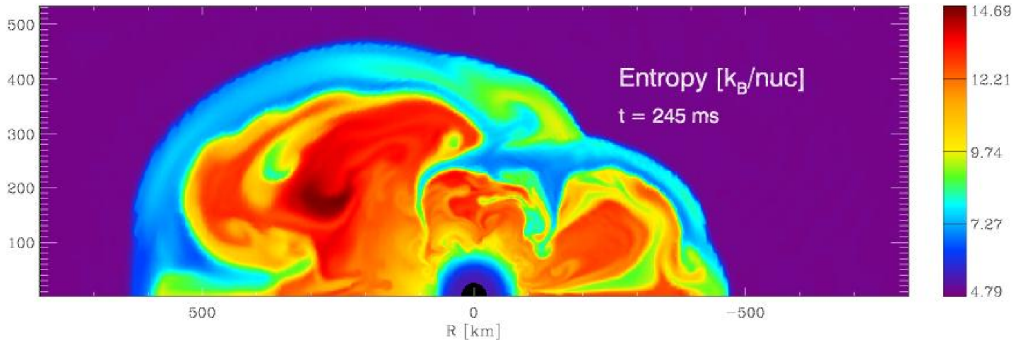

Sketch of the post-collapse stellar core during the neutrino heating and shock revival phase

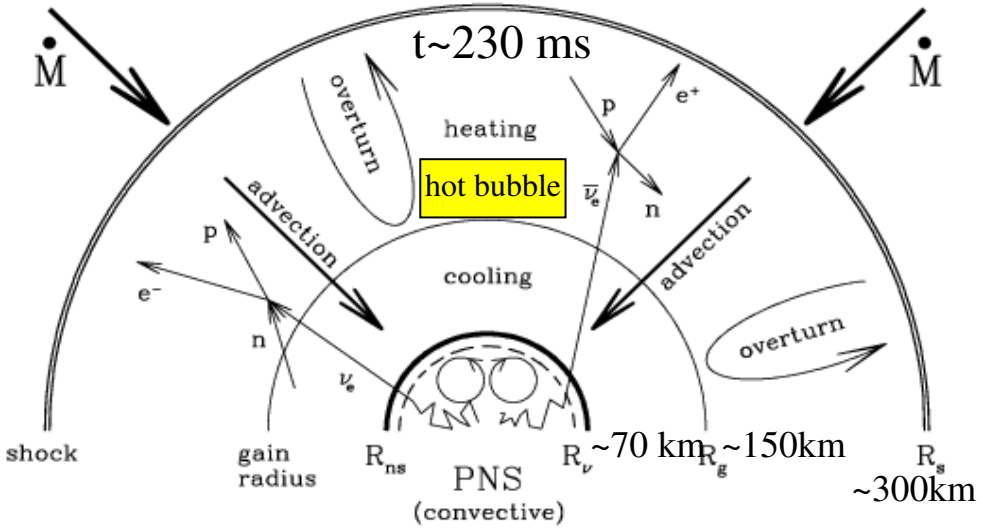

H.-T. Janka, K. Kifonidis, M. Rampp
Lect.Notes Phys.578:333-363,2001

Statistical description of supernova matter

Statistical ensemble
with fixed T, ρ_B, $Y_{L(e)}$

nuclear species (A,Z): $\boldsymbol{\mu_{AZ}=A\mu+Z\xi}$

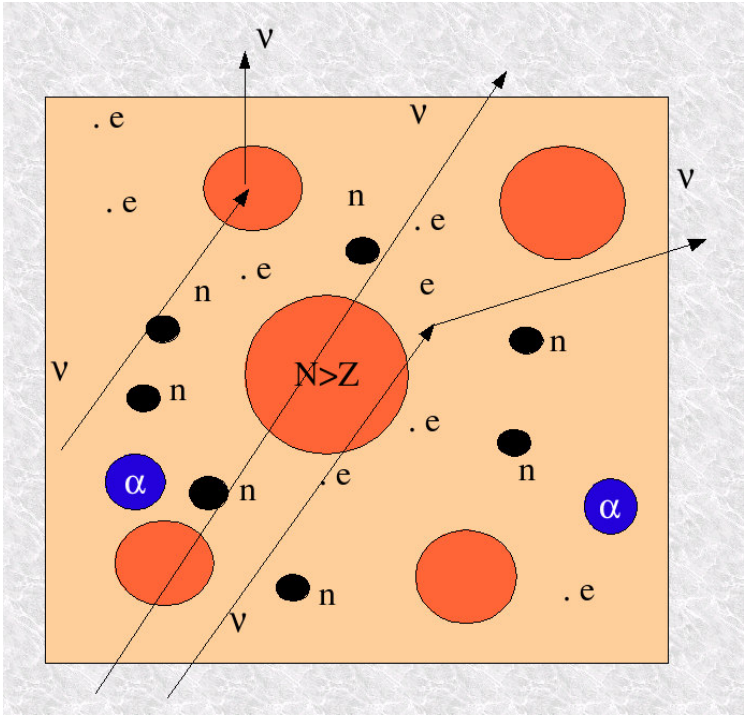

calculations done in a box
containing 1000 baryons

baryon number conservation

$$\rho_B = \Sigma_{AZ}\, A\, \rho_{AZ} \quad \text{find} \quad \boldsymbol{\mu}$$

charge conservation – electric neutrality

$$\rho_Q = \Sigma_{AZ}\, Z\, \rho_{AZ} \quad \text{find} \quad \xi$$

lepton number conservation

$$Y_L = \rho_e / \rho_B \quad \text{(free neutrinos)}$$

$$Y_L = (\rho_e + \rho_\nu) / \rho_B \quad \text{(trapped } \nu\text{)}$$

A.S.Botvina and I.N.Mishustin, Phys.Lett. B584, 233 (2004);
Phys.Rev. C72, 048801 (2005)

Grand-Canonical approximation for stellar matter

Nuclear pressure: $$P_{\rm nuc} = T\sum_{AZ} g_{AZ}\frac{V_f}{V}\frac{A^{3/2}}{\lambda_T^3}\exp\left[-\frac{1}{T}\left(F_{AZ}-\mu_{AZ}\right)\right] \equiv T\sum_{AZ}\rho_{AZ}$$

Nuclear fragment free energies are as in SMM: $$F_{AZ} = F^B_{AZ} + F^S_{AZ} + F^{\rm sym}_{AZ} + E^C_{AZ}$$

with Coulomb screening: $$E^C_{AZ} = \frac{3e^2}{5r_0}\left[1-\frac{3}{2}\left(\frac{\rho}{\rho_0}\right)^{1/3}+\frac{1}{2}\left(\frac{\rho}{\rho_0}\right)\right]\frac{Z^2}{A^{1/3}}$$

Including electrons and neutrinos:

for $T, \mu_e >> m_e$ $$\rho_e = \frac{1}{3\pi^2}\left[\mu_e^3 + \mu_e\left(\pi^2T^2 - \frac{3}{2}m_e^2\right)\right] = \rho_Q$$ - electro-neutrality

electron pressure: $$P_e = \frac{\mu_e^4}{12\pi^2}\left[1+2\left(\frac{\pi T}{\mu_e}\right)^2+\frac{7}{15}\left(\frac{\pi T}{\mu_e}\right)^4-\frac{m_e^2}{\mu_e^2}\left(3+\left(\frac{\pi T}{\mu_e}\right)^2\right)\right]$$

Neutrinos are treated as electrons but as massless particles with the spin factor twice smaller

equilibrium with electrons and neutrinos (if trapped): $$\mu_{e^-} = -\mu_{e^+} = -\xi + \mu_L$$ $$\mu_\nu = -\mu_{\tilde\nu} = \mu_L \ .$$

Thermal photons included (black body radiation), e.g., pressure: $$P_\gamma = \frac{\pi^2T^4}{45\hbar^3c^3}$$

Energy evolution of mass distributions of fragments in multifragmentation reactions and in stellar mater

A.Botvina and I.Mishustin, PRC**72**(2005)048801

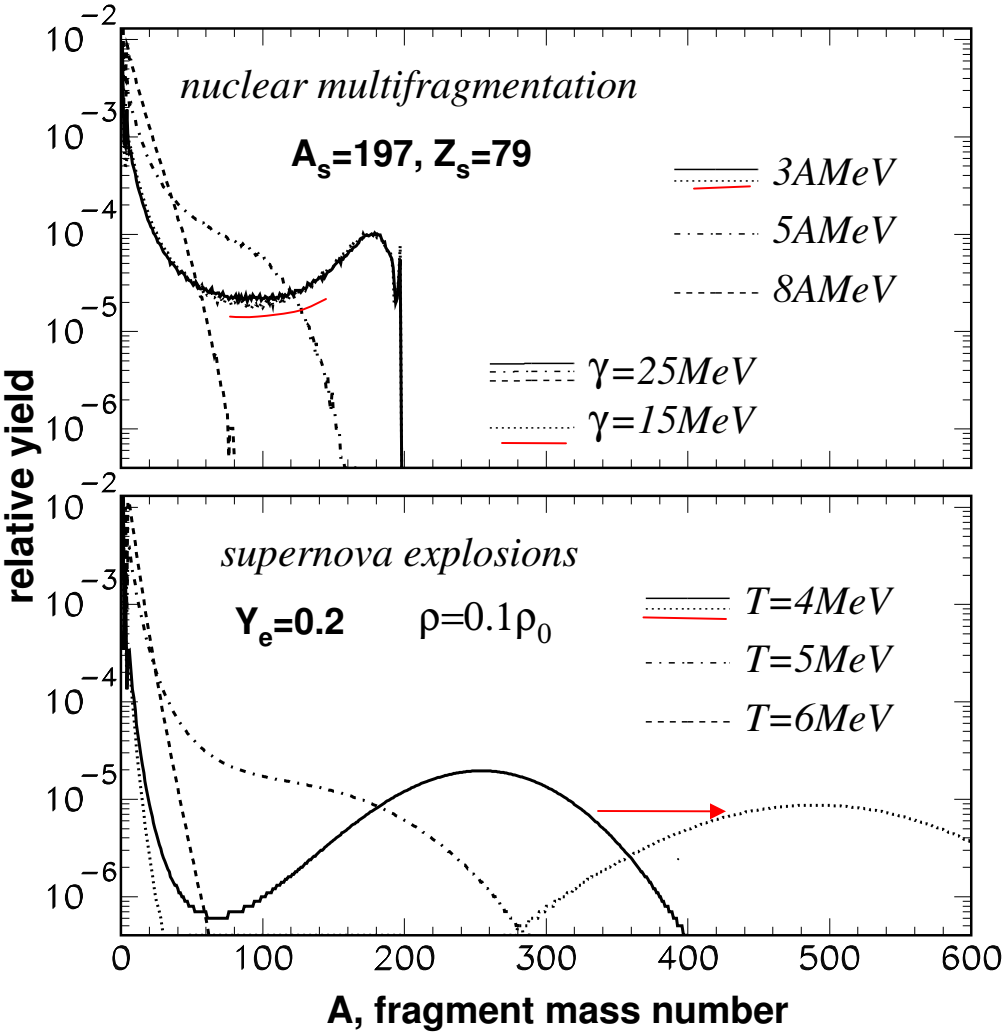

super-heavy nuclei are possible

Conclusions: multifragmentation for astrophysics

Similar conditions of nuclear matter are reached in multifragmentation reactions and during collapses and explosions of massive stars.

The statistical models successfully applied for nuclear multifragmentation can be generalized for astrophysical conditions. Nuclear parameters of the models, in particular, the symmetry energy, can be extracted from multifragmentation experiments.

Broad variety of nuclei including exotic and neutron-rich are produced in stellar matter. Modification of the symmetry energy of nuclei in dense hot medium is important for rates of electro-weak reactions, and for nucleosynthesis of heavy elements.

J.Iglio et al. PRC74, 024605 (2006)

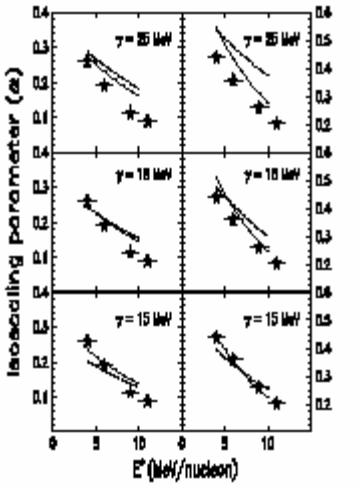

FIG. 11. Comparison of the SMM calculated α (lines) with the experimentally determined α (symbols) as a function of excitation energy for different values of the symmetry energy coefficient γ. The dotted lines correspond to the primary fragments and the solid lines to the secondary fragments. The left column shows the comparison for the ^{58}Ar+^{58}Ni and ^{58}Ca+^{58}Ni pair, and the right column shows the comparison for the ^{58}Ar+^{58}Fe and ^{58}Ca+^{58}Ni pair.